Electroproduction of $\phi(1020)$ Mesons at High Q^2 with CLAS

Joseph P. Santoro

Dissertation submitted to the Physics Department of Virginia Polytechnic Institute and State University in partial fulfillment of the requirements for the degree

Doctor of Philosophy
in
Physics

Elton Smith, Co-Chair
John Ficenec, Co-Chair
Mark Pitt
Tetsuro Mizutani
Uwe Täuber

August 5, 2004
Blacksburg, Virginia

Keywords: Vector Meson, Electroproduction, Nucleon, GPDs, quark

Electroproduction of $\phi(1020)$ Mesons at High Q^2 with CLAS

Joseph P. Santoro

ABSTRACT

This analysis studies the reaction $ep \to e'p'\phi$ in the kinematical range $1.6 \leq Q^2 \leq 3.8$ GeV^2 and $2.0 \leq W \leq 3.0$ GeV at CLAS. After successful signal identification, total and differential cross sections are measured and compared to the world data set. Comparisons are made to the predictions of the Jean-Marc Laget(JML) model based on Pomeron plus 2-gluon exchange. The overall scaling of the total cross section was determined to be $1/Q^{4.6\pm1.7}$ which is compatible within errors to the Vector Meson Dominance prediction of $1/Q^4$ as well as to the expected behavior of a quark and gluon exchange-dominated model described by Generalized Parton Distributions of $1/Q^6$. The differential cross section $\frac{d\sigma}{d\Phi}$ was used to determine that the s-channel helicity conservation (SCHC) assumption is valid within the precision of the current data. SCHC leads to a simple expression for the decay angular distribution from which R, the ratio of the longitudinal to the transverse cross section, can be extracted. Under the assumption of SCHC, we determine $R = 1.33 \pm 0.18$ at an average Q^2 of 2.21 GeV^2 which leads to a determination of the longitudinal cross section $\sigma_L = 5.3 \pm 1.3$ nb for exclusive ϕ production.

Contents

List of Figures

List of Tables

For my grandfathers Louis and Nicola

Acknowledgments

There are many people whose constant support and encouragement resulted in the successful completion of my PhD. First I would like to thank my on site co-advisor Elton Smith who provided the constant guiding voice for the duration of this project. Without Elton's constant support and advice, this work would have never come to fruition. I would also like to thank my other co-advisor John Ficenec, based at Virginia Tech, who was directly responsible for the opportunity to complete my research at Jefferson Lab. Both co-advisors exhibited unwaivering patience and support throughout the entirety of this project.

I would also like to thank the rest of my committee who spent the time reading and critiquing my thesis and providing the much needed feedback facilitating its successful completion. They, along with all the professors I had at Virginia Tech have been an integral part of my physics education, both in the classroom and out.

Special thanks goes out the Virginia Tech Physics department secretary Christa Thomas who was a pillar of support and great friend throughout my tenure as a graduate student.

I would especially like to thank Dr. Jean-Marc Laget for his invaluable discussions of the theoretical framework of this thesis topic as well as for providing a phenomenological model and calculation to which to compare my results.

The success and quality of the e1-6 experiment was a result of the hard work and dedication of the entire CLAS collaboration, especially those intimately involved in the calibration of the detector as well as the processing of the data for the e1-6 run. Besides the collaboration members, there is an invaluable staff of Hall B technicians, engineers and staff who were responsible for the smooth operation of the detector and accelerator during the e1-6 run. I extend a special thanks to Tom Carstens, Denny Insley, and Jill Gram for allowing me to tag along during the detector maintenance periods during which I accrued very useful hardware knowledge and experience.

Throughout the duration of this project, I have been blessed to have the unyielding support and encouragement of a group of close friends. To all of you in New York, Newport News, and elsewhere, I'd like to express my heartfelt and never-ending gratitude. You all make this accomplishment all the more sweeter.

I want to thank my entire family for their love, guidance and support throughout my entire life leading up to this achievement, especially my brother who provided a calming voice and open ear whenever it was needed.
Last but definitely not least, I want to thank my parents who through a lifetime of sacrifice, hard work, and unabated love provided me every opportunity possible to make the most of life. They are the primary reason I am the person I am today.
It has been a long and winding road ending miles and years from where it began.

Chapter 1

Theoretical Background and Motivation

1.1 $\phi(1020)$ Electroproduction Overview

Vector meson electroproduction has opened a unique window into the substructure of the nucleon as well as the hadronic structure of the photon [4]. Historically, vector meson electroproduction has been described in terms of the hadronization of the virtual photon at low Q^2 (low virtuality of the photon), where the virtual photon fluctuates into a virtual meson and subsequently scatters diffractively off of the nucleon. This occurs in a time $\Delta\tau$, consistent with the uncertainty principle, and completely characterizes the temporal and spatial extent ($c\Delta\tau$) of the fluctuation. In this regime, the exchange mechanisms are dominated by hadronic degrees of freedom. At higher Q^2 the wavelength of the virtual photon, given by $\lambda = \frac{\hbar}{\sqrt{Q^2}}$, decreases making the virtual photon probe more sensitive to increasingly smaller distance scales. This corresponds to a transition from hadronic to quark and gluon (partonic) degrees of freedom. In this domain, deeply inelastic production of vector mesons is described by generalized parton distributions(GPDs). Primarily, GPDs are a set of four functions of quark/gluon momentum (transverse, longitudinal and orbital) and spin which describe the behavior of these partons in the target nucleon. The Q^2 domain where the vector meson exchange$\rightarrow$GPD transition occurs is still a matter of debate. The

systematic study of ϕ electroproduction as well as ρ, and ω electroproduction has the potential to shed some light on this question as well as other relevant quandaries of hadronic physics.

The pure $s\bar{s}$ content of the ϕ makes it an ideal candidate to study the pure gluon exchange mechanisms in each regime; the Pomeron in the low Q^2 region and gluon exchange graphs in the high Q^2 region. The ϕ meson is 99% ($s\bar{s}$) and has no quark flavors in common with the nucleon (uud,udd) and thus any diagrams containing disconnected quark lines are suppressed relative to connected ones. The suppression of these disconnected quark graphs is known as OZI suppression [5]. Any $s\bar{s}$ content in the nucleon will be reflected in the cross section as well as the spin properties of the decay products.

Through the study of the Q^2 scaling of the total cross section and the scaling of the differential cross section $\frac{d\sigma}{dt}$, ϕ electroproduction can be effective in probing the validity of the two Q^2 regimes.

1.1.1 Notation

Assuming the one photon exchange (OPE) approximation, vector meson electroproduction can be written as

$$\gamma^* + N \rightarrow P + \phi \tag{1.1}$$

where γ^* is the virtual photon 4-momentum, N is the target nucleon 4-momentum, P is the scattered nucleon 4-momentum, and ϕ is the electroproduced vector meson 4-momentum (in this case the ϕ). If V is a generalized 4-vector, it can be expressed as an energy part and a 3-momentum part: $V = (E, \vec{V})$. The 4-vectors then assume the following forms in the laboratory:

$\gamma^* = (\nu, \vec{q})$, $N = (M_P, 0)$, $P = (E_P, \vec{P_P})$, $P_\phi = (E_\phi, \vec{P}_\phi)$

The virtual photon 4-momentum can be written in terms of the incident electron 4-momentum e and the scattered electron 4-momentum e' as

$$\gamma^* = e - e' \tag{1.2}$$

where $e = (E_e, \vec{P}_e)$ and $e' = (E_{e'}, \vec{P}_{e'})$

Key kinematic variables can now be defined that describe the aforementioned reaction:

- The negative of the 4-momentum squared of the virtual photon,

$$Q^2 = -q^2 = -(\gamma^*)^2 = -(e - e')^2 \tag{1.3}$$

which can be interpreted as the negative mass squared of the virtual photon.

- The $\gamma^* p$ center of mass energy or the $\gamma^* p$ invariant mass

$$W = \sqrt{s} = \sqrt{(\gamma^* + P)^2} \tag{1.4}$$

where s is one of three Mandelstam invariant variables, the next two to be defined forthwith.

- Virtual photon energy

$$\nu = E_e - E_{e'} \tag{1.5}$$

- The 4-momentum transfer squared between the virtual photon and the vector meson (or between the target and scattered nucleon):

$$t = (\gamma^* - P_\phi)^2 = (N - P)^2 \tag{1.6}$$

which is the second Mandelstam variable, and the third

$$u = (\gamma^* - P)^2 = (P_\phi - N)^2 \tag{1.7}$$

which is the 4-momentum transfer squared between the virtual photon and scattered nucleon or between the target nucleon and the vector meson.

- The minimum 4-momentum transfer squared t_{min} is given by

$$t_{min} = (E^{\gamma^*}_{cm} - E^{\phi}_{cm})^2 - (|\vec{\mathbf{p}}^{\gamma^*}_{\mathbf{cm}}| - |\vec{\mathbf{p}}^{\phi}_{\mathbf{cm}}|)^2 \tag{1.8}$$

where $E^{\gamma^*}_{cm}(\vec{p}^{\gamma^*}_{cm})$ is the energy(momentum) of the virtual photon in the $\gamma^* p$ center of

mass frame and $E^{\phi}_{cm}(\vec{\mathbf{p}}^{\phi}_{\mathbf{cm}})$ is the energy(momentum) of the vector meson (in this case the ϕ) in the same reference frame.

• One can define [6]

$$t' = \left| t - t_{min} \right| \tag{1.9}$$

• Q^2, ν, and W can be related via the following relation

$$W^2 = M_p^2 + 2M_p\nu - Q^2 \tag{1.10}$$

• The Bjorken scaling variable x_B, which is the fraction of nucleon 4-momentum carried by the parton impacted upon by the virtual photon is

$$x_B = \frac{Q^2}{2M_p\nu} = \frac{Q^2}{W^2 + Q^2 - {M_p}^2} \tag{1.11}$$

• The angle Φ between the electron scattering plane and the hadron production plane (see Figure 1.1)

The electroproduction reaction can then be described by the following set of 4 independent variables:

$$(Q^2, t, \Phi, [W \quad or \quad \nu \quad or \quad x_B]) \tag{1.12}$$

The reduced cross section $\sigma(Q^2, W)$ integrated in Φ and t is given by

$$\sigma_{\gamma^* + N \to P + \phi}(Q^2, W) = \sigma_T(Q^2, W) + \epsilon\sigma_L(Q^2, W) \tag{1.13}$$

where ϵ is the virtual photon polarization parameter given by

$$\epsilon = \frac{1}{[1 + 2(Q^2 + \nu^2)/(4E_e(E_e - \nu) - Q^2)]} \tag{1.14}$$

ϵ is expressible in terms of the ratio of two elements L_{11} and L_{12} of the spin density matrix of the photon $\tilde{L}_{\mu\nu}$ evaluated in the Breit-Wigner reference frame [1]. $\sigma_T(Q^2, W)$ is the cross section due to transversely polarized virtual photons and $\sigma_L(Q^2, W)$ is the cross section due to the longitudinally polarized virtual photons. The reduced cross section is related to the measured cross section through the virtual photon flux

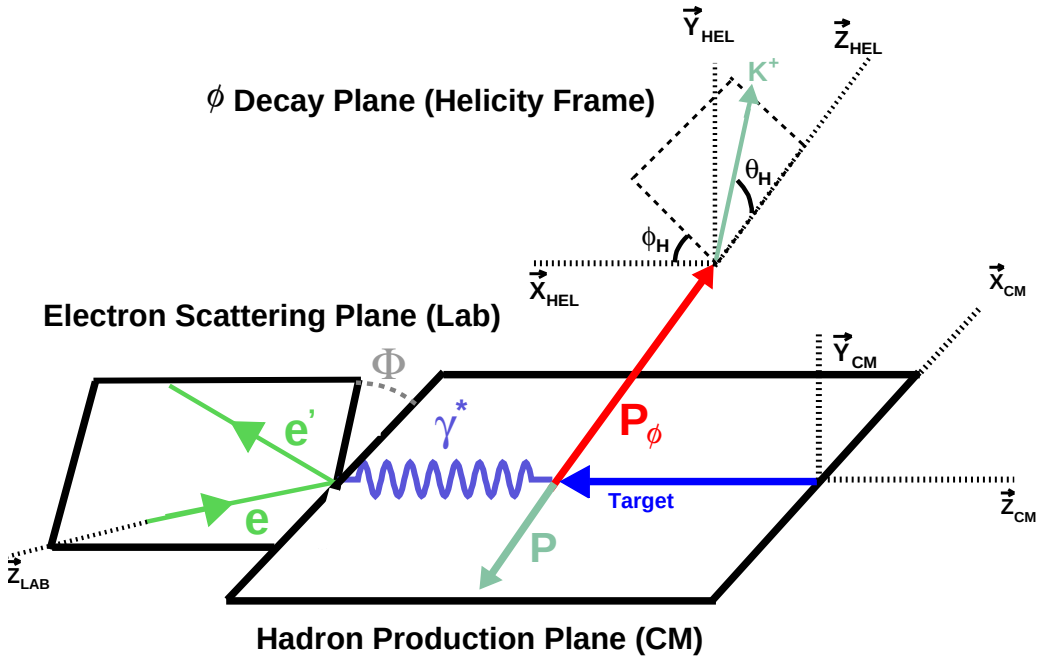

Figure 1.1: Graphical representation of ϕ meson electroproduction. Shown from left to right then above are the electron scattering plane, the hadron production plane and helicity rest frame of the ϕ respectively. Φ is the relative angle between the electron scattering and hadron production planes. θ_H and ϕ_H are the polar and azimuthal angles of the K^+ defined in the helicity frame basis of the ϕ meson as defined in reference [1]

factor $\Gamma(Q^2, W)$

$$\frac{d^2\sigma}{dQ^2 dW d\phi_{e'}} = \Gamma(Q^2, W)[\sigma_T(Q^2, W) + \epsilon\sigma_L(Q^2, W)] \tag{1.15}$$

and after integrating over the azimuthal angle of the scattered electron in the lab, the measured cross section becomes

$$\frac{d^2\sigma}{dQ^2 dW} = 2\pi\Gamma(Q^2, W)[\sigma_T(Q^2, W) + \epsilon\sigma_L(Q^2, W)] \tag{1.16}$$

where $\Gamma(Q^2, W)$ is given by

$$\Gamma(Q^2, W) = \frac{\alpha}{8\pi^2} \frac{W}{M_p E_e^2} \frac{W^2 - {M_p}^2}{M_p Q^2} \frac{1}{1-\epsilon} \tag{1.17}$$

and α is the fine structure constant. $\Gamma(Q^2, W)$can be interpreted as the probability per GeV^3 of producing a virtual photon at a given Q^2 and W. The definition of the virtual photon flux is ambiguous and there are varying conventions employed. Each convention requires the virtual photon flux to equal the real photon flux as $Q^2 \to 0$ [5]. The convention used here is that from [7].

1.2 The Vector Meson Dominance (VMD) Model

The analysis of photoproduced vector mesons has historically been described within the framework of the Vector-Meson Dominance (VMD) model. The main tenet of the VMD model is the assumption that vector meson production is dominated by interactions between the nucleon and the vector meson intermediate states of the incoming photon [3]. In other words, if the photon is given by the state vector $|\gamma\rangle$, it can be expressed as a linear combination of a "bare" photon state $|\gamma_B\rangle$ which accounts for a negligible part of the interaction and a hadronic component $|h\rangle$.

$$|\gamma\rangle \cong \sqrt{Z_3}|\gamma_B\rangle + \sqrt{\alpha}|h\rangle \tag{1.18}$$

Z_3 is introduced to ensure proper normalization of $|\gamma\rangle$ [8]. Due to invariance considerations, $|h\rangle$ must have the same quantum numbers as the photon namely $J^{PC} = 1^{--}$. Experimental observations of real and virtual photoproduction demonstrate that ρ^0, ω, and ϕ are produced copiously and therefore are the main contributions to $|h\rangle$. The main hypothesis of VMD is that these three mesons are the sole hadronic constituents of the photon $|\gamma\rangle$ and that the bare photon state $|\gamma_B\rangle$ does not interact with the target hadron or photoproduced hadron. The assumption that $|h\rangle$ is composed of more than just the three aforementioned mesons is referred to as generalized vector dominance (GVD) [8]. The VMD cross section can be expressed

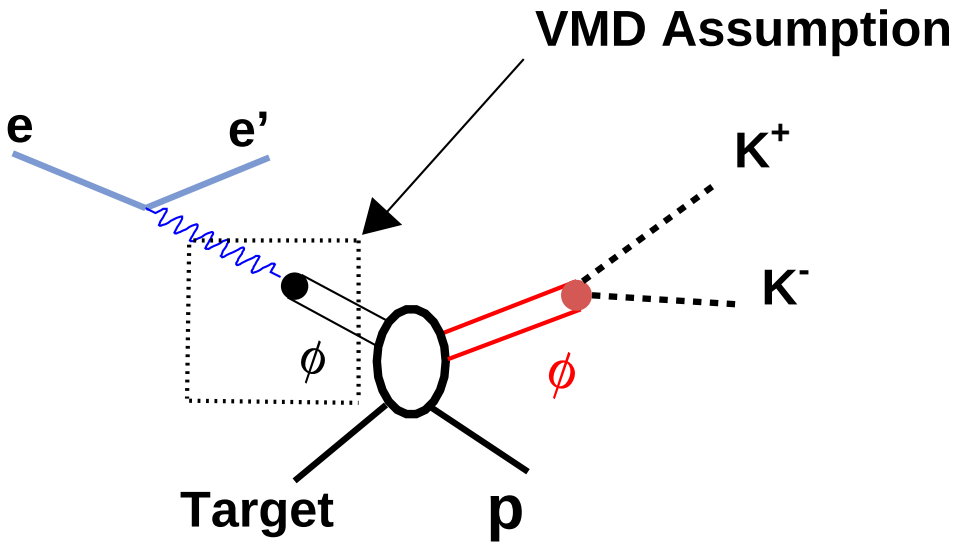

Figure 1.2: ϕ electroproduction through diffractive scattering off the nucleon. The region enclosed in the dotted box represents the VMD assumption of the fluctuation of the virtual photon into a vector meson.

as

$$\frac{d^2\sigma}{dQ^2 dW} = 2\pi\Gamma(Q^2, W)\zeta\sigma_t(1 + \epsilon R)W_D(\cos\theta_H, \psi) \tag{1.19}$$

where within the VMD framework

$$R = \xi^2 \frac{Q^2}{M_\phi} \tag{1.20}$$

is the ratio of the longitudinal to transverse cross sections. ξ^2 is the VMD scaling parameter and takes on a typical value of 0.33. The other components of equation 1.18 are given by:

$$\sigma_t = \frac{A_\phi}{b_\phi}\exp(-b_\phi t') \tag{1.21}$$

$$\zeta = \frac{W^2 - {M_p}^2}{2{M_p}^2\sqrt{\nu^2 + Q^2}} \frac{1}{(1 + \frac{Q^2}{M_\phi})^2} \tag{1.22}$$

$W_D(\cos\theta_H, \psi)$ is the angular decay distribution. Within the framework of VMD and

assuming s-channel helicity conservation (SCHC) the angular decay distribution is

$$W_D(\cos\theta_H, \psi) = \frac{3}{8\pi}\frac{1}{(1+\epsilon R)}[\sin^2\theta_H(1+\epsilon\cos 2\psi) + 2\epsilon R\cos^2\theta_H - \sqrt{2\epsilon(1+\epsilon)R}\cos\delta\sin 2\theta_H\cos\psi] \quad (1.23)$$

where the angle ψ is defined as $\psi = \Phi - \Phi_H$ and θ_H is defined in Figure 1.1. δ is a relative phase factor between the two independent helicity amplitudes. For a discussion and definition of helicity amplitudes see chapter 7 section 1 or reference [1]. The factor ζ allows the extrapolation away from $Q^2 = 0$, a.k.a into the virtual photoproduction regime. This term includes a propagator term as well as a correction to the virtual photon flux [3].

1.3 Particle Exchange Mechanisms, Regge Theory and the JML Model

1.3.1 Particle Exchange Mechanisms

The present analysis is concerned with the generalized reaction $\gamma^* N \rightarrow PX$. When describing the interaction of the electron and the proton, the virtual photon γ^* arises as the exchange particle of the electromagnetic force between the two, Figure 1.3. A similar quantum field theoretic exchange particle mechanism can be used

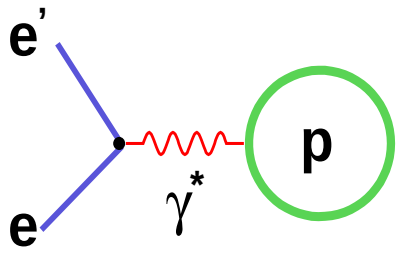

Figure 1.3: The electromagnetic interaction mediated by a virtual photon.

when describing the interaction of the virtual photon γ^* with the proton P at low

energies. The nature of this interaction is illustrated in Figure 1.4. The species of the exchange particle is multi-fold for each reaction considered and is determined by which exchange channel one is considering. The exchange channels are named for the three Mandelstam variables s, t, and u described in section 1.1.1 and denote the three possible directions of momentum flow in $\gamma^* P$ scattering. For the t-channel, the exchange particle is a meson, and is a baryon for the s and u channels (see Figure 1.4). The amplitude $\mathcal{A}$ of each of the diagrams can be constructed from factors associated

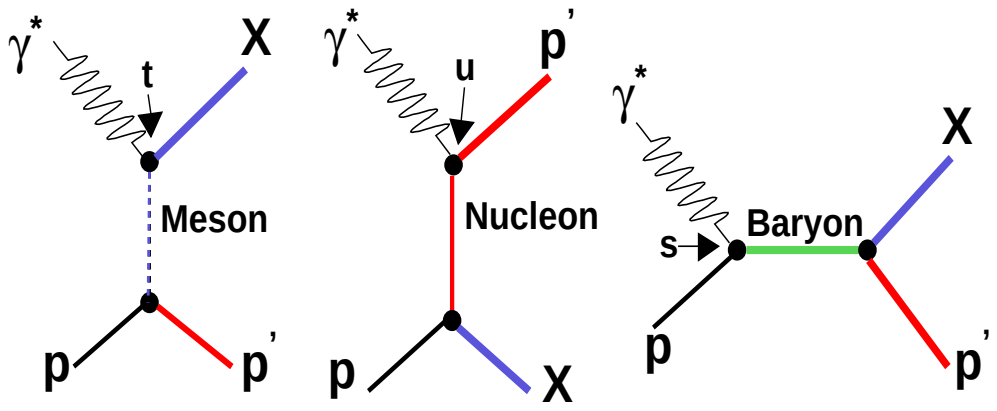

Figure 1.4: Channel-dependent exchange mechanisms for $\gamma^* P \rightarrow P' X$

with each line within the diagram. These are known as the Feynman rules of the diagram [9]. For the diagrams above the amplitude is proportional to the following product of the Feynman propagator $\mathcal{P}_F$, the coupling constants at each of the two vertices g and g' and the spin-dependent vertex functions $\mathcal{V}$ and $\mathcal{V}'$ which depend on which three particles are joined at the vertex [10].

$$\mathcal{A} \propto g\mathcal{V}\mathcal{P}_F g'\mathcal{V}' \tag{1.24}$$

1.3.2 Regge Theory

The process $1+2 \rightarrow 1'+2'$ ($\gamma^*+p \rightarrow p'+X$) is historically described with S-matrix theory. S-matrix theory characterizes the aforementioned scattering process from the initial state vector $|1,2\rangle$ into a final state vector $|1',2'\rangle$ by way of the scattering matrix

S where **S** is unitary matrix [9]. The purpose of S-matrix theory is to calculate the matrix element

$$\mathcal{A} =< 1', 2'|\mathbf{S}|1, 2 > \tag{1.25}$$

where the matrix $\mathcal{A}$ represents the amplitude of the scattering process. The amplitude $\mathcal{A}$ can be expressed as partial-wave expansion

$$\mathcal{A}(s,t) = \sum_{l=0}^{\infty}(2l+1)A_l(t)P_l(\cos\theta_{CM}) \tag{1.26}$$

where l is the total angular momentum, $A_l(t)$ are the coefficients of the Legendre polynomials $P_l(\cos\theta_{CM})$. This t-channel partial wave amplitude can be cast into integral form using the Sommerfeld-Watson transform. This step is where angular momentum becomes a complex number and is the foundation of Regge theory [11, 12]. In relativistic field theory, the mapping of non-negative integer angular momentum values l to complex values [13] is not unique. This requires the introduction of two amplitudes corresponding to odd (-) and even (+) real parts of l. This is known as the signature. Incorporating these requirements, the amplitude can be expressed as

$$\mathcal{A}^{\pm}(s,t) = 8\pi i \int_{\mathcal{C}} \frac{dl(2l+1)}{\sin(\pi l)}\mathcal{A}^{\pm}(l,t)[P_l(-\cos\theta_{CM}) \pm P_l(\cos\theta_{CM})] \tag{1.27}$$

It was shown that the singularities of $\mathcal{A}^{\pm}(l,t)$ in the complex l-plane are poles whose locations vary with t:

$$l = \alpha(t) \tag{1.28}$$

These poles are known as Regge poles or Reggeons and as t varies, they trace out paths parameterized by $\alpha(t)$ in the complex l-plane that are known as Regge trajectories [12].

1.3.3 JML Model

Regge theory makes its connection to scattering theory through the fact that each of these trajectories $\alpha(t)$ corresponds to the exchange of a different family of particles. The model of Jean-Marc Laget et. al., denoted as the JML model from

this point on, has at its foundation the exchange of Regge trajectories in the t-channel [10]. Therefore, the predictive power of the JML model will be in describing the t-behavior of the cross section as well as the scaling of the total cross section with cm energy squared: $\sigma \sim (\frac{s}{s_0})^{(2\alpha(0)-1)}$. The photoproduction of each meson is described by a channel-appropriate sum of exchanges of the four main t-channel Regge trajectories π^0, σ, f_2, and P(Pomeron). These are diagrammatically shown in Figure 1.5. Each of the π^0, σ, f_2, and P exchanges has a corresponding Regge trajectory:

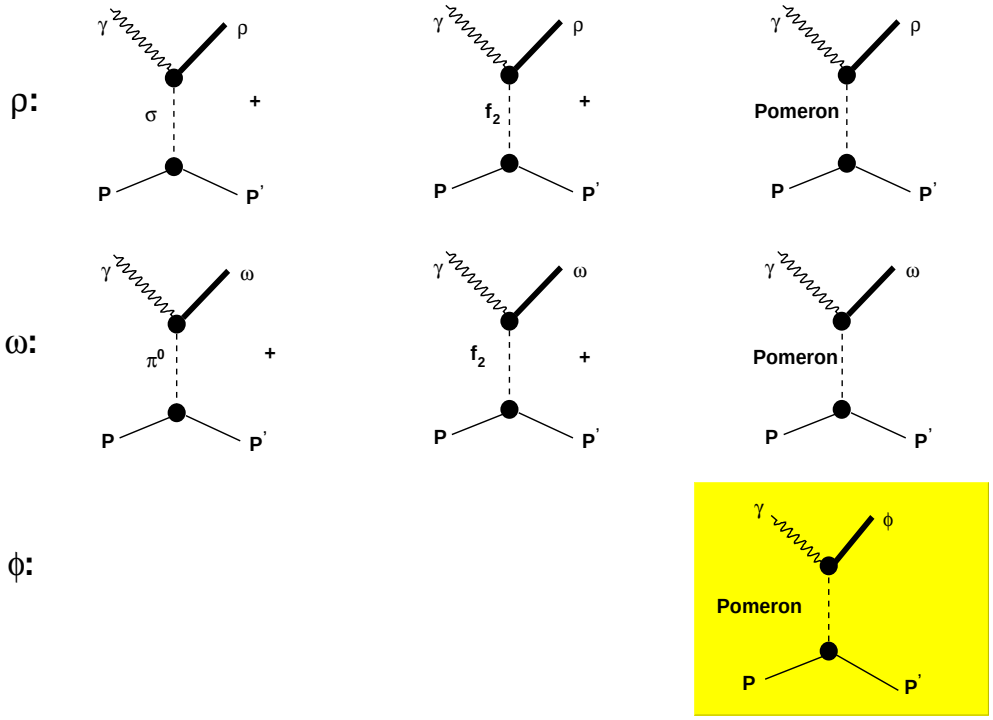

Figure 1.5: Dominant exchange diagrams for ρ, ω, and ϕ electroproduction in the JML model. The ϕ channel is shown highlighted in yellow

The Pomeron trajectory is $\alpha_{\mathsf{P}}(t) = 1.08 + 0.25t$, the f_2 is $\alpha_{f_2}(t) = 0.55 + 0.7t$, the π^0 is $\alpha_\pi(t) = 0.7(t - {m_\pi}^2)$ and finally the σ is $\alpha_\sigma(t) = -0.175 + 0.7t$ [10, 14]. From these trajectories, the Regge propagators $\mathcal{P}_{Regge}$ which are the analogues of the Feynman propagator in the aforementioned amplitude $\mathcal{A}$ can be calculated. For ϕ production

we are concerned with the Pomeron propagator:

$$\mathcal{P}_{Regge} = \left(\frac{s}{s_0}\right)^{\alpha_{\mathrm{P}}(t)-1} e^{-\frac{1}{2}i\pi\alpha_{\mathrm{P}}(t)} \tag{1.29}$$

$s_0 = 1.0$ GeV^2 is a mass scale variable. In contrast to the π^0, σ, f_2 Reggeon family, which is composed of two-quark ordinary meson exchanges, the Pomeron, a reggeon with the quantum numbers of the vacuum (0^{++}), corresponds to the exchange of a glueball. Glueballs can be thought of as complicated color-neutral structures composed entirely of gluons. In the regime $Q^2, -t > 1$ GeV^2 [14], the Pomeron exchange reduces to a simple 2-gluon exchange. The transition from the Pomeron to the non-perturbative 2-gluon regime occurs when the formation process of the Pomeron has no time to develop [14]. The 2-gluon propagator is given by:

$$\mathcal{P}_{2g} = \frac{\beta_0}{\sqrt{\pi}\lambda_0}\mathsf{exp}\left(\frac{l^2}{{\lambda_0}^2}\right) \tag{1.30}$$

l here denotes the total transverse momentum of the exchange gluons and the range parameter ${\lambda_0}^2 = 2.7$ GeV^2 characterizes the spatial scale of the interaction. The coupling of the Pomeron to the quark, or more generally the effective coupling of the gluon to the quark β_0 is set by high energy nucleon-nucleon scattering and assumes the value $\beta_0 \sim 4.0$ GeV^2.

The JML model predictions for photoproduction data of vector mesons reproduces the magnitude of the cross sections up to W$\sim$100 GeV, however, in the range W$\sim$ 10 GeV, the pure Pomeron exchange mechanism is an underestimate of the data. The superposition of the JML predictions over various photoproduction data plotted against W is shown in Figure 1.6. The data shown are from various photoproduction experiments conducted at JLAB, SLAC, CERN, HERA, and Fermi Lab. It is clear from Figure 1.5 that the ϕ channel provides a convenient way of isolating the gluon exchange mechanism, in the cast of Pomeron exchange, from quark exchange mechanisms. This is due to the OZI suppression of quark exchange mechanisms in ϕ production [5]. The data at two different W values corresponding to the HERA energy range (top plot) and the JLAB energy range (bottom plot), are shown in Figure 1.7. As for other vector meson channels, the JML model reproduces the data well up

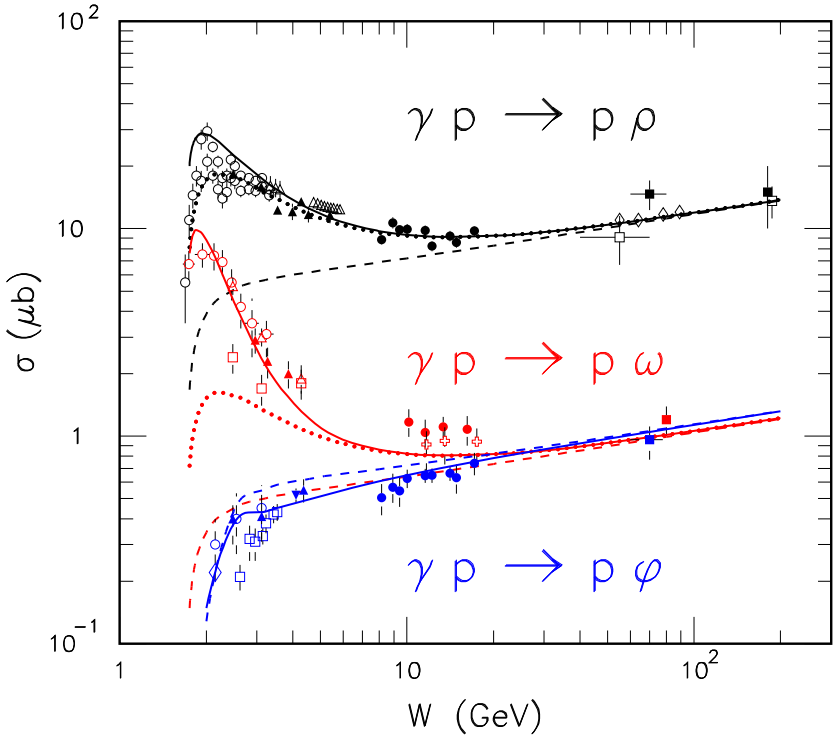

Figure 1.6: Plot shows W dependence of ρ(black), ω(red), and ϕ(blue) photoproduction cross sections. The dashed curves are the JML model predictions for just Pomeron exchange. The dotted curves are Pomeron+f_2 exchange, and the solid curves are the full JML model predictions. Both the JML predictions and cross section data are integrated over angles.

to $-t \leq 0.5$ GeV^2 at high W (HERA) and $-t \leq 1.0$ GeV^2 at low W (JLAB) [14].

1.3.4 Extension of JML to electroproduction

All the predictions of the JML model mentioned thus far were applicable to vector meson photoproduction. The JML model has recently been extended to include vector meson electroproduction as well through methods described in [15]. To extend JML to electroproduction, one must first introduce electromagnetic form factors into the Regge amplitude $\mathcal{A}$ [15], however since the Pomeron couples directly to the quark, there is no associated form factor for this exchange. The Q^2 dependence of the Pomeron as well as the 2-gluon amplitudes is an intrinsic part of its construction. The full forms of these amplitudes are given in reference [14]. Thus far, comparisons of the

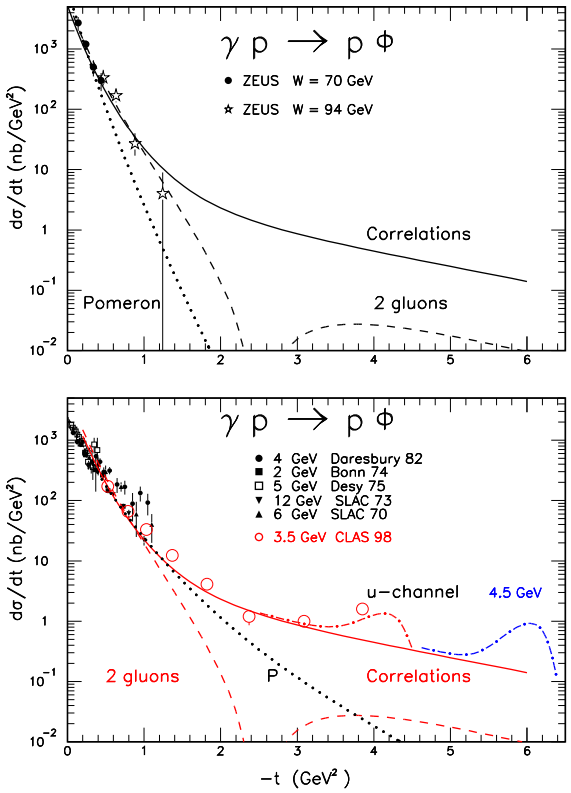

Figure 1.7: Top plot shows $\frac{d\sigma}{dt}$ data from ZEUS at high W superposed with JML model predictions. Bottom plot shows various ϕ photoproduction data measuring $\frac{d\sigma}{dt}$ as well as JML model predictions for pure Pomeron exchange, pure 2-gluon exchange, u-channel (baryon) exchange as well as the full model (Correlations).

JML model for electroproduction have been made with ω[10], and ρ [16] electroproduction data from JLAB, and ρ electroproduction data from HERMES [17, 10, 16]. JML seems to overestimate the W dependence of σ_L, however σ_T is satisfactorily described.

1.4 Generalized Parton Distributions

As Q^2 increases, the resolution of the inelastic probe γ^* is improved in the $\gamma^* N \to PX$ reaction. In this higher Q^2 domain, γ^* becomes sensitive to the internal structure of the nucleon, composed of quarks and gluons. A generalized description of the

momentum and spatial distribution of the partons in the nucleon is encoded in functions called Generalized Parton Distributions(GPDs) [18]. A formalism which unifies exclusive reactions at large Q^2 is by no means a new concept, however through the recent work of Ji, Radyushkin, and Collins, GPDs have acquired a new predictive richness and descriptive form [19]. To first order, GPDs can be classified into two

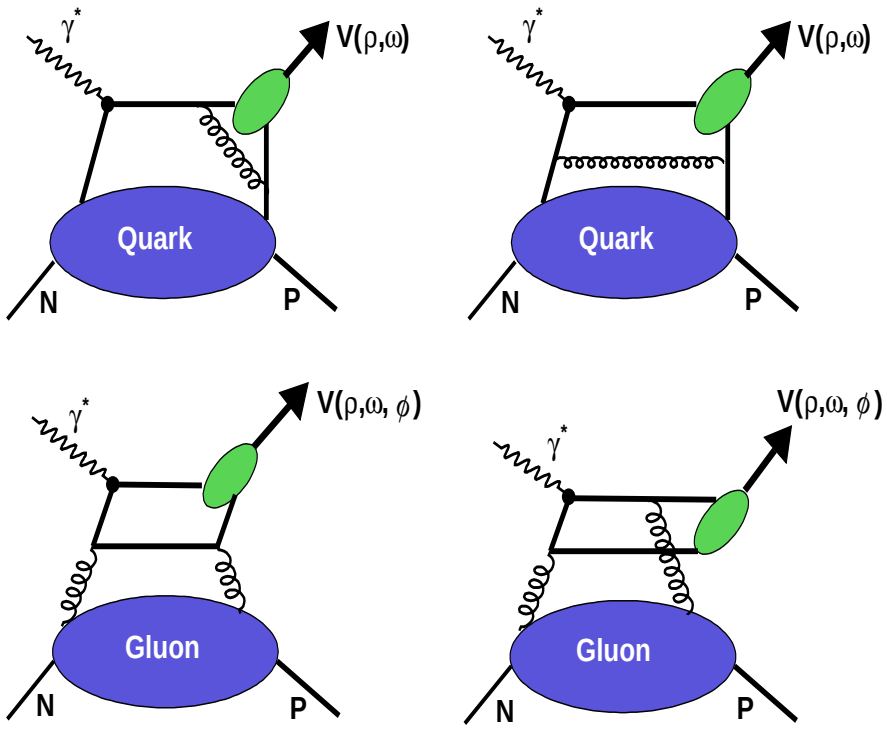

Figure 1.8: Exchange diagrams for meson electroproduction. The top two diagrams are the quark exchange GPDs (blue blobs) and the bottom two are the gluon GPDS.

groups corresponding to quark-exchange GPDs and gluon-exchange GPDs, whose respective graphs are shown in Figure 1.8. This figure also illustrates the particular species of vector meson production to which each of these graphs contributes. It is seen from this figure that for ρ and ω production, both quark and gluon graphs contribute and do in fact contribute almost equally. For ϕ production however, only the gluon graphs contribute due to the OZI suppression of the quark exchange graphs. ϕ meson electroproduction becomes a useful filter for isolating and studying these glu-

onic GPDs. As a result of this, any quark exchange in ϕ production occurs through the $s\bar{s}$ content of the proton wave function, and thus such exchanges are a direct probe of the physics associated with the dynamics of strange sea quarks in the proton [19]. This is the GPD description of the familiar $s\bar{s}$ knockout mechanism described in [20].

1.4.1 Functional Form of the GPDs and Factorization

GPDs describe the soft part of the exclusive meson electroproduction amplitude in the so-called handbag diagrams. These handbag diagrams contain a hard, perturbative part which is exactly calculable within regular perturbation theory as well as a soft, non-perturbative part describing the strong interaction with the partons in the target nucleon. The predictive power of GPDs arises when factorization [21] of the perturbative and non-perturbative parts is valid. To the extent that the virtual photon γ^* is longitudinally polarized and $|t| \ll Q^2$ the amplitude $\mathcal{A}_L$ can be factorized into a perturbative and non-perturbative part (GPD) part. $\mathcal{A}_L$ is the amplitude of σ_L so the experimental access to GPDs will be accomplished through the measurement of the longitudinal cross section σ_L. Assuming SCHC, R can be extracted from the decay angular distribution. Before introducing the explicit form of the amplitudes and associated GPDs, it is appropriate to introduce light-cone coordinates:

$$v^{\pm} = \frac{1}{\sqrt{2}}(v^0 \pm v^3), \quad \mathbf{v} = (v^1, v^2) \tag{1.31}$$

where v is any arbitrary 4-vector with components v^i, $i = 0, 1, 2, 3$.

Following the form used in [19, 22], $\mathcal{A}_L$ can be decomposed into a quark GPD part $\mathcal{A}_q$ and a gluon GPD part $\mathcal{A}_g$. $\mathcal{A}_q$ is given by:

$$\mathcal{A}_q = e\frac{16\pi\alpha_s}{9}\frac{1}{Q}\int_0^1 dz \sum_q e_q \frac{\Phi^q(z)}{z}\int_{-1}^1 dx\, F^q(x,\xi,t)\left[\frac{1}{\xi - x - i\epsilon} - \frac{1}{\xi + x - i\epsilon}\right] \tag{1.32}$$

$\mathcal{A}_g$ is given by:

$$\mathcal{A}_g = e\frac{\pi\alpha_s}{3}\frac{1}{Q}\int_0^1 dz \sum_q e_q \frac{\Phi^q(z)}{z}\int_{-1}^1 dx\, \frac{F^g(x,\xi,t)}{x}\left[\frac{1}{\xi - x - i\epsilon} - \frac{1}{\xi + x - i\epsilon}\right] \tag{1.33}$$

The factorization theorem and its associated variables is elucidated in Figure 1.9. where

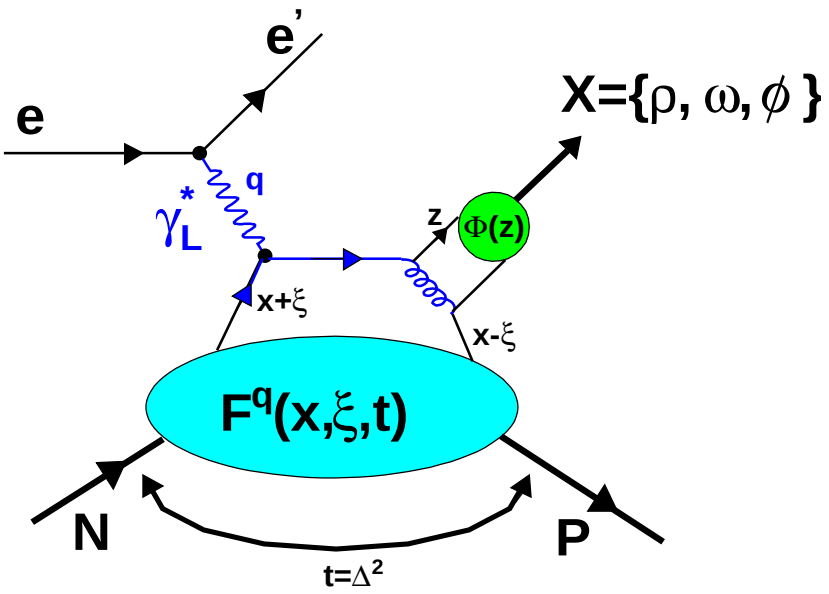

Figure 1.9: Handbag diagram representation of the electroproduction of the vector mesons ρ^0, ω, and ϕ. The lines highlighted in dark blue represent the perturbative "hard" part of the scattering amplitude. The entire non-perturbative part of is represented by the light blue oval. The formation of the vector meson, described by the meson distribution amplitude, is represented by the light green blob. This diagram is the handbag diagram for quark GPDs F^q. A diagram like the bottom two in Figure 1.8 can be drawn for the gluon GPDs F^g.

- α_s is the strong coupling constant and e_q is the quark charge
- $\Phi^q(z)$ is the distribution amplitude of the electroproduced meson which is a function of the 4-momentum fraction z [19]
- The index q describes the quark flavor composition of the electroproduced meson in the amplitude $\mathcal{A}_q$
- ξ is the symmetrized momentum transfer fraction $\xi = \frac{N^+ - P^-}{N^+ + P^-}$ ($N^\pm, P^\pm$ are the light-cone 4-vectors of N and P)
- x is the light-cone momentum fraction carried by the exchange quarks
- $F^{q/g}(x, \xi, t)$ is the non-perturbative part of the amplitude which is a function of the

GPDs $\mathbf{E}, \tilde{\mathbf{E}}, \mathbf{H}, \tilde{\mathbf{H}}$. $\mathbf{E}, \mathbf{H}$ are for vector mesons and $\tilde{\mathbf{E}}, \tilde{\mathbf{H}}$ are for psuedoscalar mesons. The amplitude $\mathcal{A}_q$ is associated with the top two diagrams of Figure 1.8 while $\mathcal{A}_g$ is represents the bottom two diagrams. For ϕ production, the amplitude $\mathcal{A}_q$ is strongly suppressed so the main contribution comes from $\mathcal{A}_g$. The function $F^{q/g}(x,\xi,t)$ are the GPDs describing the nucleon structure. For vector meson electroproduction, it is defined according to [23]

$$F^{q/g}(x,\xi,t) = \mathbf{H^{q/g}}(\mathbf{x},\xi,\mathbf{t})\bar{N}(P)\gamma^{+}N(N) + \mathbf{E^{q/g}}(\mathbf{x},\xi,\mathbf{t})\bar{N}(P)i\sigma^{+\kappa}\frac{{\Delta_\kappa}^{+}}{2M_N}N(N) \tag{1.34}$$

where

• $\bar{N}(P)$, and $N(N)$ are the nucleon spinors (explicitly written in appendix B of reference [19]

• γ^{+} and γ^{5} are the Dirac matrices

• $\sigma^{+\kappa}$ is Pauli matrix. κ is the spinor index.

• $\Delta^{+} = -2\xi P^{+}$ is related to the t-channel momentum transfer ($\Delta^2 = t$) expressed as lightcone 4-vectors

There is a similar expression for $\tilde{H}^{q/g}(x,\xi,t)$ and $\tilde{E}^{q/g}(x,\xi,t)$ which are applicable to psuedoscalar mesons but will not be discussed here. The study of ρ^0, ω, and ϕ electroproduction channels act as a filter for isolating the $H^{q/g}(x,\xi,t)$ and $E^{q/g}(x,\xi,t)$ GPDs. The ϕ channel has the capability of further isolating the gluonic GPDs $H^{g}(x,\xi,t)$ and $E^{g}(x,\xi,t)$.

The amplitude for ϕ electroproduction can be written as the sum of the gluon GPD contribution and a strange quark GPD contribution:

$$\mathcal{A}_\phi \propto F^{g}(x,\xi,t) + F^{s}(x,\xi,t) \tag{1.35}$$

The strange quark GPD contribution to this amplitude, $F^{s}(x,\xi,t)$, is strongly OZI suppressed so the main contribution to ϕ production comes from the gluon contribution. Any strange quark component of the nucleon wave function will however manifest itself through the contribution from $F^{s}(x,\xi,t)$.

1.4.2 Consequences and Results of GPDs

Given that σ_L can be successfully extracted and the requirements of factorization are met, GPDs can yield a tremendous wealth of information concerning the structure of the nucleon as well as the behavior of its constituents. Some predictive aspects of GPD formalism have already been touched upon and some of the more salient predictions will now be discussed [19].

3-D spatial distributions of partons in the nucleon

• Given that the momentum transfer t can have a small component transverse to the nucleon direction, one can obtain information about the transverse structure of the nucleon. When expressed in the impact parameter representation of the GPDs (where the spatial distribution of quarks and gluons in the plane transverse to the momentum of the hadron is given as opposed to the momentum representation of GPDs already introduced), a 3-D picture of the partonic stucture of the nucleon can be constructed.

Spin structure of the nucleon

• A long-standing mystery of nucleon structure is how the total nucleon spin is constructed from its partonic constituents. Reference [24] shows how the nucleon spin can be decomposed into a quark intrinsic (helicity) spin , a quark orbital, and a gluon contribution. Furthermore, it is shown how this total quark spin contribution to the nucleon can be accessed through deeply virtual Compton scattering (DVCS). The total nucleon spin can be decomposed as

$$\underbrace{(\mathsf{S}_q + \mathsf{L}_q)}_{\mathsf{J}_q} + \mathsf{J}_g = \frac{1}{2} \tag{1.36}$$

The contribution S_q is known from inclusive measurements on polarized targets, so using the DVCS reaction will yield L_q and thus the quark contribution to the nucleon spin. Such a measurement is accessible through measurements of ρ^0 electroproduction

by exploiting the relation:

$$J_q = \lim_{t\to 0} \frac{1}{2} \int d\mathbf{x}\, \mathbf{x} \left[\mathbf{H}(\mathbf{x},\xi,\mathbf{t}) + \mathbf{E}(\mathbf{x},\xi,\mathbf{t}) \right] \tag{1.37}$$

at fixed ξ.

Cross section ratio predictions: $\sigma_{\rho^0} : \sigma_\omega : \sigma_\phi$

If one assumes the regular $q\bar{q}$ content of the neutral vector mesons,
$\rho^0 : \frac{1}{\sqrt{2}}(|u\bar{u}> - |d\bar{d}>)$
$\omega : \frac{1}{\sqrt{2}}(|u\bar{u}> + |d\bar{d}>)$
$\phi : |s\bar{s}>$
then the ratio of their production amplitudes can be written as [19]:

$$\begin{aligned}
\mathcal{A}_{\rho^0} : \mathcal{A}_\omega : \mathcal{A}_\phi &= \int_{-1}^{1} \frac{dx}{\xi - x - i\epsilon} \left(\frac{2F^u(x,\xi,t) + F^d(x,\xi,t)}{\sqrt{2}} + \frac{9}{8\sqrt{2}} \frac{F^g(x,\xi,t)}{x} \right) \\
&: \int_{-1}^{1} \frac{dx}{\xi - x - i\epsilon} \left(\frac{2F^u(x,\xi,t) - F^d(x,\xi,t)}{\sqrt{2}} + \frac{3}{8\sqrt{2}} \frac{F^g(x,\xi,t)}{x} \right) \\
&: \int_{-1}^{1} \frac{dx}{\xi - x - i\epsilon} \left(-F^s(x,\xi,t) + \frac{3}{8} \frac{F^g(x,\xi,t)}{x} \right)
\end{aligned} \tag{1.38}$$

This relation leads to predictions about the cross section ratios:
$\sigma_{\rho^0} : \sigma_\omega : \sigma_\phi = 9 : 1 : 2$ in the region at very small x_B where gluon exchange dominates. Otherwise, in the quark-exchange-dominated region, the expected cross section ratio between the ρ^0 and the ω meson is expected to become $\sigma_{\rho^0} : \sigma_\omega = 25 : 9$ as quark exchange becomes more important. The expected ratio to the ϕ cross section does not change as a result of the suppression of quark exchange diagrams in ϕ production.

1.5 Summary of Previous Data and Measurements

One of the leading motivations for completing the present analysis is the sparse amount of existing ϕ electroproduction data. Aside from the previous data in references [2, 25, 3] most of the measurements are at high W ($W > 10$ GeV). A summary of the world data along with kinematical regime of each contributions can be found in

Table 1.1. The data is plotted in Figure 1.10 along with additional photoproduction

Table 1.1: Summary of ϕ electroproduction data

Data Author/Location	Q^2	W	Year
Lukashin/CLAS	0.70 to 2.20 GeV^2	2.0 to 2.6 GeV^2	2001
Airapetian/HERMES	0.70 to 5.00 GeV^2	4.0 to 6.0 GeV^2	2003
Cassel/Cornell	0.80 to 4.00 GeV^2	W= 2.7 GeV^2	1981
Dixon/Cornell	0.23 to 0.97 GeV^2		1977
Adloff/H1	1.00 to 15.0 GeV^2	40.0 to 130.0 GeV^2	2000
Adloff/H1	$Q^2 > 7.0$ GeV^2	W= 75.0 GeV^2	1997
Breitwig/H1	3.00 to 20.0 GeV^2	4.0 to 120.0 GeV^2	2000
Derrick/H1	7.00 to 25.0 GeV^2	42.0 to 134.0 GeV^2	1996

data (Q^2=0 GeV^2).

1.6 Goals and hopes of the present analysis

The objectives of the following analysis are multi-fold and are summarized as follows:

- Extraction of the total cross section $\sigma(Q^2)$

The predictions of the VMD model predict a $\frac{1}{Q^4}$ scaling of the total cross section. A different behavior of $\sigma(Q^2)$ would indicate the contribution of other exchange mechanisms.

- Extraction of the differential cross section $\frac{d\sigma}{dt}$ and $\frac{d\sigma}{dt'}$

The comparison of the measured differential cross section with multiple models requires the extraction of both $\frac{d\sigma}{dt}$ and $\frac{d\sigma}{dt'}$. The comparison of the data to VMD predictions amounts to the extraction of the t-slope parameter b from $\frac{d\sigma}{dt'}$ vs t'. VMD predicts the t-dependent part of the cross section to behave as:

$$\sigma_{t'} \propto A_\phi \, \mathsf{exp}(-bt') \tag{1.39}$$

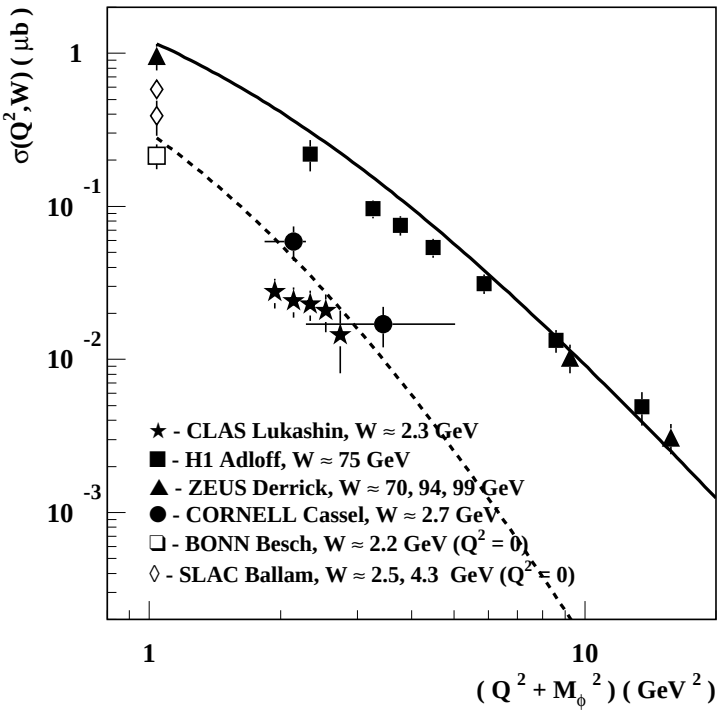

Figure 1.10: Figure shows some of the existing ϕ electroproduction data along with the Pomeron exchange predictions at high W (solid) and low W (dotted line). Also shown are data from two photoproduction measurements ($Q^2 = 0$).

The slope parameter is expected to decrease with increasing Q^2.

The JML model predicts a certain behavior of $\frac{d\sigma}{dt}$ depending upon whether Reggeon (Pomeron) exchange or 2-gluon exchange is the dominant production mechanism. The extraction of $\frac{d\sigma}{dt}$ is complicated by the t_{min} effect (see section 6.3), which must be corrected for before $\frac{d\sigma}{dt}$ vs. t can be plotted. Again, due to poor statistics, the extraction of $\frac{d\sigma}{dt}$ will be extracted in two Q^2 bins for comparison to the JML model predictions at two $< Q^2 >$ values.

- Extraction of R and σ_L from the angular distributions

The $\phi(1020)$ meson is a spin 1 particle which decays into two spin-0 particles: $\phi \rightarrow K^+K^-$. The decay angular distribution $W_D(\cos\theta_H, \psi)$ of the K^+ (or K^-),

provides a complete description of the ϕ polarization [20]. SCHC. will first be tested via the extraction of $\frac{d\sigma}{d\Phi}$. Assuming SCHC, the VMD parameters R and ξ^2 can be extracted with a fit to the assumed angular distribution (Eq. 1.23). The consistency of these parameters can then be gaged relative to previous measurements.

Secondly, assuming SCHC and the successful extraction of R, σ_L (the cross section due to longitudinally polarized photons) can be extracted from σ.

$$\sigma_L = \frac{R}{1+\epsilon R}\sigma \tag{1.40}$$

It is still unclear whether the kinematic regime of the present analysis is compatible with the region of validity of GPDs. The GPD formalism makes predictions about the behavior of σ_L, namely its scaling as a function of Q^2 and t. The extraction of σ_L is tantamount to making a meaningful comparison to the model. It is the hope that at the very least we have entered a transition region where hadronic degrees of freedom give way to quark, and more appropriately gluonic degrees of freedom.

Chapter 2

Experimental Apparatus and CLAS Overview

2.1 Continuous Electron Beam Accelerator Facility

Thomas Jefferson National Accelerator Facility or **TJNAF** in Newport News, Virginia is home to a recirculating linear electron accelerator capable of delivering beam to three experimental halls simultaneously. The accelerator along with some of its components is shown schematically in Figure 2.1. At its heart is a series of superconducting Niobium cavities, five per cryomodule which produce a minimum energy gradient of 5 MeV per meter. A beam of 45 MeV electrons is injected into one of the linacs which are connected on one end by five recirculation arcs and four on the extraction side. Each successive pass through the linacs boost the electron energy by a typical value ΔE where ΔE is about 0.4 GeV per line-ac. With the recent accelerator upgrade, the available beam energies range from 1.140 GeV to 5.70 GeV in multiples of 1.140 GeV.

The electron beam is extracted at the recirculation arcs which allow the three Halls to operate at 3 different but correlated energies simultaneously. As a result of the RF signal structure operating at 1.497 GHz, each beam bunch is separated by about two-thirds of a nanosecond. In other words, the electron beam can be delivered to

each hall at a frequency of 499 MHz with currents ranging from $\sim 100pA$ to $\sim 100\mu A$.

Each of the end stations contain spectrometers which support complimentary experimental physics programs. Two High Resolution Spectrometers (HRS's) with a momentum resolution of $\frac{\Delta p}{p} \leq 10^{-4}$, and a maximum momentum of 4 GeV/c make their home in Hall A. Hall C contains two medium resolution magnetic spectrometers, each with a $\frac{\Delta p}{p} \leq 10^{-4}$ but each with a different maximum momentum. The Short Orbit Spectrometer (SOS) has a maximum momentum of 1.8 GeV/c while the High Momentum Spectrometer (HMS) has a maximum momentum of 7 GeV/c. Experimental Hall B is home to CLAS or SELF Large Acceptance Spectrometer. The CLAS detector is dedicated to the measurement of multi particle final states and will be discussed in great detail in the following section.

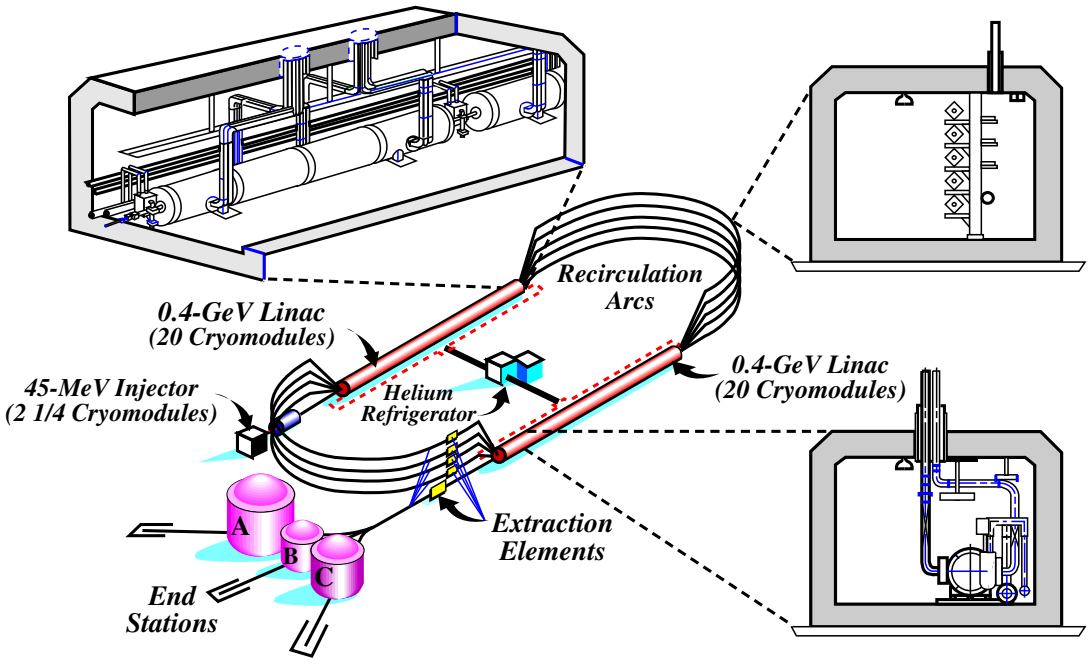

Figure 2.1: Schematic layout of the CEBAF accelerator.

2.2 CEBAF Large Acceptance Spectrometer, An Overview

The CEBAF Large Acceptance Spectrometer or CLAS detector, as shown in Figure 2.2 in experimental Hall B, is nearly a 4π acceptance detector. Its design is based on a toroidal magnetic field generated by six (6) superconducting kidney-shaped coils. The detector's primary requirements include the ability to measure charged particles with good momentum resolution while also providing geometrical coverage of charged particles to large laboratory angles. CLAS is separate into six (6) sectors which effectively act as six independent magnetic spectrometers with a common target, trigger and data acquisition system or **DAQ** [26].

The detector consists of a set of drift chambers to measure particle trajectories and momenta, gas Cerenkov counters for electron identification, scintillators that measure the time of flight of particles and electromagnetic calorimeters that measure energy deposition of showering particles ($e's$ and $\gamma's$) and neutrons.

The CLAS detector can operate in a mode with either a pure electron beam or a pure photon beam. During operation in electron mode, a normal-conducting mini-torus surrounds the target to sweep away low-momentum Möller electrons produced in the target. While operating in photon mode, the mini-torus is replaced by a scintillator-based start counter which provides fast input to the trigger and the correct start time for the time of flight (**TOF**) counters.

The trigger in CLAS is multi tiered, making use of multiple levels of information in the detector at once. The **Level 1** trigger utilizes fast information from the TOF, the Cerenkov, and the electromagnetic calorimeters. In addition to this, the **Level 2** trigger uses hit patterns in the drift chambers to create rudimentary particle tracks. Once the data is digitized, the data acquisition collects and stores it for subsequent offline analysis.

Each subsystem will be discussed in further detail in the sections to follow.

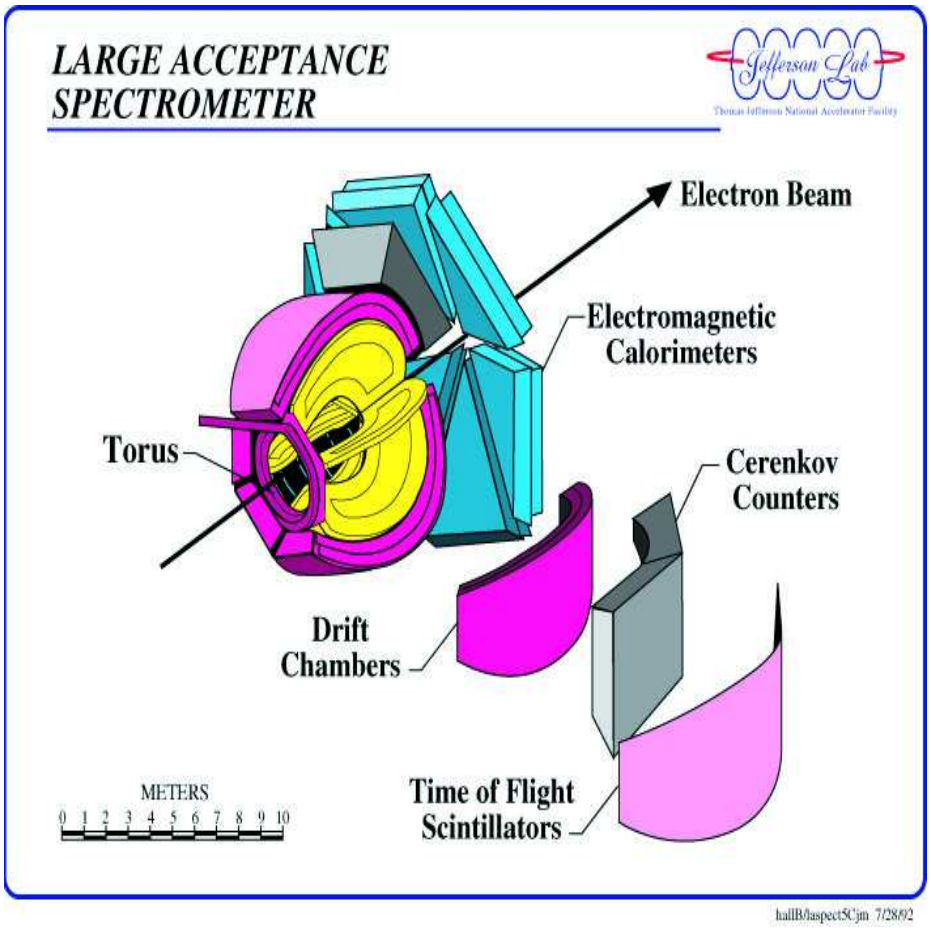

Figure 2.2: The CLAS Detector in Hall B.

2.2.1 Torus Magnet

As previously mentioned, the magnetic field in CLAS is produced by six superconducting coils arranged to produce a toroidal magnetic field around the electron beam. This arrangement, as illustrated in Figure 2.3, produces a magnetic field directed mainly in the ϕ or azimuthal direction.

There are deviations from a pure ϕ field close to the coils, however, deviations on the particle trajectories in these regions is minimized by the circular inner shape of the coil. This is due to the fact that particle trajectories coming from the target will be perpendicular to the inner coil face. The maximum design current of the

Figure 2.3: The Superconducting Torus.

coils is 3860 Amperes. At this current, the magnetic field integral in the forward direction reaches 2.5 Tesla-meters while at a scattering angle of 90 degrees, the field drops to 0.6 Tesla-meters. To avoid out-of-limit mechanical stresses on the coils and its support structure, operation of the torus has been limited to 87% of maximum current or 3375 A. Each of the six coils consists of 4 layers and 54 turns of aluminum-stabilized NbTi/Cu conductor. They are cooled to 4.5 K by forcing super-critical helium through cooling tubes. This supercooling is maintained by a intermediate liquid-nitrogen-cooled heat shield and super insulation.

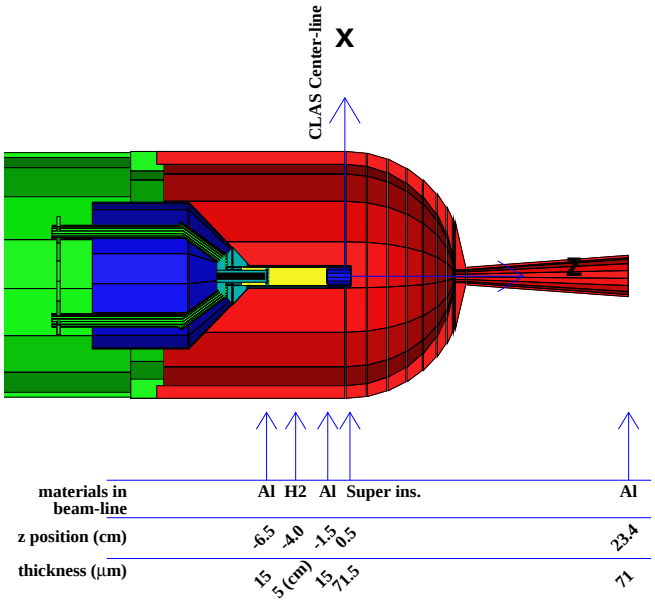

Figure 1: *Horizontal cross–section of the scattering chamber, target cell and superinsulation. The interior of the scattering chamber is made vacuum, which extends for ∼60 cm upstream of the target centre. The materials referred to by the different colours are explained in table 1.*

Figure 2.4: Horizontal Cross Section of e1-6 Target

2.2.2 Cryogenic Target

The target used in the e1-6 experiment was a cryogenic liquid hydrogen target. A diagram of its horizontal cross section is illustrated in Figure 2.4 [27]. The target cell is 5.0 cm long with a radius of 1.5cm. The cell walls were constructed of 128 μm Kapton. The two target windows had radii of 5 cm and were made of 15 μm thick Aluminum. During the course of the experiment, empty target runs were taken to measure container contributions to the H_2 cross section. The target pressure and temperature were continuously monitored while data were accumulated and their values recorded in an on line database.

2.2.3 Drift Chambers

Particle tracking and momentum information is made possible by the CLAS Drift Chambers. The drift chamber system consists of three (3) chambers placed in increasing radial positions in each of the six sectors to give a total of 18 separate chambers. The radial locations are referred to as "Regions" where Region 1 is located closest to the target in an area of low magnetic field, Region 2 is situated between the coils in a region of high magnetic field and finally Region 3 is located radially the furthest from the target and outside the coils. This is illustrated in Figure 2.5. Each region

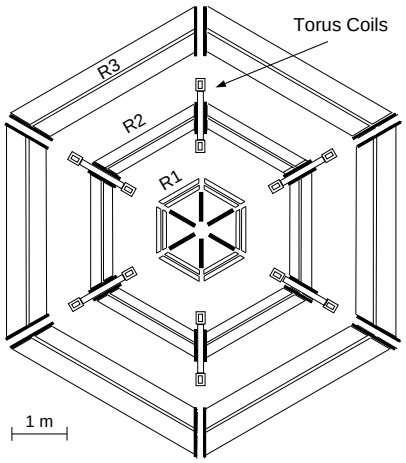

Figure 2.5: Vertical cut through the drift chambers transverse to the beam line at the target location.

is divided into two superlayers consisting of six layers of hexagonally arranged field wires to produce a total of 35,148 individually instrumented hexagonal drift cells. The field wires consist of a 140 μm gold-plated aluminum kept at high voltage. At the center of each of these hexagonal field wire cells is a 20μm diameter gold-plated tungsten sense wire. The wires in one superlayer in each region are arranged axially with respect to the magnetic field (the axial layer) while the wires in the second superlayer are oriented at a 6° stereo angle with respect to the radial direction.

The chambers were filled with a gas mixture of 90% Ar, 10% CO_2. As a charged particle passes through the gas, it ionizes and the liberated electrons are guided to the sense wire(s) via the total electric field produced by the field wires, sense wires, and

guard wires. The sense wires nearest to the particle's trajectory fire and register hits along the trajectory. This is the basis of particle tracking in CLAS. The time it takes for the liberated electrons to arrive at the sense wire can be used to determine the total drift distance between the particle track and the sense wire. This is accomplished by using an experimentally predetermined drift-time to drift-distance function. The

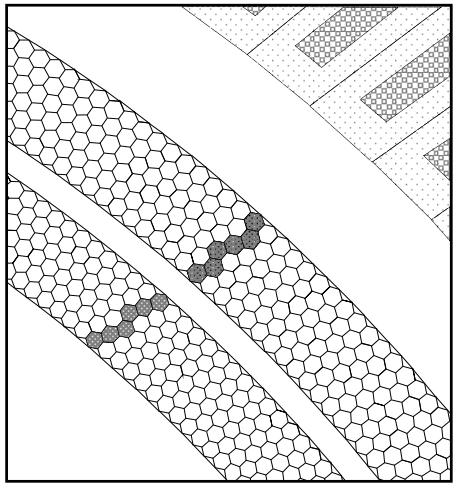

Figure 2.6: Representation of a portion of a Region 3 sector showing the layout of its two superlayers. The hexagonal granularity is drawn as a guide. Each cell is an electrostatic boundary formed by the field wires. The sense wires are at the center of each hexagon while the field wire lie at the vertexes of each cell. The highlighted cells show a particle's trajectory through the two superlayers and the corresponding wires that fired. Beyond the drift chambers, the Cerenkov counter is shown.

drift chambers were designed to provide a $\delta p/p \leq 0.5\%$ (momentum resolution) and a $\delta\theta, \delta\phi \leq 2$ mrad (angular resolution). These design criteria were tested using electron-proton elastic scattering. These studies yielded a $\delta p/p \approx 1-2.5\%$ and a $\delta\theta, \delta\phi \approx \pm 10$ mrad. Both the electron and proton tracks contribute to the errors in this study so that for a single track, the resolution is expected to be closer to the design criteria rather than those measured in elastic scattering experiments.

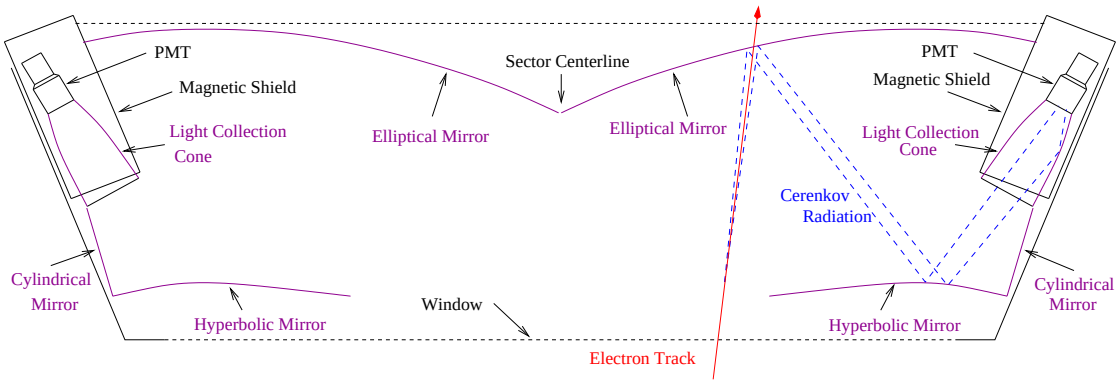

Figure 2.7: Schematic representation of Cerenkov segment. An electron track is shown along with the path of the reflected Cerenkov light.

2.2.4 Cerenkov Counters

The Cerenkov counters are used primarily for electron identification, separating pions from electrons, and as a means of triggering on electrons. It is comprised of six identical threshold counters allocated one per sector. Each of these six counters provides a polar angle (θ) coverage from 8° to 45° along with nearly full coverage in ϕ. The counter is constructed of two side walls in the same plane as the magnet coils, a cylindrical section near the beamline and in the vicinity of the vertex, and a "45-degree wall" made of a highly durable and lightweight material called GreySeal. The entrance window to each counter is made from a sandwich's of $10\mu m$ Mylar surrounded by $2\mu m$ Teldar [28].

The radiator material used is Perflorobutan (C_4F_{10}) maintained at 0.2% above the ambient atmospheric pressure. Perflorobutan's attributes as a heavy (10x that of air), non-flammable, and ultra-violet transparent gas qualify it as a very effective radiator. As a charged particle passes through the gas ($n = 1.00153$), it emits Cerenkov light if its velocity exceeds the threshold value (c/n). This light is collected by the elliptical, hyperbolic, and cylindrical mirrors. This ordering reflects the sequence in which the Cerenkov light hits them. The arrangement of the mirrors optimizes light collection by the PMTs.

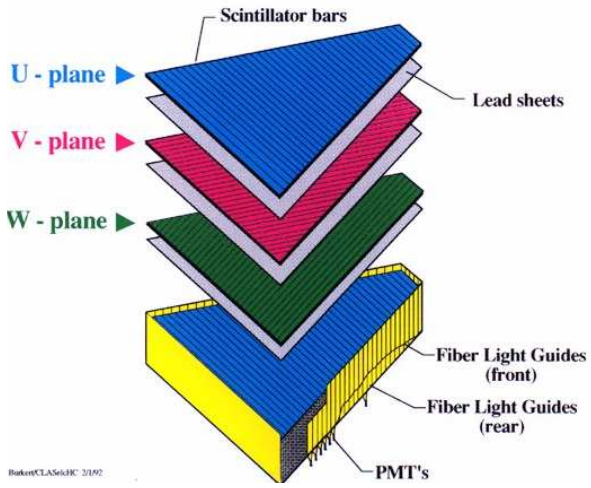

Figure 2.8: Exploded view of one of the six CLAS electromagnetic calorimeter modules.

2.2.5 Time of Flight

The purpose of the Time of Flight (TOF) system is to measure the flight time elapsed from the event start time to the time when the particle arrives at the TOF counter. The TOF system contains 288 "logical" counters amounting to 48 per sector as well as read-out electronics and a laser calibration system. The TOF system will be elaborated upon further in chapter **3** because its maintenance and calibration were a substantial part of the author's work here at Jefferson Lab.

2.2.6 Electromagnetic Calorimeter

The forward electromagnetic calorimeter serves several purposes including the detection of and the triggering on electrons of energy greater than 0.5 GeV, the detection of photons of energy above 0.2 GeV and the detection of neutrons.

Each sector of CLAS contains a wedged-shaped section of the EC consisting of 39 lead-scintillator layers equaling 16 radiation lengths of material and providing a θ coverage between 8° and 45° (Figure 2.9). Each layer contains 10-mm thick scintillator divided into 36 scintillator paddles followed by a 2.2-mm antimony-doped lead sheet. The EC utilizes a "pointing" geometry with each wedge pointing to the nominal target

position. With this configuration, the area of each successive layer increases linearly with distance. Each successive layer is rotated by 120° relative to the previous, which provides 3 orientations or views denoted by U,V, and W (Figure 2.8). This gives 13 layers of each orientation where the first five of these layers are denoted as the "inner" stack and the remaining eight comprise the "outer" stack. The 36 paddles per layer are read out using one 1296 XP2262 PMT in one of the 3 views. The average energy resolution of the EC is comparable to its design value of

$$\frac{\sigma(E)}{E} = \frac{10}{\sqrt{(E)}}\%$$

In the e1-6 experiment, the deposited energy was used in the trigger in coincidence with an above-threshold signal in the Cerenkov in the same sector. The relation between the EC hardware threshold, which was used for triggering, and the corresponding electron energy (**Egyian CLAS NOTE**) is given by:

$$EC_{Thr}(MeV) = 214 + 2.47 \times EC_{Thr}(mV) \tag{2.1}$$

2.3 CLAS Electronics and Data Acquisition

2.3.1 Overview

The gathering of data in CLAS occurs in two stages and thus is comprised of two main components. The first is the large array of hardware including discriminators, amplifiers, ADC's (Analog to Digital Converter), TDC's (Time to Digital Converter), multiplexers (fan outs, fan-ins) and miles of cabling responsible for digitizing, streaming and filtering the data. The data is then streamed to the second component, the software and computer hardware that comprise the Data Acquisition system or **DAQ**, responsible for collection, monitoring, and storage of the data.

2.3.2 Detector and Trigger Electronics

For compatibility's sake, most of the subsystem readout electronics in CLAS are the same type. Most analog signals are digitized using commercial FASTBUS mod-

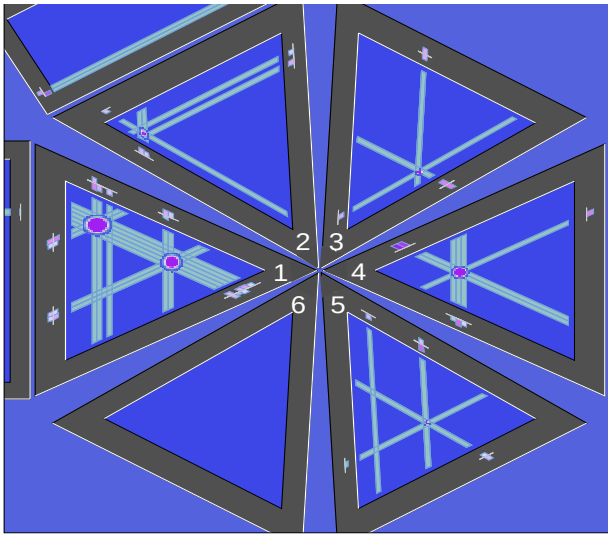

Figure 2.9: The arrangement of scintillator wedges in each sector. View is shown with the beam direction into the page. Also shown is the event reconstruction. The ovals depict the calorimeter-reconstructed location of the passage of a showering particle. The size of the ovals denote the transverse energy spread in the shower.

ules, although recently there has been a gradual integration of VME modules into some of the newer detector components as they have become available. These VME crates are used for the scaler readouts of the various detector subsystems as well as for the polarimeter readout.

The signals from the drift chambers are read out using LeCroy 1877 pipeline TDCs. The timing information of two wires is multiplexed into one thereby reducing the total number of modules required by a factor of two. The signal times from the PMT-based detectors are digitized using LeCroy FASTBUS 1872A TDCs while the signal amplitude is digitized via LeCroy 1881M ADCs. The high-resolution TDCs are needed to achieve the desired timing resolution for TOF measurements. The ADC information is used to determine the amount of energy deposited in each detector and to perform the Time-Walk correction. This will be further elaborated upon in the section of this paper dealing solely with the TOF detector.

CLAS uses a multilevel, hierarchical trigger system divided into two levels: **Level 1** and **Level 2**. The Level 1 trigger is designed to select candidate events using any

or all prompt information from the PMT channels within a 90 ns period. This information includes signals in the Cerenkov detector used for electron identification, the general location of hits in the TOF detector and energy deposition in the calorimeter. The signals are processed in the trigger supervisor (TS) module through which they are responsible for providing the common start signal for the PMT TDCs, the integrating gate signal for the PMT ADCs and the common stop for the drift chamber TDCs. In order to facilitate the fast response of the Level 1 trigger system, bit patterns from these detector subsystems are compared to pre-loaded bit patterns in memory tables.

Events lacking a matching particle trajectory in the drift chambers, such as cosmic-rays can satisfy the Level 1 trigger. In order to minimize these occurrences, the more sophisticated Level 2 trigger system was developed to find "likely tracks" in the drift chamber system. This process is initiated by finding track segments in five superlayers in each sector, excluding the region 1 stereo superlayer. Drift chamber hits are compared with nine templates designed to catch all tracks traversing a superlayer up to an angle of 60°. In its present form the Level 2 trigger identifies a "likely track" in a given sector when track segments are found in at least three of the five used superlayers.

The next step in the CLAS electronics chain is the Trigger Supervisor (TS) board, a custom-designed electronics board that takes the Level 1 and Level 2 trigger signals as input and produces all common signals, busy gates, and resets required by the detector electronics. The TS has a total of twelve inputs, the first eight of which are used for the Level 1 triggers. The remaining four are used for assorted calibration triggers. In addition to these twelve inputs, there exists an input for the Level 2 trigger confirmation. The TS can operate in two modes, CLASS1 which requires only a Level 1 trigger input or CLASS2 which requires both a Level 1 input and a Level 2 trigger confirmation.

2.3.3 Data Acquisition

The CLAS data acquisition system or DAQ was commissioned in 1997 and originally designed for an event rate of 2kHz. The gradual development and dedicated

improvement of the DAQ has allowed it to accommodate event rates between 3 and 4kHz for the 2000/2001 run period. As was previously mentioned, the DAQ is the second and final component of the CLAS data accumulation process. Data from the assorted subsystem electronics is digitized in 24 VME or FASTBUS crates and these signals are gathered by the 24 VME Readout Controllers (ROC1 to ROC24). This digitized data is then translated into tables in which the up-to-16-bit data values are associated with a unique number tagging and describing the active subsystem in the detector. These "event fragments" are buffered and transfered to a the CLAS Online acquisition computer (CLON10) where they are processed in three primary stages. First the Event Builder (EB) takes these event fragments and builds complete events. The individual data tables are prefixed by headers to form "banks" with alphanumeric names, and tagged with an event and run number contained in a header bank (HEAD). In this form, the data is ready for offline analysis. The EB system passes the data to the Event Transfer system (ET) which manages shared memory on the CLON system, allowing for the data to be utilized by several simultaneously active event producer and consumer processes. The data stream is transferred to remote ET systems (ET2 & ET3) which check the raw data, display hits and perform some rudimentary track reconstruction (online RECSIS). The final link in the data collection daisy-chain is the Event Recorder (ER) system which collects all events for permanent storage on magnetic tape. The data is stored on local RAID disks before being transferred to the computer center's tape silo, a kilometer away, on a dedicated fiber connection. This entire process is represented schematically in Figure 2.11.

2.3.4 CEBAF Online Data Acquisition

The successful flow of data in CLAS from detector to tape is contingent upon the seamless communication of some 100 processes running on a system of processors in the Hall and linked to two Symmetric Multi-Processor (SMP) computers and assorted workstations in the control room. The organizational framework which makes this communication possible is the CEBAF Online Data Acquisition (CODA) system. Accessed through a front-end RUN CONTROL GUI, the CODA system is responsible for the configuration and execution of data runs. This includes the downloading of all

crucial values and executable software to the VME crates as well as the initialization of such processes as the EB, ET, and ER components among many others.

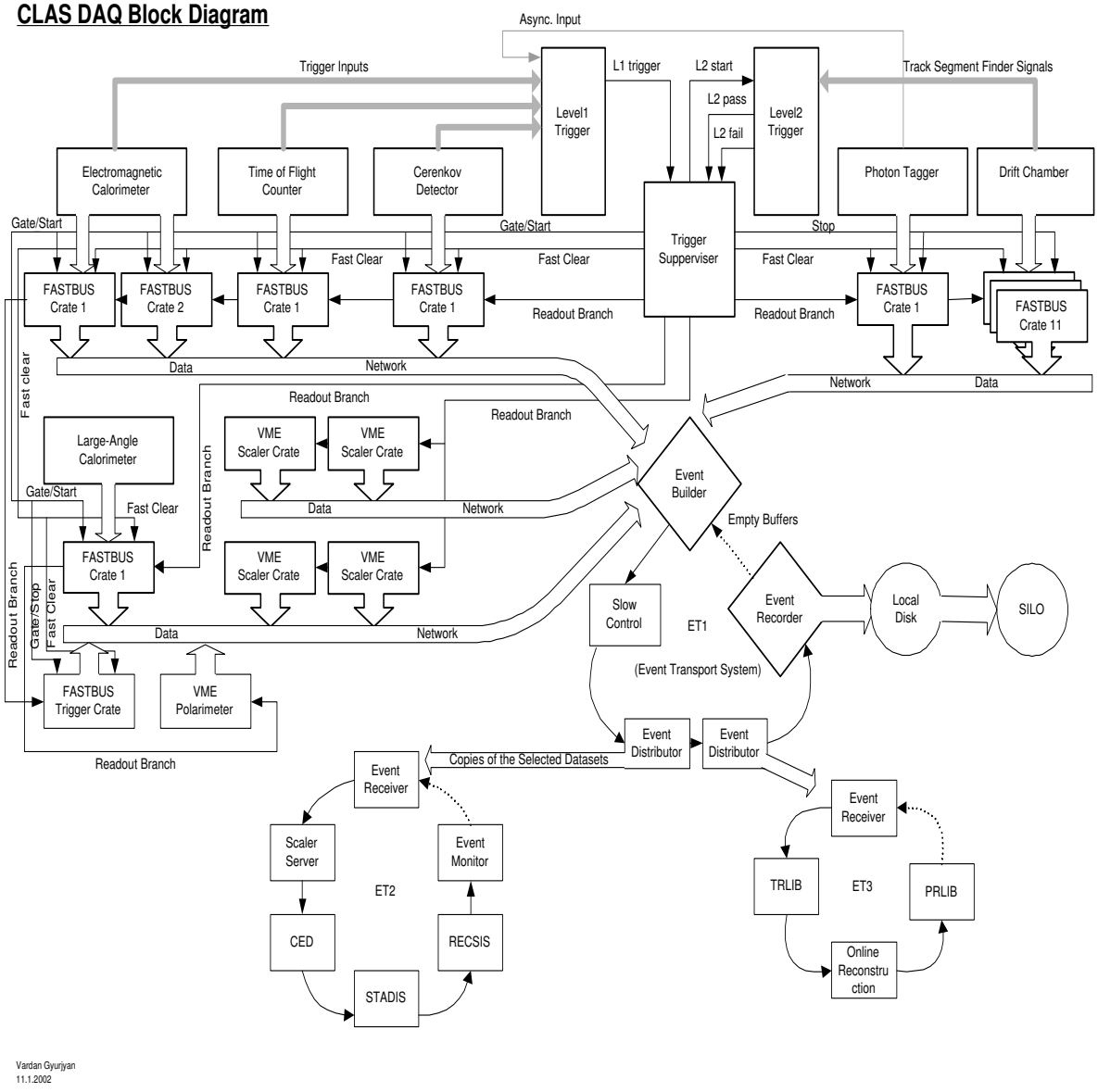

Figure 2.10: Diagram showing the flow of data from its collection points at the various detector subsystems to its collection and storage.

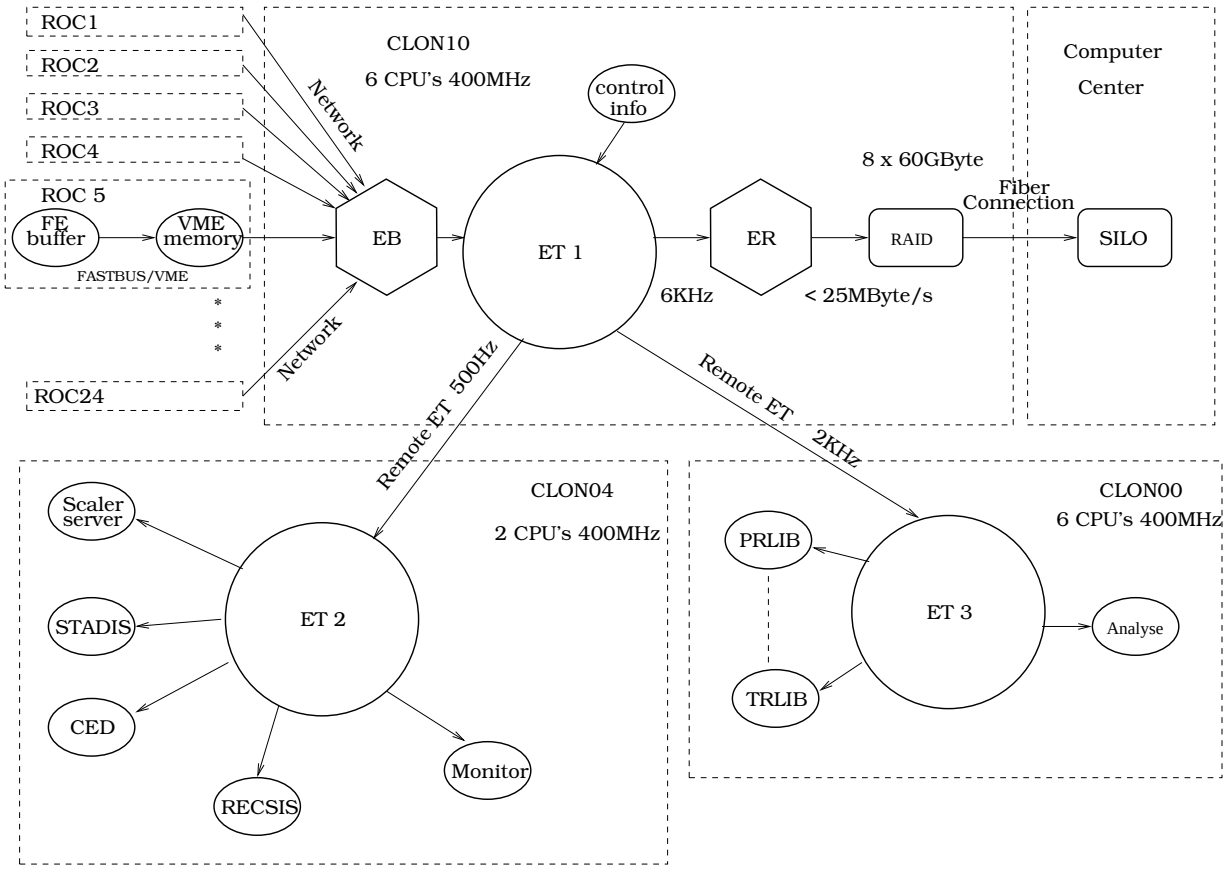

Figure 2.11: A schematic diagram showing the CLAS data flow from the $EB \rightarrow ET \rightarrow ER$ Also shown are the ancillary ET systems (E2 & E3) used for monitoring.

Chapter 3

Time of Flight Detector

3.1 Overview

The design of the TOF system is based on rectangular scintillator bars with a photomultiplier tube (PMT) at each end. The TOF system consists of 57 scintillator bars per sector providing angular coverage in the lab from 8° to 142° in θ and almost a full coverage in the azimuthal direction, ϕ. The TOF system is located between the Cerenkov counter and in front of the electromagnetic calorimeter as viewed from the center of CLAS. The PMTs and light guides are positioned in a way such that they occupy the inactive regions behind each of the superconducting magnet coils. The counters are mounted on four flat panels spanning each of the six sectors. Scintillators 1-23 are mounted on the Panel 1 and are commonly referred to as the "Forward-Angle" counters because they detect particles at scattering angles of less than 45°. Panels 2,3, and 4 support the "Large-Angle" counters. In order for the counters to yield a large signal from minimally-ionizing particles compared to background, the thickness of the counters is a uniform 2 in (5.08 cm) throughout. This 2 in thickness also matches the 2-in PMTs chosen for the forward-angle counters. The scintillators are all arranged perpendicular to the beam direction in a manner such that the width of each counter subtends $\sim 2.0°$ of scattering angle. The counters are parallel to the axial drift chamber wires while spanning nearly the entire ϕ range in each sector.

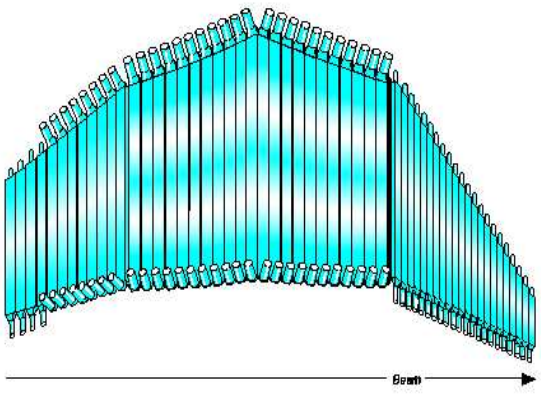

Figure 3.1: View of the TOF counters in one sector showing the panel grouping

3.1.1 TOF Counters

Each counter employs an organic polymer scintillator, Bicron BC-408, and two Thorn EMI 9954 PMTS for the forward counters or two Phillips 4112B/D2 PMTs for the large-angle counters. Due to the length of the longer, large-angle scintillator bars ($\geq$ 300 cm), a material with low light attenuation was needed. In order to achieve the desired timing resolution, the chosen scintillator material also had to have a fast time response. Bicron was chosen as the scintillator material because it satisfied both of these requirements as well as being cost-effective. Good particle identification was one of the main original design goals of the TOF system. The reconstructed time of each scintillator is given by

$$\bar{t} = \frac{(t_L + t_R)}{2} \tag{3.1}$$

where t_R and t_L are the times from the right and left phototubes respectively. Hence, the readout of both counters reduces the timing uncertainty of each scintillator bar by a factor of $\frac{1}{\sqrt{2}}$, thus improving the kaon-pion separation for instance. Further improvement to the TOF resolution can be made in software, for example by using the RF time to specify the event start time. This is described in more detail later when the multistage calibration procedure is discussed.

3.2 TOF Electronics

The TOF system slow controls are responsible for providing the high-voltage power for the PMTs and the TOF system electronics are responsible for the collection and processing of the PMT signals. The high-voltage for the PMTs ($\sim$ 2000 Volts each) are provided by 5 LeCroy 1458 mainframes which can be remotely controlled using the Experimental Physics Industrial Control System (EPICS) in the Counting House (the nerve-center for the detector). The light signal emanated from the scintillator is guided to the PMT via a light guide, and the signal of the PMT is collected by a custom-designed voltage divider. The schematic for the 2-in tube is shown in Figure 3.2 (The divider used for the 3-in tube is very similar). The gain of each PMT is stabilized by four Field-Effect Transistors (FET) which protects the circuit in the event of a current spike. The output of the TOF counters are prompt signals used for input into the Level 1 trigger as well as signals for pulse-height (Energy) and timing analysis. The anode signal is split into two signals using a splitter. One goes to a LeCroy 1881M ADC for energy deposition analysis while the other is the input to the LeCroy 2313 discriminator. The time of the event is recorded by a LeCroy 1872A FASTBUS TDC. The inverted dynode signal goes to a pretrigger circuit which produces two signals. One is for the Level 1 trigger and the other is used as a gate pulse for the discriminator preceding the TDC. The flow of a signals from the PMT anode and dynode are shown in Figure 3.3.

3.2.1 Discriminators

The discriminators chosen for the TOF system are leading-edge rather than constant fraction discriminators. Although the timing of constant fraction discriminators is initially superior to their leading edge counterparts, offline timewalk corrections can be performed that give comparable results and at a substantially reduced cost. The LeCroy 2313 leading-edge discriminator was chosen because of the system's need for a many-channel discriminator with low cross-talk.

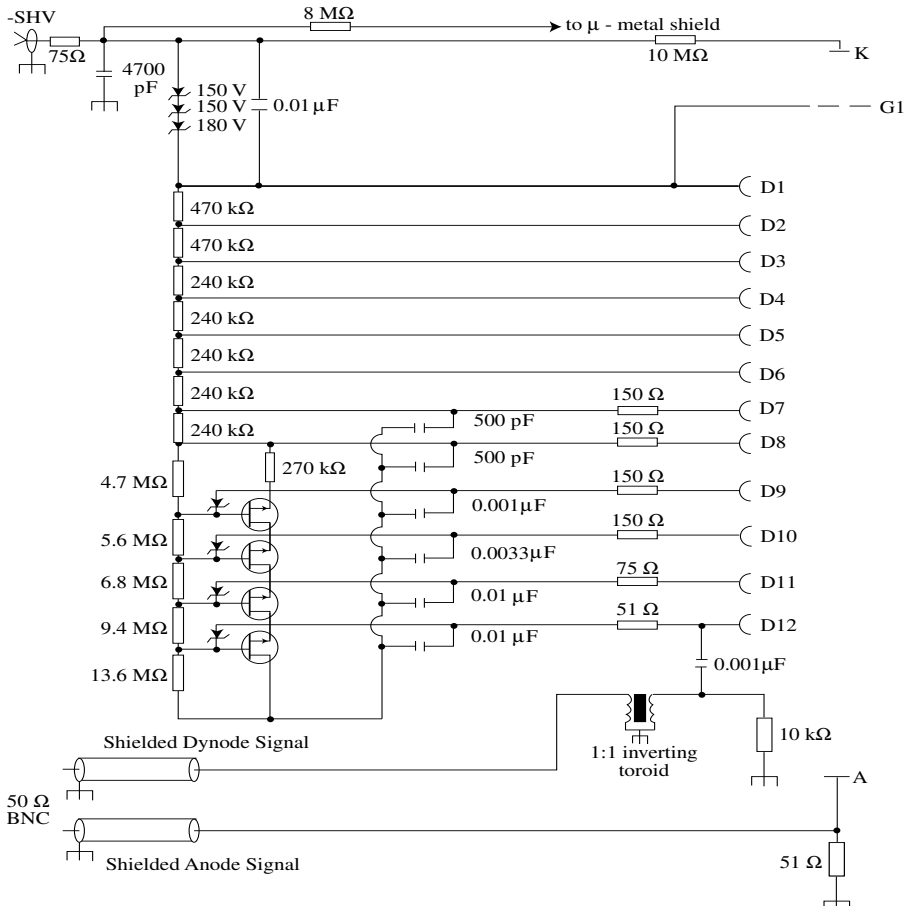

Figure 3.2: Schematic diagram of the high-voltage divider for the TOF PMTs.

3.2.2 Time to Digital Converter

The LeCroy 1872A Mod 100 time-to-digital converter was chosen as the TOF TDC module. This unit is a 12-bit, 64-channel, single-width FASTBUS module. This original version of this hardware was modified from its original form to fulfill certain requirements of CLAS, for instance the dependence of any time measurement on the activity in other (adjacent) channels was required to be less than one count.The module was required to have a conversion time of less than $5\mu s$. The 1872A Modules have a conversion time of 10 plus $2.7\mu s$ per hit channel.

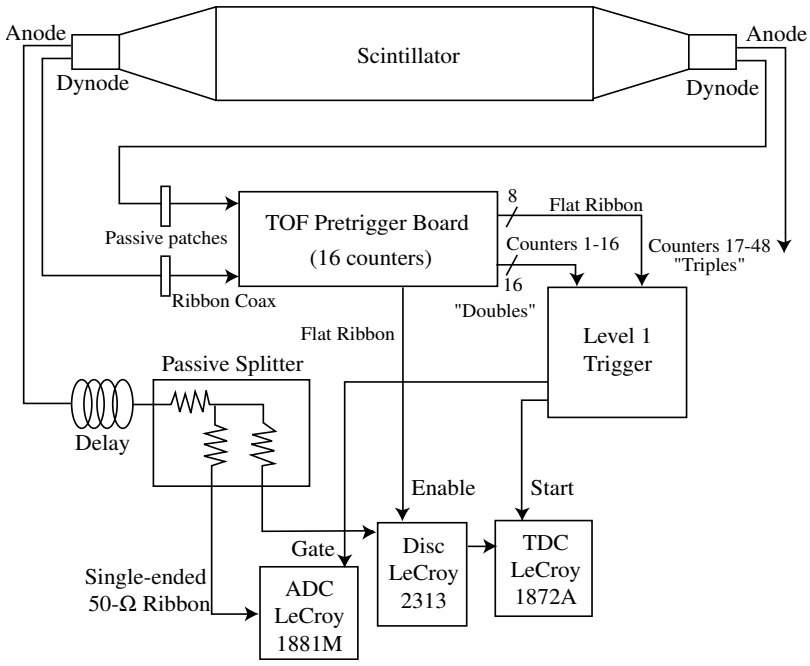

Figure 3.3: Overall schematic of the TOF electronics.

3.2.3 Analog to Digital Converter

The LeCroy 1881M Analog-to-digital converter FASTBUS module was chosen as the TOF ADC module, responsible for measuring and recording the integrated charge of the PMTs. The 1881M is a 13-bit, 64-channel module with a fixed conversion time of 12 μs.

3.2.4 Pretrigger

A custom-designed circuit called the pretrigger board, which sums the PMT dynode signals from both ends of a counter is one of the main components of an efficient trigger. Since particles traveling in curved trajectories can deposit energy in adjacent counters as well, the pretrigger board must also sum the signals of adjacent counters to obtain an amplitude proportional to the total energy deposited. This circuit is shown schematically in Figure 3.4 . The signals from counters 1-16 are the OR of two

adjacent counters and are called the “doubles”. Fine granularity is not required in the large angles, so to reduce the total number of input lines to the Level 1 trigger, the “doubles” are combined for channels 17-48 to produce “triples”. This can be done with little worry of including accidentals due to the decreased rate in the large-angle counters. The pretrigger discriminator has two outputs. The first is scaled and used as input to the Level 1 trigger. The second output is used as an enable to the fast (low-level) discriminator preceding the TDC.

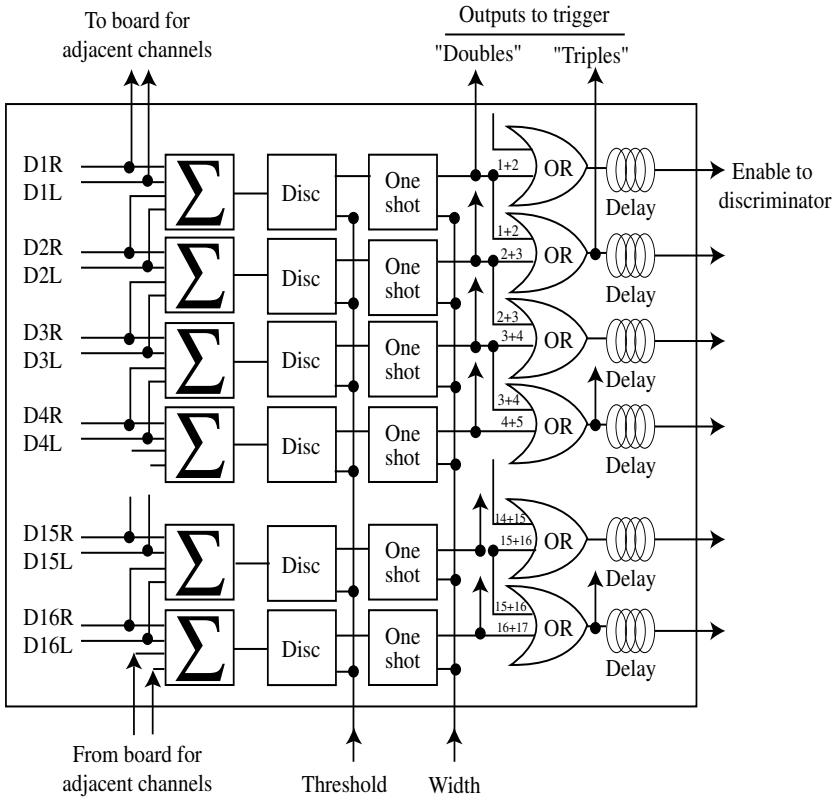

Figure 3.4: Logic diagram for the pretrigger circuit.

3.3 CEBAF RF Structure

As previously mentioned, the CEBAF accelerator is based on superconducting accelerating cavities operated at a highly stabilized frequency of $1.497 \times 10^9\ sec^{-1}$. Electrons ride on the crest of the RF field wave with a bunch length of a few picoseconds. Every third bunch is directed to one of the experimental halls creating a train of electrons equally spaced by 2.004 ns.

3.4 Hardware Adjustments: Gain Matching

In order to normalize the response of the TOF paddles, a gain-matching calibration is required. This calibration ensures that each counter contributes equally to the trigger for a common-threshold discriminator level. This is accomplished by adjusting PMT voltages such that the energy deposited by a normally-incident MIP (Minimally Ionizing Particle) produces a peak at ADC channel 600 after pedestal subtraction. The measured pulse height in each counter subtracted by the pedestals is given by

$$\begin{aligned} A_L &= kE_L e^{-y/\lambda} \\ A_R &= kE_R e^{+y/\lambda} \end{aligned} \tag{3.2}$$

where $A_{L/R}$ is the pedestal-subtracted ADC value, k is an conversion factor between energy and ADC Channels ref[29]), $E_{L/R}$ is the energy deposited in the counter as measured by the left/right PMT, λ is the attenuation constant for the counter, and y is the position of the hit along the counter whose zero is at the center of each scintillator. First the position-independent pulse height distribution $E = \sqrt{E_L \cdot E_R}$ is obtained for each scintillator bar via a fit. The log of the ratio of the right ADC to left ADC $\ln \frac{A_L}{A_R}$ is then used to separate the contributions from each PMT to this overall pulse height distribution. If one parameterizes the gain of the phototube G as

$$G \propto V^{s\alpha} \tag{3.3}$$

where s is the number of dynodes stages of the PMT (s=12 for the phototubes in the CLAS TOF system), α is the gain constant for the PMT (for the phototubes in the

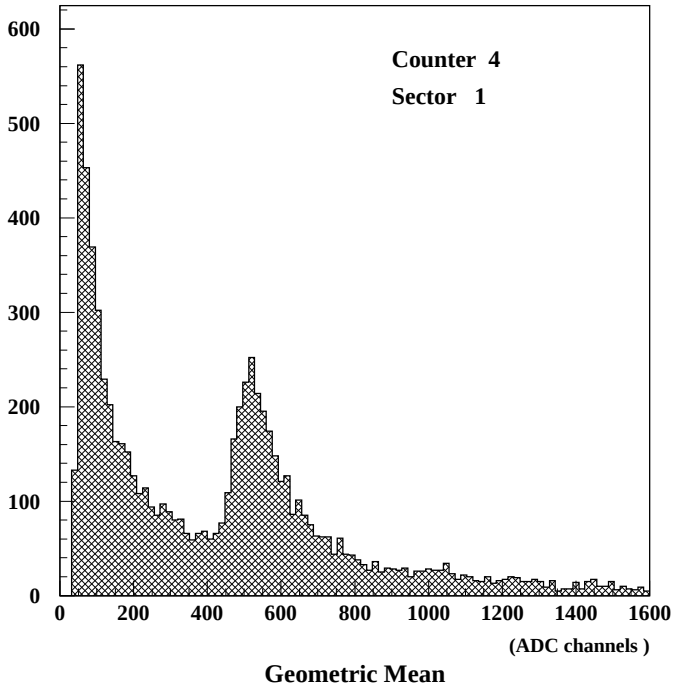

Figure 3.5: Typical pulse-height spectrum of all hits in a TOF counter. The energy is estimated by evaluating the geometric mean of right and left PMTs.

CLAS TOF system $s\alpha \sim 7.2$), and V is the voltage drop between the cathode and anode one can then obtain an expression that governs the gain change if one changes the voltage:

$$\ln G = s\alpha \ln V \rightarrow \frac{dG}{G} = \frac{s\alpha dV}{V} \tag{3.4}$$

The for relatively small changes in voltage this expression becomes

$$\Delta V = V_i \frac{\Delta G'}{G' s\alpha} \tag{3.5}$$

where V_i is the old voltage of the PMT, G' is the pulse height of the PMT proportionate to the gain measured in ADC channels, $\Delta G' = 600 - G'$ is the desired pulse height change and $s\alpha = 7.2$.

The first step in this calibration is taking a cosmic-ray data run. There are two

separate data acquisition configurations used, one for the large-angle counters and one for the forward counters. The trigger for the large-angle configuration requires cosmic tracks traversing sectors offset by 120° instead of a simple opposite-sector trigger. This overcomes the horizontal track requirement for sectors 1 and 4 required by a pure opposite-sector trigger. The nature of incoming cosmic radiation requires a separate configuration for the forward counters. Since incident cosmic rays are predominantly vertical, a software trigger was developed, which utilizes the EC, to construct tracks that approximately point back to the target. Such a situation would require multiple day-long data-taking sessions to accumulate sufficient statistics in these sectors.

Until recently, the gain-matching procedure for each counter was conducted manually. There now exists a software package managed by Concurrent Versions System, **hv_code** which automates this procedure. This software operates on three different file sources as input: fitted gains peaks for each counter (from the software package **gains**), text files containing the voltages of each PMT when the cosmic data was taken and fits of the $\ln \frac{A_L}{A_R}$ distributions (from the software package **log_stuff**) used to separate the left PMTs' contribution to the gain from the right. During the a cosmic ray run, each scintillator is assumed to be uniformly illuminated as shown in Figure 3.6. This uniform illumination of each scintillator produces the distributions such as the $\ln \frac{A_L}{A_R}$ distributions that are later fitted. The fitted parameters from these distributions are the input to the hv_code. The output of hv_code are four files containing the new voltages for the PMTs separated by carriage, north, south, space, and forward, as well as diagnostic histograms. Usually this procedure requires multiple iterations to converge upon suitably-balanced gains for each tube.

3.5 TOF Calibration

To obtain meaningful information from the TOF system, the ADCs, TDCs, discriminators and delay in the cables must all first be calibrated. To accomplish this, a software package managed by Concurrent Versions System (CVS) exists for each aspect of the calibration procedure. More specifically, the calibration procedure includes the determination of the ADC pedestals, PMT gain-matching, determination

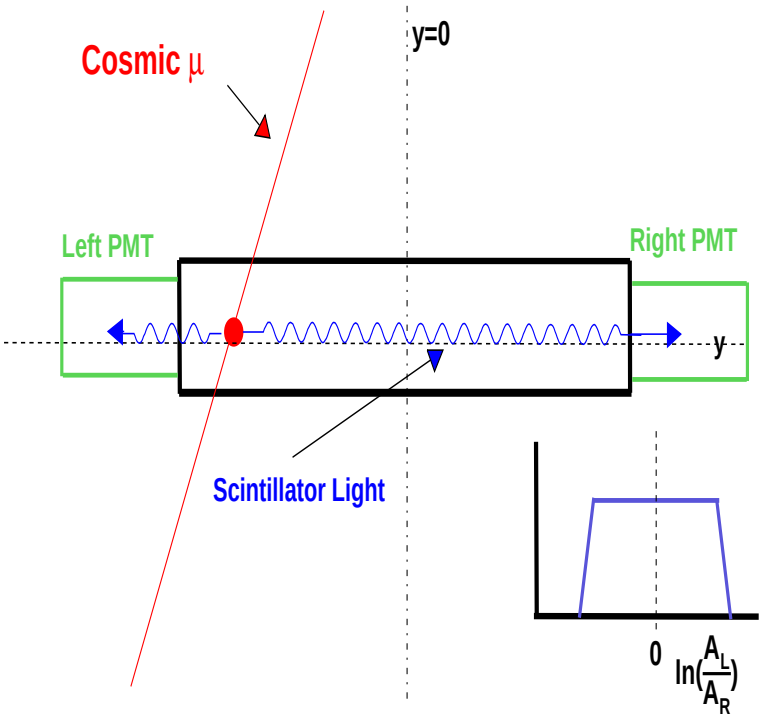

Figure 3.6: Figure shows a cosmic ray incident on a scintillator bar. An accumulation of events uniformly illuminating the scintillator bar produces the distribution shown in the bottom right of the diagram. This distribution is centered around zero if the two phototubes are properly gain-matched.

of the time-walk correction function parameters and assorted time-offset parameter such as paddle to paddle delay caused by differing cable lengths.

The calibration is based on four main sources of data, namely laser data taken with the laser calibration system, pulser data, cosmic-ray data, and beam data taken at 5.75 GeV on a liquid hydrogen target. The sequence and requirements of each calibration step is summarized in Table 3.1 [29].

Calibration step	Main requirements
Status	Raw Beam Data
Pedestals	Pulser data
TDC calibration	Pulser data
Time-walk correction	Laser data
Left-right Adjustment	Raw Beam Data
Energy loss	Cosmic Ray Data, left-right time alignment at SC level
Attenuation length	Cosmic Ray Data, left-right time alignment at SC level
Effective velocity	Reconstructed-Track Data and all constants above
RF parameters	Reconstructed-Track Data and all constants above
Counter-to-counter delays	Reconstructed-Track Data and all constants above
RF offsets	Reconstructed-Track Data and all constants above
Geometric constants	survey data

Table 3.1: The order and requirements for the TOF calibration.

3.5.1 Pedestal Calibration

The ADC pedestal values are obtained using dedicated 100Hz pulser data completed before taking production data. The data is analyzed at the counting house using the PEDMAN utility, a ROOT-based, online software package that enables the user to analyze the pedestal values for each counter in each subsystem, and then set them.

3.5.2 TDC Calibration

The TDC calibration serves to determine the constants in the quadratic equation used to convert raw TDC channels T to time t in nanoseconds.

$$t = c_0 + c_1 T + c_2 T^2 \tag{3.6}$$

Typical values for these constants are $c_0 \sim 1$ns, $c_1 \sim 0.05$ns/channel, and $c_2 \sim 5 \times 10^{-8}$ns/$ch^2$. A pulser run is taken and then analyzed offline with the software package TDC_calib. In order to reduce correlations between adjacent channels, every fourth channel is pulsed sequentially.

3.5.3 Time-Walk Corrections

The Time-Walk is an instrumental shift in the measured time from a leading-edge discriminator due to the finite rise time of the analog pulse. The purpose of the Time-Walk correction is to measure and correct for the dependence of the LeCroy 2313 leading-edge discriminator output pulse time on the input pulse height. Bursts of laser light of differing intensities using a neutral density filter are delivered to the center of each counter via optical fibers. The pulse-time measurement tells us the time a PMT pulse crosses a fixed (leading-edge) voltage threshold. The time-walk corrections are performed in software using an empirically-determined function

$$t_w = t - f_w\left(\frac{A-P}{Th}\right) + f_w\left(\frac{600}{Th}\right) \tag{3.7}$$

where A is the ADC channel, P is the pedestal value, Th is the ADC channel corresponding to the leading-edge discriminator threshold of 20mV, and f_w is the time-walk correction function

$$\begin{aligned} f_w(x) &= \frac{w_2}{x^{w_3}} \qquad \text{if} \qquad x < w_0 \\ f_w(x) &= \frac{w_2}{{w_0}^{w_3}}(1+w_3) - \frac{w_2 w_3}{{w_0}^{w_3+1}}x \qquad \text{if} \qquad x > w_0 \end{aligned} \tag{3.8}$$

The time vs. ADC distribution is fit using equations 3.9 and 3.10 with two adjustable fit parameters w_2 and w_3. These parameters are determined for each counter and are then recorded in the calibration database. Ref[30].

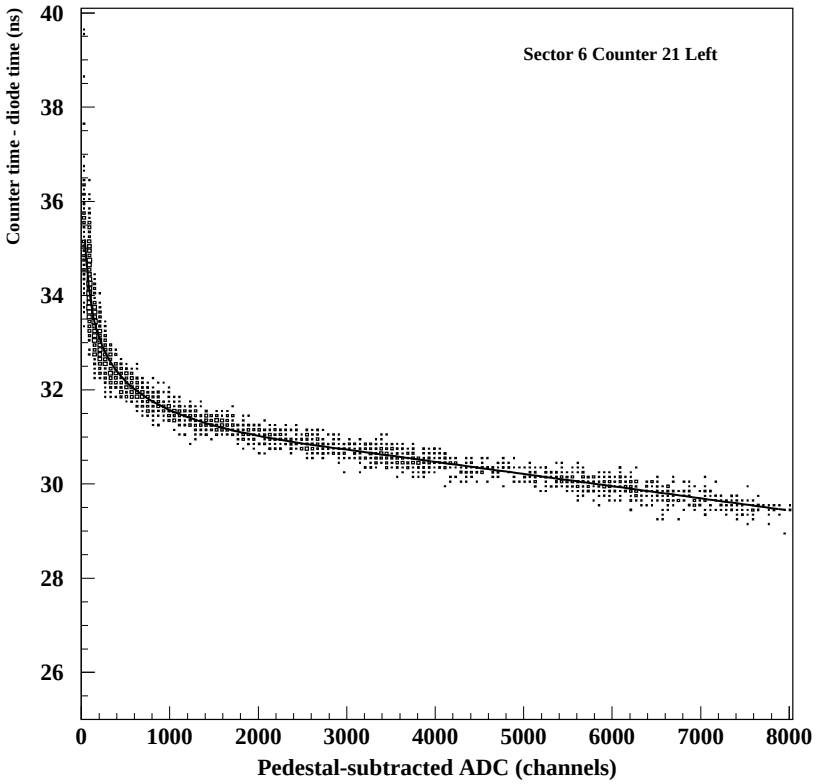

Figure 3.7: Example of the time dependence of a TOF TDC on pulse height. The solid line represents the calibration fit.

3.5.4 Paired Counters

As was mentioned in section 3.1, there are 57 counters per sector giving a grand total of 342 physical counters. In order to simplify the electronics, the last 18 counters in each sector were paired into nine effective counters, giving us a total of 288 logical counters. The pulses from each of the four PMTs are matched in time during the coupled-paddle calibration step and the ADC peaks are matched during the gain-matching calibration step.

3.5.5 Attenuation Length and Effective Velocity

The attenuation of light collection in the scintillator material is accounted for during the attenuation length calibration. Beam data is used to obtain the effective attenuation constants for each paddle which depend upon the dimensions of the scintillator paddle. For each paddle, $\ln \frac{A_L}{A_R}$ vs hit position is plotted. The hit position is the position y along the scintillator (taken to be 0 at the center) where the charged track crosses, as determined by CLAS tracking. The fitted slope of this plot is recorded as the attenuation constant of that paddle.

The effective velocity of light in each scintillator, which is the propagation velocity in the scintillator material, must also be calibrated. This quantity becomes quite important in the situation where there is only one working PMT for a counter. For instance, in this case where only the left PMT is functioning, the time of the hit is given by

$$T = T_L - \frac{y}{V_{eff}} \tag{3.9}$$

where T_L is the time given by the working left TDC, y is the position of the hit, and V_{eff} is the effective velocity of light to the right PMT. Although the left/right effective velocity values can be different, they are usually the same in practice. A quality effective velocity calibration is then essential for obtaining meaningful timing information from such a counter. For each paddle, the SC time vs hit position is plotted. The fitted slope of this plot is the effective velocity of the paddle.

3.5.6 Time-Delay Calibration (Paddle to Paddle Delay)

Events of the topology $ep \rightarrow ep\pi X$ are used to fine-tune the calibration of the relative time delays between the 288 counters. This is accomplished by comparing the TOF time of an event with the beam RF time. The TOF time is given by

$$\mathsf{TOF} \quad \mathsf{time} = \mathsf{TOF} - \frac{d}{\beta c} \tag{3.10}$$

where TOF is the time to reach the TOF counter, d is the distance from the event vertex to TOF counter (length of the track), β is given as

$$\beta = \frac{p}{\sqrt{p^2 + M^2}} \tag{3.11}$$

p is the momentum of the track as measured by the drift chambers and M is the assumed mass of the particle producing the track. The RF period is the time between successive, picosecond electron bunches. The RF signal from the accelerator has a 2.004 ns period which can be resolved by the TOF counter via scattered electrons.

The calibration is divided into four steps. First the difference between the TOF vertex time and the RF time is calculated for pions or electrons. This time is divided by 2.004 and the remainder is taken as the offset correction to the TOF time. There is a 2.004 ns ambiguity introduced by not knowing which beam bunch was associated with the event. To correct for this, electron-pion coincident events were used. The calibration constants are determined modulo 2.004 ns by requiring that the two reconstructed tracks (e^- and π) have a common vertex time. Secondly, due to their abundance in the forward direction, electrons are detected in the first 10 counters of each sector which are calibrated to an arbitrary but fixed counter using coincident pions within each sector. Third, using pion events, the first 10 counters of sector 1 are calibrated to the first 10 counters of the remaining five sectors using electron events. In the fourth and final step, paddles 11-48 for all the sectors are calibrated against the offset of the first 10 paddles in each sector using pion events. A plot of TOF vertex time compared to RF time for all the counters shows the result of the calibration. Ref[29].

3.5.7 Alignment of TOF to RF Signal and RF Correction

Along with the timing information from the TOF counters, a sub multiple of the RF signal time is also recorded. One can then synchronize the event start time to the correct beam bunch and use the RF time as the correct event start time. Since the knowledge of the RF time is much more accurate, this should improve the overall timing resolution by a factor of $\sqrt{2}$ by eliminating any of the uncertainty associated with the electron timing. The paddle-to-paddle delays were already fixed

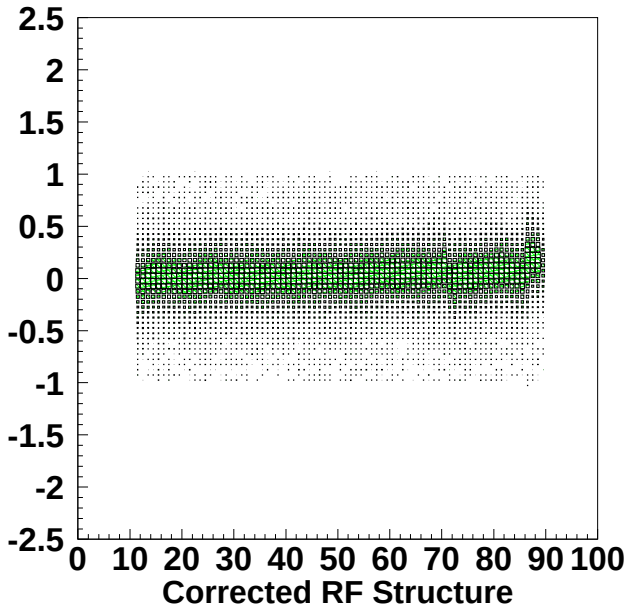

Figure 3.8: Plot of corrected modulus of $(T_0 - T_{RF})$ vs T_{RF} for selected runs of the e1-6 data.

with respect to the RF signal, so the purpose of the RF correction calibration is to fix the RF time to zero relative to the entire TOF system on an event-by-event basis. This adjustment corrects for shifts in the RF signal introduced by changes in the accelerator run conditions as a function of time. The difference between event start time and the RF time RF_{corr} is given by:

$$RF_{corr} = T_{RF} - \overbrace{\left(T_e^{TOF} - \frac{L_e}{\beta_e}\right)}^{\text{Event Start Time}} + \overbrace{\frac{Z_{vert}}{\beta_e}}^{\text{Vertex Correction}} \tag{3.12}$$

where T_{RF} is the time of the RF signal, T_e^{TOF} is the measured electron time in the TOF counters, L_e is the measured length of the electron track, Z_{vert} is the z-coordinate of the event vertex position and β_e is the electron velocity. The vertex correction term is added to compensate for the effect of the target length. The purpose of the RF calibration is to fix the mean value of RF_{corr} to zero and to eliminate any

dependence of RF_{corr} on RF time. Proper calibration of the RF ensures an accurate determination of the TOF resolution which will be described later in this paper. The fitting algorithm uses four independent third-order polynomials that are fit to four regions of the raw RF time. Outside the range of these regions, the correction is set to zero. See Figure 3.8. There is also one overall offset constant, that is applied to all four regions at once, and shifts the RF correction up or down.

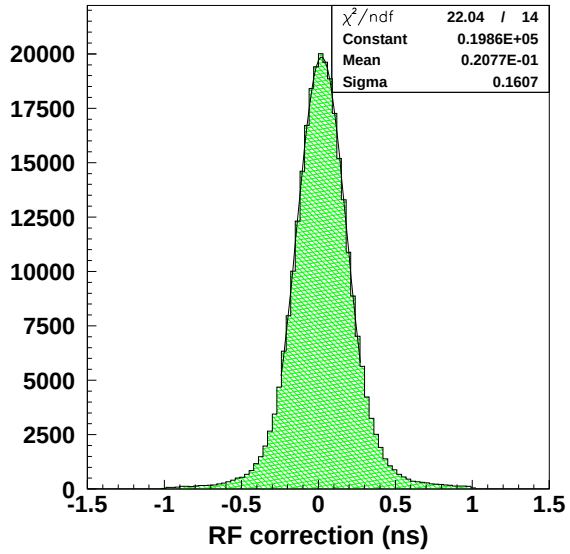

Figure 3.9: Overall timing resolution for electrons achieved for the e1-6 experimental run.

3.5.8 Overall TOF Performance and Summary

The resolution achieved during the calibrations for this run has been the best so far in the detector's history. The resolution of the each paddle is going to depend upon several factors including the length of the scintillator in question. A scintillator 100 cm in length (corresponding to a scattering angle of 18°) has an average resolution of $\sim$ 150 ps. As the scintillator length increases so does the scattering angle[1],

[1]Refer to Figure 3.1 The forward direction is in the direction of the beam and the scintillator bars here are the shortest.

and resolution degrades as expected. There have been significant improvements made in the TOF calibration procedure for the e1-6 run compared to previous runs. An example of this is the newly-automated gain-matching procedure which contributed significantly to the overall quality of the TOF data. The overall resolution for electrons in the e1-6 run is shown in Figure 3.9. A fitted value of 160 ps was attained. A good determination of the quality achieved of the TOF resolution is the measurement of the timing separation of pions and kaons or the separation of kaons and protons.

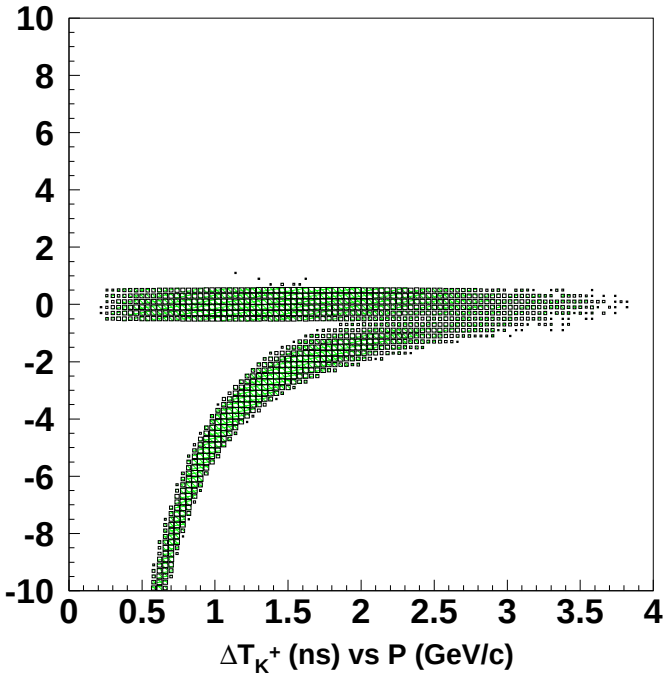

Figure 3.10: A plot of ΔT_{K^+} vs momentum of the kaon and proton sample shows suitable timing separation of kaons and protons up to $\sim$ 1.8 GeV. The data plotted include timing selection cuts on both the kaon and the proton.

The timing separation is characterized by ΔT which is the difference between the measured TOF time and a calculated time if a particle mass is assumed. The particle mass can either be the proton mass if protons are being identified or the kaon mass if K^+'s are being identified. A plot of ΔT vs particle momentum is shown for K^+ identification in Figure 3.10. The straight horizontal band is the kaon band with a ΔT centered around zero. The curved band are protons with a clear time separation

up to a momentum of ~ 1.8 GeV. ΔT is discussed further in section 5.2.

Chapter 4

Calibration and Data Reduction

The data was taken during the e1-6[1] electron beam run period between October 2001 and January 2002. With an electron beam of 5.75 GeV incident on a Hydrogen target, a total of 22.439 mC of total, useful charge was accumulated. The luminosity was maintained at $\sim 10^{34} cm^{-2} \cdot s^{-1}$, which was limited by the background population in the CLAS drift chambers. During the entire span of the experiment, the torus current was set at its full value of 3375 Amperes. The Level 1 trigger for the e1-6 run required a coincidence between the Cerenkov counter and the forward electromagnetic calorimeter. The e1-6 run period was separated into three distinct periods demarcated by machine shutdown and maintenance, during which certain run parameters, such as the RF constants, could and did change.

4.1 Data Reduction

The sample of files ($\sim 2\%$ of the total data) used to complete the Pass0 calibration cooking[2] fairly democratically represented all three data-taking periods. The cooking software used was the production version 3-5 of RECSIS, which was the track-reconstruction software package used. Its output included BOS files, which include the track-reconstructed data banks as well as raw banks, but also monitoring

[1] Denotes an electron run at 6 Gev, designated E-99-105.

[2] "Cooking" refers to the process of reconstructing charged particle tracks in the detector from raw data banks.

histograms. After the calibration stage was completed, the software was tagged, the

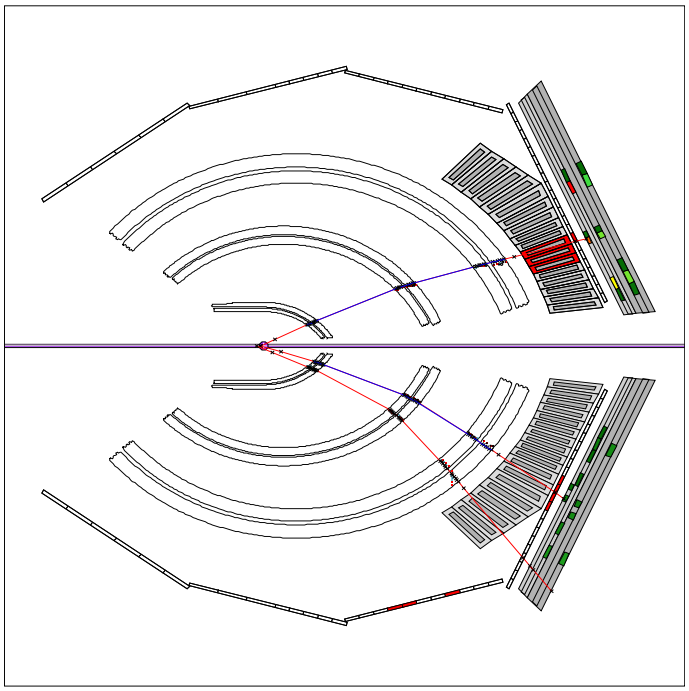

Figure 4.1: An example 3-pronged reconstructed epK^+ event as reconstructed by RECSIS.This particular event shows time-based as well as hit-based tracks reconstructed in a Monte-Carlo event.

calibration constants were copied to the MySQL calibration database[3] to the main run index table of that database and **pass1** cooking was begun.

For the purpose of calibrating the detector, we selected a sample of data to be processed that was uniformly distributed across the entire run. This step was dubbed calibration cooking and the files were used for the calibration of the detector components, as well as to improve the event reconstruction software. The calibration cooking was completed in 3 steps or versions for data in periods 2 and 3 and only in one step for data in period 1. The data in period 1 was cooked last, with calibration constants refined from cooking the other run periods because of the lack of RF information in period 1. The significance of each cooking step is summarized in Table

[3]The calibration database is a centrally-managed database responsible for the management and implementation of the calibration constants of all detector subsystems. It supersedes the old mapfile

Pass 0 Cooking Summary		
Period	**Version**	**Meaning**
Period 1 10/31/01 -11/21/01	V3	Cooking with constants as of 03/19/02 6pm (includes DC alignment and best paddle2paddle constants from run 30921)
Period 2 11/28/01 -12/21/01	V1	Cooking with constants as of 02/07/02
	V2	Cooking with Yoffset calibration, new time-walk constants and RF offset position adjustment
	V3	Cooking with DC alignment constants and new paddle2paddle constants
Period 3 01/05/02 -01/30/02	V1	Cooking with constants as of 02/07/02
	V2	Cooking with Yoffset calibration, new time-walk constants and RF offset position adjustment
	V3	Cooking with DC alignment constants and new paddle2paddle constants

Table 4.1: Calibration cooking steps performed on the three separate run ranges and the meaning of each version.

4.1.

4.2 Detector Calibration Procedure

In order for the data collected to be analyzable, the detector components must be calibrated. The three major calibration procedures are mentioned below.

scheme.

4.2.1 Drift Chamber Calibration

Before the drift chamber calibration procedure can be described, some background information related to the track reconstruction in CLAS must be presented.

Track Reconstruction Overview

Charged particle track reconstruction is completed in four steps. The first three steps are required before proceeding with hit-based (HBT) track fitting, followed by time-based (TBT) track fitting.

1. cluster finding: The first step is to find a contiguous group of hits (called a cluster) in each of the superlayers. Each cluster may contain several track segments.

2. track segment finding: A lookup table is used to find groups of hits or segments within one cluster that are consistent with a track traversing a superlayer.

3. segment linking: Segments from individual superlayers are identified with segments in other superlayers, again using a look-up table. If the look-up table address corresponds to a possible track, it also contains an estimate of the track's initial parameters.

4. track fitting: Using the linked segments, a preliminary angle and momentum are assigned and a trial track is propagated through the CLAS magnetic field. At each layer we calculate the distance-of-closest-approach (DOCA) of the track to the hit wire (HBT), or to the position derived from the drift times (TBT). As described below, track parameters are then adjusted to provide the best fit of the track to the measured positions.

The fitting procedure minimizes the following quantity

$$\chi^2 \;=\; \sum_i \frac{[d_{meas,i} - d_i(\vec{q})]^2}{\sigma_i^2}\,, \tag{4.1}$$

where $d_i(\vec{q})$ is a reference trajectory whose parameter vector $\vec{q}$ is composed of inverse momentum, the polar and azimuthal angles (w.r.t. the beam), and the interaction

vertex transverse to and parallel to the beam direction. The uncertainty for HBT is given by $\sigma_i \sim$ cell size $2\sqrt{12}$, and for TBT by a distance-dependent resolution which varies between 200 and 800 μ.

Alignment

Each of the 18 drift chambers was surveyed upon installation. This served as reasonable starting point for the drift chamber alignment and positions, to be refined using straight-track (no magnetic field) data.

Time-Delay Calibration

The fixed time delays for each wire must be determined before the drift times can be known. These delays are mainly a result of different cable lengths, and are determined using a pulser that generates two pulses with constant time separation. One pulse goes to the Amplifier/Discriminator (DAB) crates while the other goes acts as a common stop for the TDCs. This provides a relative t_0 for each signal wire.

Time-to-distance Calibration

In order to have confidence in the track fitting procedure, the measured drift time from the sense wire and the distance-of-closest-approach (DOCA) to the sense wire must be calibrated. DOCA is a reconstructed quantity, obtained from a fit to a time-based track. These two quantities are used to determine the drift-velocity function of the drift cells. The measured drift time, along with other parameters is used to calculate the predicted distance from the sense wire DIST. The difference of the absolute values of these quantities is called the time residual:

$$Res = |DOCA| - |DIST| \tag{4.2}$$

The residual is used to measure the resolution of the drift chambers.

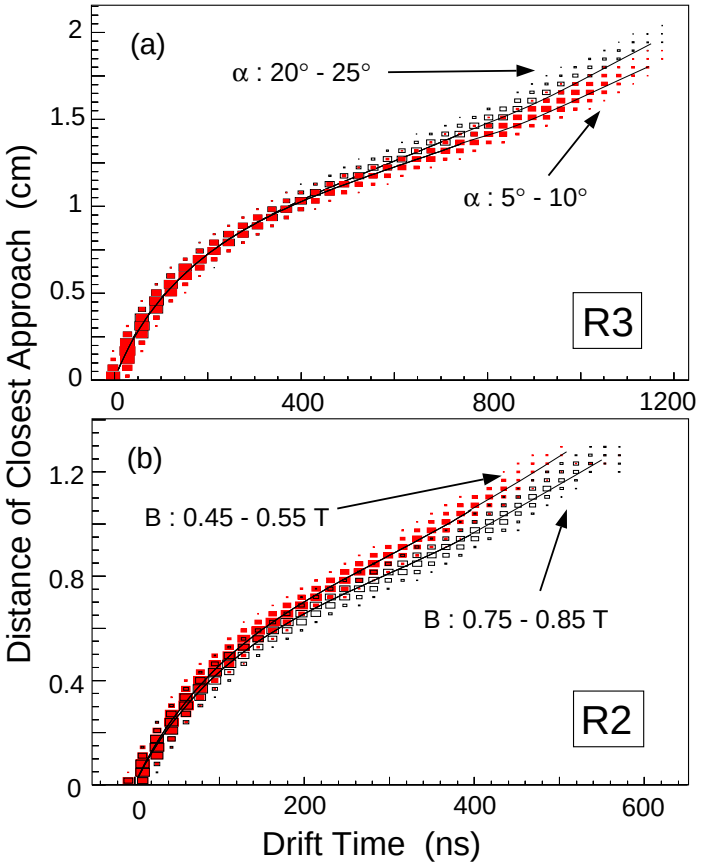

Figure 4.2: Scatter plot of DOCA versus the corrected drift time for a) R3 axial wires and b) R2 axial wires along with a sample fit of the time-to-distance correlation

Function Parameterization

The ultimate purpose of the drift chamber calibrations is to obtain the drift-velocity function mentioned above for each superlayer in every sector. The drift-velocity function relates the quantity DIST of a particle track to the drift time, which is the time it takes for the electrons, created by the ionization of the gas in the drift chamber, to arrive at the sense wire. The determination of this function depends on the drift chamber operating conditions and geometry. As an added complication, the hexagonal shape of the drift cells adds entrance angle dependence to this function.

The parameterized drift time to drift distance function has the form:

$$x(t) = v_0 t + \eta \left(\frac{t}{t_{max}}\right)^p + \kappa \left(\frac{t}{t_{max}}\right)^q, \tag{4.3}$$

where v_0 is the the saturated drift velocity at or near $t = 0$, and the coefficients η and κ, and the exponents p and q are obtained from a fit to the time-to-distance correlation in Figure 4.2. Ions emanating from tracks close to the edge of a cell follow the electric-field line from the field wire to the sense wire, regardless of the entrance angle α. The drift time of these ions is denoted by t_{max}, and is used to define a normalized drift time $\hat{t} = t/t_{max}$. This quantity is used in the time-to-distance function which defines the cell boundary constraint:

$$x(\hat{t} = 1, \alpha) = C \cdot \cos(30^\circ - \alpha). \tag{4.4}$$

where C characterizes the linear cell size. The time-to-distance function can be written in terms of a correction function $f(\hat{t})$:

$$x(\hat{t}, \alpha) = x_0(\hat{t}, \alpha_0) + C\left(\cos\left(30^\circ - \alpha\right) - \cos\left(30^\circ - \alpha_0\right)\right) f(\hat{t}). \tag{4.5}$$

where x_0 is expected drift distance for a normalized drift time with an assumed entrance angle α_0. The function $f(\hat{t})$ is used to correct the extracted drift distance corresponding to the actual entrance angle of the track. The R2 drift chambers are located between the torus cryostats, a region of high and inhomogeneous magnetic field, which affects the drift velocity. These effects are modeled by a modification to α and also by an increase in t_{max}. Further discussion of these effects can be found in reference [31].

4.2.2 EC Energy Calibration

In order to obtain meaningful energy information from the electromagnetic calorimeter, the gains of the phototubes must be calibrated. This is done in a similar fashion to the gain matching procedure for the TOF (section 3.4). In fact, the same cosmic ray data is used for the EC energy calibration as is used for the TOF forward carriage

counters. Due to the large number of triggers required, raw data files are not stored during cosmic runs. Instead events are filtered in real time with a ET client called level3 to select muon tracks which activate a single pixel in the EC. A pixel is defined as an intersection between scintillators in the U, V, and W planes [32]. The pixel ID is calculated and six sets of pixel histograms (one for each U,V,W and inner/outer view) are weighted with the measured ADC for the PMT in that view. These pixel histograms are later analyzed with a PAW kumac to estimate the PMT gains and scintillator attenuation lengths [33]. The high voltage of the PMTs are adjusted to equalize the gains of all the channels.

4.2.3 Electromagnetic Calorimeter Timing Calibration

The CLAS Electromagnetic Calorimeter is an essential component of the CLAS detector. It serves as the primary electron trigger for CLAS and thus the successful calibration of the Electromagnetic Calorimeter is essential in obtaining quality data. The Electromagnetic Calorimeter serves three main functions:

• Detection and triggering of electrons at energies above 0.5 GeV. The total energy deposited in the EC is available at the trigger level to reject minimum ionizing particles or to select a particular range of scattered electron energy. This is directly related to the EC energy calibration.

• Detection of photons at energies above 0.2 GeV, allowing π^o and η reconstruction from the measurement of their 2γ decays.

• Detection of neutrons, with discrimination between photons and neutrons using time-of-flight measurements.

The EC timing calibration is crucial to the DECS analysis within this data set but are not directly relevant to this analysis.

4.2.4 Time of Flight Calibration

The calibration of the TOF system is discussed in detail in chapter 3, section 3 of this paper.

4.2.5 Cerenkov Counter Calibration

The Cerenkov counters perform the dual function of triggering on electrons as well as providing electron-pion separation. The single-photoelectron response of the photomultiplier tubes is used to perform the gain-matching calibration of the detector as well as to calibrate the response of the detector in terms of the number of photoelectrons. A value of 4-5 photoelectrons per in-bending electron track is typical.

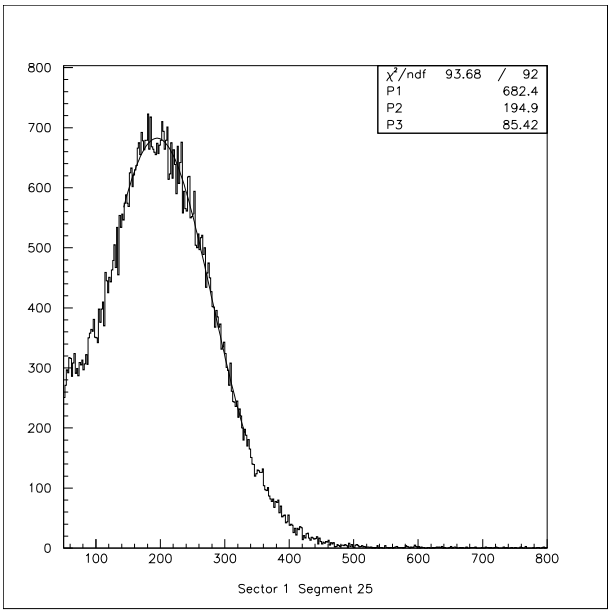

Figure 4.3: Fitted ADC values for one Cerenkov channel. This is an example of a pmt with very little noise.

TDC and Pedestal Calibrations

Ultimately, the pedestals, TDCs, and single photoelectron position must be calibrated. To accomplish this, pulser runs are used to calibrate the CC TDCs after a pedestal calibration has been completed. More specifically the constant T1, which is used to convert raw TDC channels to nanoseconds. Secondly, in order to obtain meaningful ADC information, the pedestal values for each channel must be determined.

This is accomplished as part of an online calibration procedure that determines the pedestal values for each detector subsystem. The Single Photoelectron (SPE) amplitude calibration is unique to the Cerenkov counter, whose purpose is to determine the position of the SPE and the noise function for each PMT. The calibration is accomplished using cosmic ray data. Once sufficient data has been accumulated, the ADC distribution for every PMT is fit with a Gaussian function. This determines the SPE position. An example of this fit is shown in Figure 4.3.

4.3 Further Data Reduction

During the e1-6 run period, over 5 billion triggers were recorded. For a trigger to qualify as an event, there must be at least one hit-based, negative, reconstructed track in the drift chambers. More precise tracking is achieved by also requiring time-based tracking to be present. The fraction of triggers containing at least one negative hit-based track is $\sim 33\%$. For this sample of events, full event reconstruction, monitoring, and filtering were performed.

In order to reduce the multi-terabyte data set to a manageable size for analysis, the data set was filtered with an epK^+ (electron-proton-kaon) skim program. This skim uses multiple levels of cuts to "skim" events from the full data set containing exactly one electron, one proton, and one K^+ candidate plus possible additional negative tracks. The skim program identifies and selects electrons using the PID definition with additional cuts on the EC energy and particle momentum as measured by the drift chambers. The EC cut is a polynomial cut of $\frac{E_e}{P_e}$ vs P_e in the variable $\frac{E_e}{P_e}$. This ratio is parameterized as

$$f(P_e) = A + BP_e - C{P_e}^2 + D{P_e}^3 \tag{4.6}$$

and

$$\sigma_{\frac{E_e}{P_e}} = a - bP_e + c{P_e}^2 - d{P_e}^3 \tag{4.7}$$

The cut is defined as $f(P_e) - 3\sigma_{\frac{E_e}{P_e}} \leq \frac{E_e}{P_e} \leq f(P_e) + 3\sigma_{\frac{E_e}{P_e}}$. These cuts are summarized in Table 4.3. In order to recoup high-momentum proton and kaon candidate events that would be lost by cutting on the TOF mass, cuts on the particle time-of-flight

Table 4.2: Parameter Values for $\frac{E_p}{P_e}$ vs P_e cut

A	B	C	D
0.26662	0.20317e-01	0.26262e-02	0.18451e-04
a	b	c	d
0.42904e-01	0.21558e-01	0.73153e-02	0.91419e-03

are employed to make proton and kaon selection. To identify and select a Kaon or Proton candidate, a positive particle is selected and its TOF time T_{TOF} is recorded. A second time $T_{calculated}$ is then computed from measured momentum of the particle, which is the time-of-flight of the particle if it is assumed to have the K^+ or proton mass. The difference $T_{TOF} - T_{calculated}$ is computed and the all events within ± 1.05 ns are kept. This timing cut is discussed in further detail in the section 5.2 Hadron Cuts and ID. The filtering process isolated about 5.6 million such events ($\sim$ 31 GB) for further analysis. The filtering process greatly reduces the size of analyzable data, considering the size of the original data set was over 2 Terabytes.

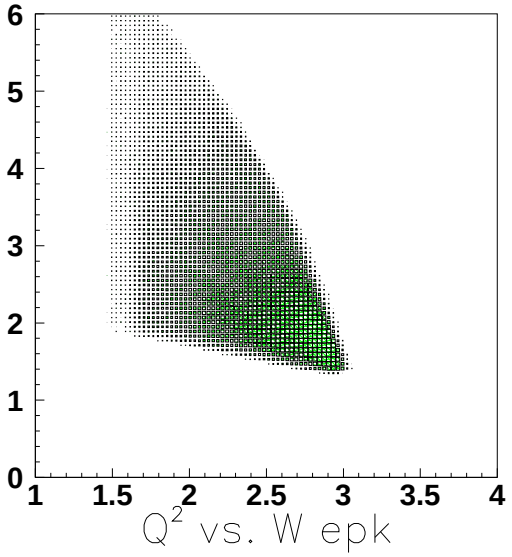

Figure 4.4: Kinematic distribution of epK+ event sample

Table 4.3: Summary of Cuts in epK^+ Skim

Cut	**Purpose**	**Value**
Electron PID	Identify good Electrons	-
EC Energy	Eliminate false triggers	$E = 0.64GeV$
E/p vs p	Avoid e^-/π^- misidentification	$3\sigma_{\frac{E}{P}}$
Proton Timing	Loose cut to identify Protons	$\pm$1.05 ns
K^+ Timing	Loose cut to identify K^+'s	$\pm$1.05 ns

4.4 The epK^+K^- Final State

The desire to further reduce the data size prompted the completion of one more filtering step. The average time taken to cycle through all the epK^+ skim files ($\approx$ 20 minutes) greatly increased the turn-around time whenever new plots had to be produced. Therefore the data was filtered once through the C++ analysis code phi++ with a set of relaxed cuts summarized in Table 4.4. The cuts included here are many of the same cuts used in the final analysis but with slightly relaxed values in the case of the proton and K^+ timing cuts. The magnetic field configuration for the e1-6 run was such that all negative tracks were "in-bending" relative to the beam. These conditions equate to a very small acceptance for the K^-. Thus the K^- was reconstructed via the epK^+(X) missing mass. [4]

[4]see Nphe definition on page 60

Cut	**Purpose**	**Value**
Electron Fiducial Cuts	Use trustworthy detector volume to identify electrons	-
Vertex Cut	Eliminate contributions from the target windows	$-8.0\text{cm} \leq z \leq -0.8\text{cm}$
Number of Photoelectrons Cut	Further reduce e^-/π^- misidentification	Nphe ≤ 2.5
Hadron Fiducial Cuts	Use trustworthy detector volume to identify hadrons	-
Proton Timing Cuts	-	± 0.90 ns
K^+ Timing Cuts	-	± 0.90 ns
3 or 4 Tracks per Event	Eliminate additional pion background	-

Table 4.4: Summary of additional cuts in final Phi++ skim.

Chapter 5

Reconstruction and Analysis

The ϕ decays into a K^+ and a K^- with a branching ratio of 49.1%. To select events of the topology $ep \rightarrow epK^+(K^-)$, the K^+ is detected in CLAS, along with the scattered electron and scattered proton, while the K^- is reconstructed using the missing mass technique. The following describes the further reduction and subsequent analysis of the e1-6 data set. The procedure employed for electron and hadron ID, along with all relevant cuts are discussed. The acceptance-corrected total yield and cross sections as a function of Q^2, W, t, Φ and helicity angular distribution in $cos\theta_H$ are discussed, evaluated and presented. The successful extraction of $R = \sigma_L/\sigma_T$ will allow the separation of the longitudinal cross section σ_L from the total cross section, which will enable direct comparison with GPD model predictions.

5.1 Scattered Electron Identification

The cuts used during the analysis ensure only the purest events survive to be included in the final event sample. The following sequence shows the procedure used to identify good epK^+K^- events. An initial round of particle id is completed during cooking but these selections can be and will be improved upon.

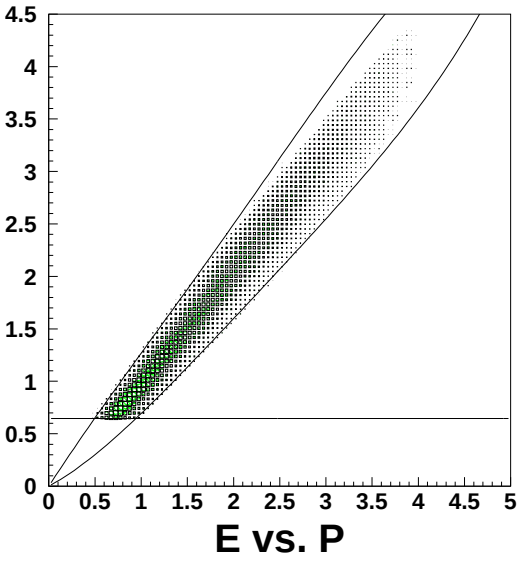

Figure 5.1: $3\sigma_{\frac{E}{P}}$ cuts on E vs. P. Horizontal line is the straight cut on the EC energy at 0.64 GeV. The curved lines are the $3\sigma_{\frac{E}{P}}$ E/p vs. P cuts.

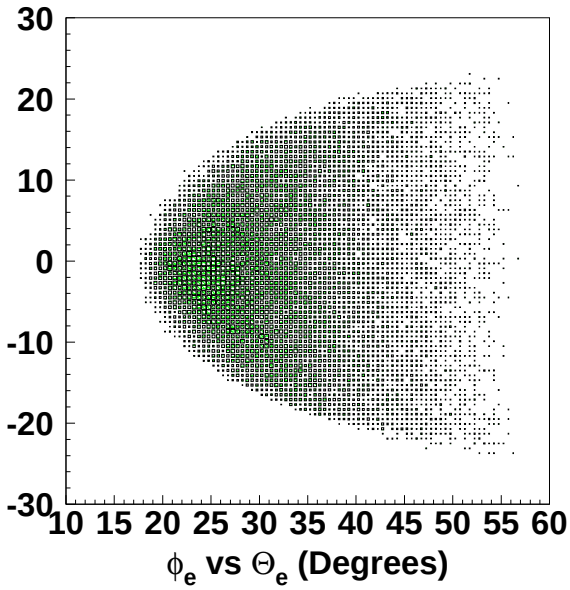

Figure 5.2: Electron sample after fiducial cuts imposed. Figure shows sector 1.

5.1.1 Good Track Selection

Part ID=3

Good electron selection is the essential first step in the reconstruction of the epK^+K^- final state [34]. The first requirement is that the track have a PID number 3 in the PART bank. This requirement encompasses all the general attributes of an electron such as the track being negative as well as loose cuts on the energy deposited in the Electromagnetic Calorimeter.

Vertex Corrections and Z vertex cut

In addition, a cut on the vertex position of the electron track was made to confine the event sample to those emanating from within the target. Electrons that come from the target window, located 2cm downstream from the target are eliminated by a cut on the z component of the vertex position. The cut made is -8.0 cm $\leq Z_{vtx} \leq$ -0.8

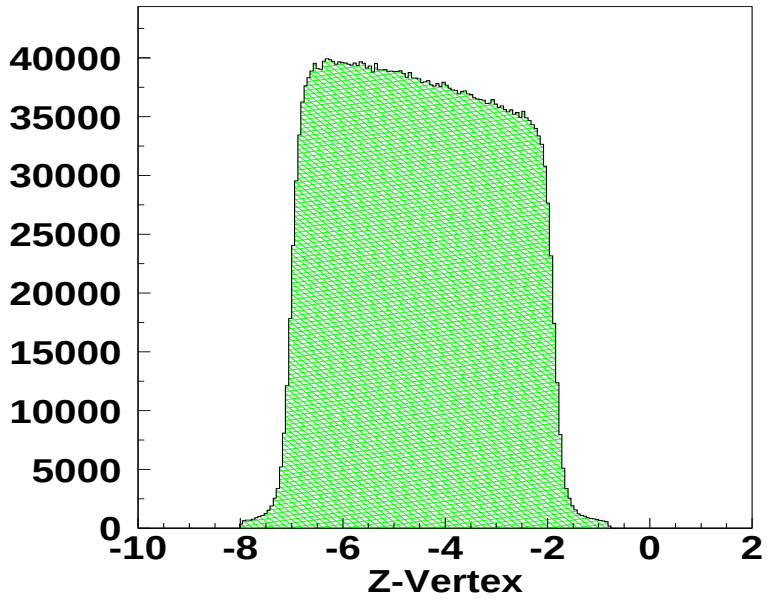

Figure 5.3: Vertex position of electron tracks in cm. The mean shows the z-position of the target. The slant of the distribution is due to acceptance effects in the scattered electron angle.

cm. The distribution of electron vertex positions after this cut was made is shown in Figure 5.3.

5.1.2 Cuts to eliminate detector inefficiencies

Cherenkov fiducial cut

In order to ensure that the events chosen came from a trustworthy volume of the detector, fiducial volume cuts were imposed. The efficiency of the Cherenkov counters are compromised as the light path approaches the edge of the mirrors. This is equivalent to saying the Cherenkov efficiency decreases as the particle (electron) track approaches the geometrical edge of each sector. Cuts are applied to eliminate these inefficient volumes that are a function of electron momentum p_e, polar angle of the scattered electron θ_e, and the azimuthal angle of the scattered electron ϕ_e. A

standard CLAS parametrization of the cuts are

$$\theta \geq \theta_{cut}, \theta_{cut} = C_1 + \frac{C_2}{(p + p_{shift})}$$
$$|\phi_s| \leq C_4 \sin(\theta - \theta_{cut})^{C_3 p^{\alpha}} \tag{5.1}$$

Where $|\phi_s|$ is the azimuthal angle defined relative to the center of each sector and the parameters $C_1 - C_4$, p_{shift}, and α are parameters that were determined for the e1-6 run in reference [35, 36]. The effect of these cuts are shown in Figure 5.2.

Electromagnetic calorimeter fiducial cut

When an electron enters the EC too close to the edge, the resulting particle shower is not completely contained by the detector volume, which means that the measured deposited energy is no longer related to the particle energy. This distance is typically $\sim$ 10 cm from the edge. Therefore a cut is applied in the local coordinate system of the EC (U_{EC},V_{EC}, and W_{EC}), which are calculated from the global coordinate X_{EC} and Y_{EC}. The cuts applied are the same used for the e1-6 ω analysis [10]; $U_{EC} \geq 40$, $V_{EC} \leq 360$, $W_{EC} \leq 390$.

EC/DC Energy/Momentum cut

A cut on the electron energy, as determined by the EC can be estimated from the trigger threshold value $EC_{threshold} = 175$ mV for e1-6. The cut value is calculated via:

$$E_{EC}(MeV) = 214 + 2.47 \times EC_{threshold}(mV) \tag{5.2}$$

This was determined by an in-depth study documented in reference [37]. Due to fluctuations in the trigger signal, a cut, $E_{EC} \geq 700$ MeV was applied.

5.1.3 Cuts to eliminate π^- background

At the cooking stage, there are a number of π^-'s that are misidentified as electrons.

E/p vs. p cut

To avoid e^-/π^- misidentification, the expected ratio of the electron energy as determined by the EC to its momentum as determined by the DC was exploited in the form of cuts on E/P vs P, and were imposed at the epK^+ skim level. Due to the sampling ratio of the EC, the expected value of E/p for electrons is ~ 0.29. The details of this cut are discussed in section 4.3 and are shown in Figure 5.1.

E_{in} Cut

Minimum-ionizing pions are expected to deposit ~ 25 MeV of energy in the inner part of the calorimeter as well as ~ 40 MeV in the outer part of the calorimeter. If one applies a cut on the energy deposited in the inner calorimeter $E_{in} \geq 60$ MeV, this eliminates most of this pion background. [10]

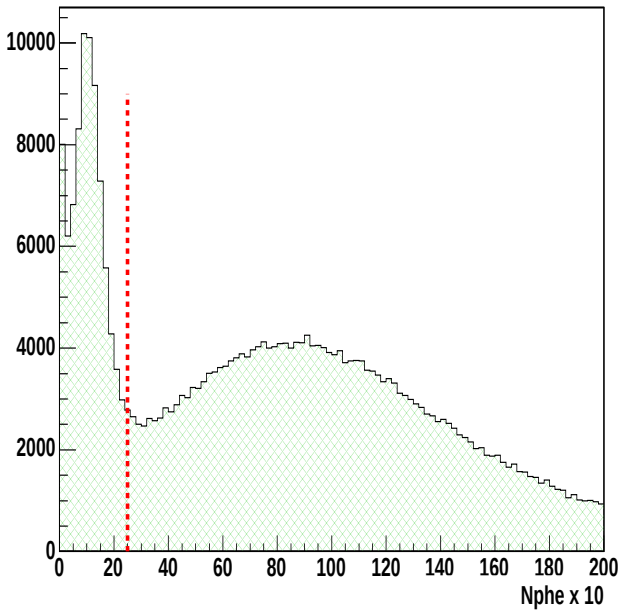

Figure 5.4: Figure shows number of photoelectrons distributions. The pion peak is clearly seen at zero. The red dashed line shows the cut to eliminate this pion contamination.

Number of photoelectrons cut

Upon inspection of the number of photoelectrons distribution (Nphe) in the Cherenkov counter, one observes the electron signal, distributed according to the Poisson distribution, centered at around Nphe = 9 or 10. In addition to this, there exists a very distinct peak centered at Nphe $\sim$ 1 which is due to pion contamination.

Table 5.1: Summary of Cuts used for electron selection. The percentages shown indicate the effect of each cut on the "epK skimmed" data sample. Each cut was applied one at a time to the data so the effectiveness of each cut could be considered separately.

Electron Id Cut	**Accepted (%)**
PART ID = 3	100
Z-Vertex	96
EC Energy/DC momentum	89
CC Fiducial Cuts	77
EC Fiducial Cuts	70
E_{in}	98
E_{TOT}/p	99
Nphe	64

5.2 Hadron Cuts and ID

To complete the construction of the epK^+K^- final state, a clean sample of protons and K^+ must be successfully identified. The beam energy for this data sample was 5.754 GeV, which was significantly higher than previous runs. Due to this, cuts on the TOF mass would lead to inefficiencies at high momenta. This is due to the spreading or smearing of the measured TOF mass as $\beta \rightarrow 1$. To counteract this effect, we employed cuts on particle times, which are closely related to the experimental resolution. These cuts were described in section 4.3. The time as measured by the TOF is denoted by $T_{measured}$. The quantity T_{calc} is the calculated flight time of the

respective track with a specific mass assignment. First, assuming either the M_p for case of proton selection or M_{K^+} for the case of K^+ selection, the quantity β_{calc} is computed:

$$\beta_{calc} = \frac{p^2}{\sqrt{p^2 + M^2_{P/K^+}}}, \tag{5.3}$$

where p is the particle momentum as measured by the drift chambers. T_{calc} is then given by:

$$T_{calc} = \frac{d_{trk}}{\beta_{calc} \cdot c}, \tag{5.4}$$

where d_{trk} is the measured track length from the target to the detection plane. The quantity ΔT is then given by $\Delta T = T_{measured} - T_{calc}$.

$$\Delta T(p/K^+) = T_{measured}(p/K^+) - T_{calc}(p/K^+) \tag{5.5}$$

This is the quantity used to make proton and K^+ selections.

5.2.1 Proton ID

The proton was selected using a timing cut, $\Delta T(p) < 0.75$ns. The proton selection included tracks which satisfied **only** the proton cuts as well as high momentum particles which satisfied both the proton and K^+ timing cuts but were identified as protons because a kaon was unambiguously associated with the other positive track. In addition, fiducial volume cuts were also applied to final proton sample in order to cut out tracks in inefficient and unreliable parts of the detector. The fiducial cuts take the following functional form $f(\theta)_{upper} = A(1.0 - e^{-B(\theta - C)})$ for the upper cut and $f(\theta)_{lower} = a(1.0 - e^{-b(\theta - c)})$ for the lower cut. A(a), B(b), and C(c) are sector dependent fit parameters adjusted to give a liberal cut in the kaon lab angles θ and ϕ.

5.2.2 K^+ ID

The K^+ was selected using a timing cut, $\Delta T(K^+) < 0.60$ns. The Kaon selection included tracks which satisfied **only** the Kaon cuts as well as high momentum particles

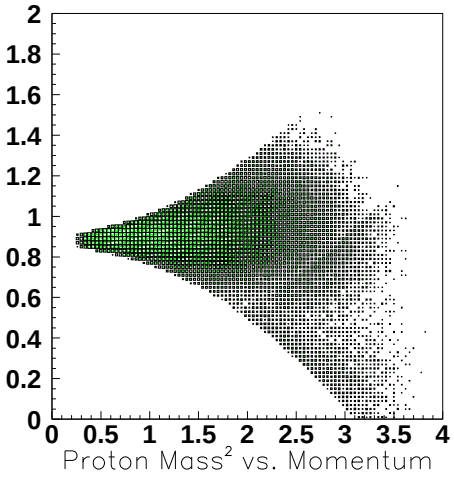

Figure 5.5: Plot of TOF Mass^2 vs momentum for identified protons. The 5σ cuts are clearly visible.

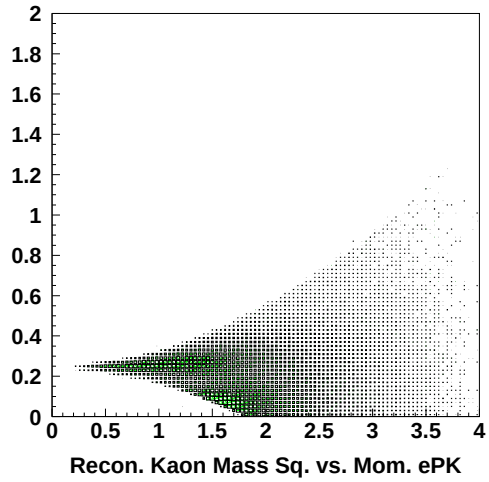

Figure 5.6: Plot of TOF Mass^2 vs momentum for identified K^+s. The 4σ cuts are clearly visible. Also clearly visible is the π^+ contamination at higher momenta.

which satisfied both the proton and K^+ timing cuts but were identified as Kaons because a proton was unambiguously associated with the other positive track. In addition, fiducial volume cuts were also applied to final K^+ sample in order to cut out tracks in inefficient and unreliable parts of the detector. These are shown in Figures 5.7 and 5.8. The same functional form of the fiducial cuts are used for the K^+ as was used for the proton, however the parameters differed slightly.

5.2.3 K^- ID

Due to the e1-6 magnetic field configuration, all negative particles were in-bending. This amounts to a very small acceptance of K^-'s, therefore K^- identification was accomplished via the missing mass technique. The epK^+ missing mass is shown in Figure 5.9. A 2σ cut was applied to the epK^+X sample to select K^-s. The epK^+ missing mass vs K^+K^- invariant mass is shown in Figure 5.10 along with the 2σ cuts on the epK^+ missing mass. The invariant mass is defined as

$$IM_{K^+K^-} = \sqrt{(K^+ + K^-) \cdot (K^+ + K^-)} \tag{5.6}$$

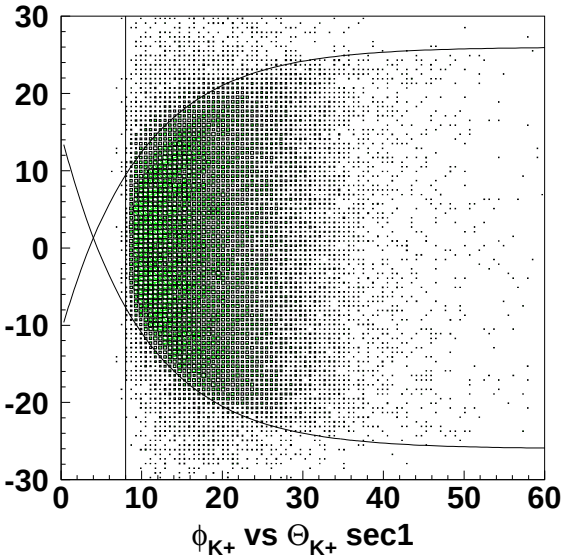

Figure 5.7: Scatter plot of ϕ vs. θ for the K^+ sample before fiducial volume cut is applied.

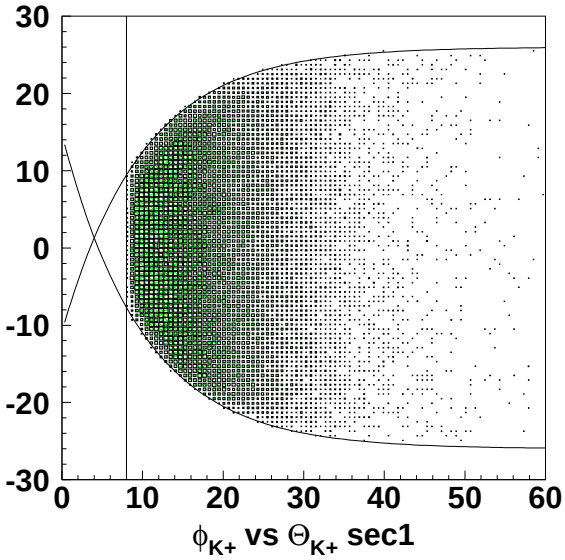

Figure 5.8: Scatter plot of ϕ vs. θ for the K^+ sample after fiducial volume cut is applied.

where K^+ and K^- are the kaon 4-vectors with the rest mass replaced with the particle data group value and the K^- momentum is the measured missing momentum.

5.2.4 Other Cuts to Eliminate Background

Additional cuts can be useful in order to obtain the cleanest sample of events in the epK^+K^- final state. If one plots the epK^+ missing mass versus the same variable redefined with the K^+ mass replaced by the pion mass, one can separate the real K^- sample from the misidentified pion background. This pion background is mainly the decay product of ρ, ω and the ground-state hyperons Λ and $\Sigma^{+/-}$. This background would eventually have been removed during the K^- selection process, however by applying the cut shown in Figure 5.11, one obtains a much cleaner K^+ sample at the K^+ id stage. The effectiveness of this cut in eliminating the Λ and $\Sigma^{+/-}$ background is illustrated in Figure 5.12.

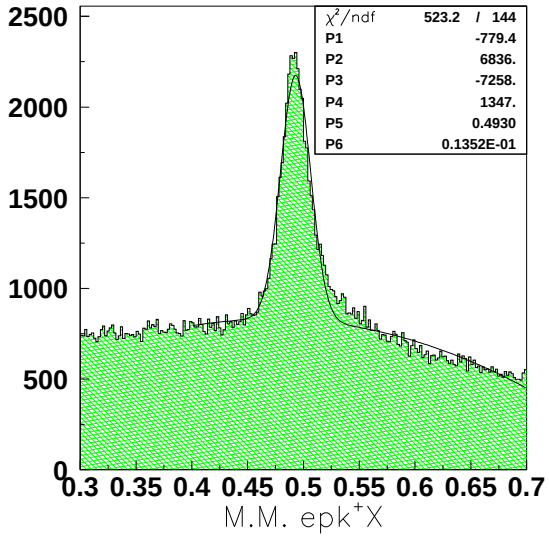

Figure 5.9: Plot of epK^+X missing mass. Shown is the Gaussian+2^{nd}-order polynomial fit to the K^- peak.

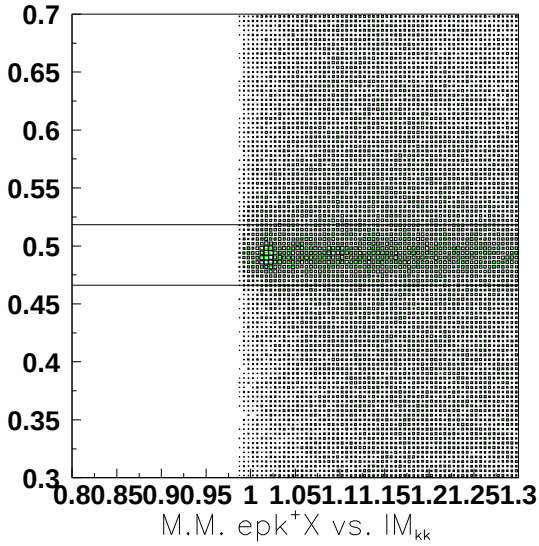

Figure 5.10: Plot of epK^+X missing mass vs. the K^+K^- invariant mass. $\pm 2\sigma$ cuts are applied to the epK^+X missing mass in order to select K^-s.

5.2.5 Electron Momentum Corrections

Our knowledge of the CLAS geometry and magnetic field distribution is incomplete. This causes errors in the track momentum and position reconstruction, which affect the determination of physics quantities such as energy (invariant mass of the ϕ) and missing mass. To correct for these effects, empirically-determined momentum and angle corrections were imposed on the electron. The electron angle is corrected first, which accounts for uncertainties in the torus field and angles defined by the DC geometry. These corrected angles were then used to determine the corrected momentum.

$$P_{ecorr} = P_{emeasured} \times g(\theta_e, \phi_e, sector) \tag{5.7}$$

The correction function $g(\theta_e, \phi_e, sector)$ is treated as a sector-dependent scale factor which is also a function of the polar angle of the scattered electron θ_e and the scattered

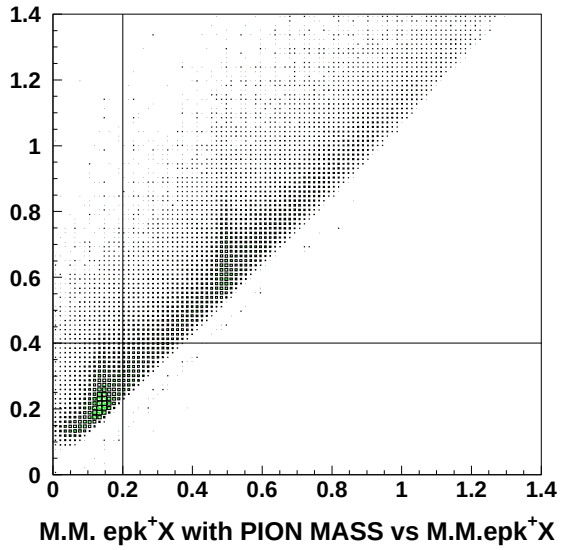

Figure 5.11: Scatter plot of epK^+ missing mass with modified K^+ mass versus the regular epK^+ missing mass. The cuts on these two variables are shown.

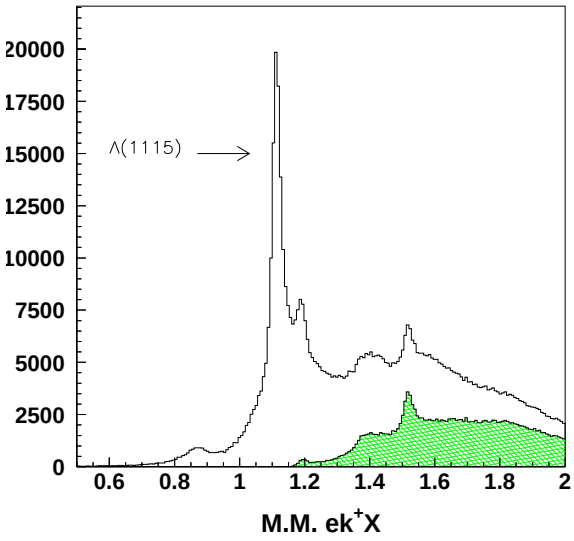

Figure 5.12: eK^+ missing mass before cut (unfilled) and after cut (green-hatched) illustrated in Figure 5.11. The ground-state $\Lambda(1115)$ is shown as well as the $\Sigma(1189)$ directly right of the Λ.

electron azimuthal angle ϕ_e.

$$g(\theta_e, \phi_e, sector) = \delta p_e = p_{ecorr}/p_{emeasured} \tag{5.8}$$

5.2.6 Hadron Energy-Loss Corrections

In order to correct for the energy loss suffered by the proton in the target and to a lesser extent, in the drift chamber regions of CLAS, an empirical proton energy correction is applied to the proton sample. The correction function is defined as a function of the detected proton momentum $p_{reconstructed}$ and scattering angle θ_p.

$$p_{corr} = p_{reconstructed} \times F(p_{reconstructed}, \theta_p) \tag{5.9}$$

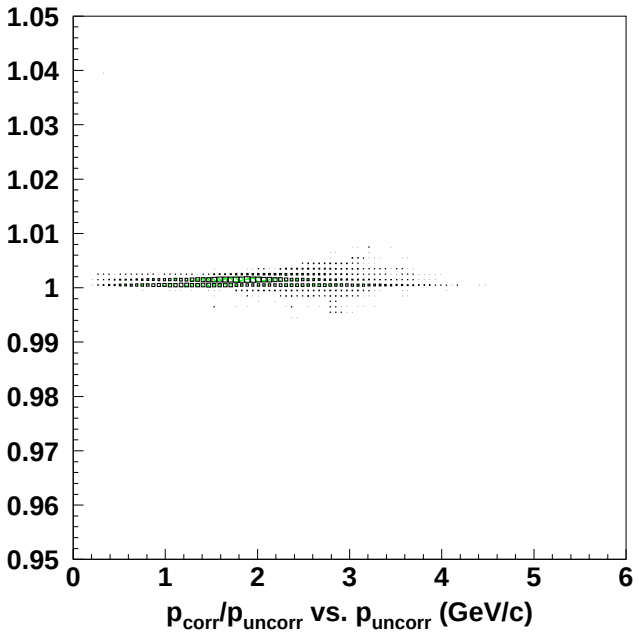

Figure 5.13: Plot shows the ratio of the corrected electron momentum to uncorrected electron momentum versus the uncorrected momentum. The electron momentum correction has a less than 1% effect for all applicable momenta.

The range of validity in these variables is ~ 0.2 GeV/c $\leq p_{reconstructed} \leq\sim 6.0$ GeV/c and $\sim 7^\circ \leq \theta_p \leq 120^\circ$. The parameters of the correction function were determined by running a GSIM simulation of only protons with momenta and scattering angles in the range specified above. The data was binned in θ_p and the parameters were obtained by a fit of $p_{generated}/p_{reconstructed}$ vs $p_{reconstructed}$ for each θ_p slice. Since the data is in the K^+ minimally-ionizing region, the above-mentioned energy correction was not applied to the K^+ sample [38].

5.2.7 Hadron Momentum Corrections

As is the case with the electron, the limitations of our knowledge of the CLAS magnetic field and geometry force the implementation of momentum corrections for hadron tracks. A set of momentum corrections based on kinematical fits using the

reactions $ep \rightarrow e\pi^+(n)$ and $ep \rightarrow ep(\gamma)$ were developed as a function of momentum, and azimuthal and polar angles. These corrections were applied to both the proton and K^+ sample, and although the corrections from this to the e1-6 data were small ($\sim 0.1 - 0.7\%$), they did have a overall "tightening" effect on the epK^+ missing mass peak width on a sector-by-sector basis [39]. As is illustrated in Table 5.2,

Sector	Before Correction		After Correction	
	M_{K^-}	σ_{K^-}	M_{K^-}	σ_{K^-}
1	0.4934	0.0136	0.4919	0.0137
2	0.4924	0.0126	0.4912	0.0124
3	0.4915	0.0127	0.4902	0.0125
4	0.4938	0.0124	0.4919	0.0125
5	0.4926	0.0135	0.4912	0.0136
6	0.4935	0.0139	0.4921	0.0138
Δ	0.0059	0.0033	0.0042	0.0038

Table 5.2: Values show the fitted mean and σ of the K^- peak for each sector before and after momentum corrections are applied to the proton and kaon samples. The last row shows the variances Δ of each column.

the momentum corrections decrease the variance of the means by $\sim 30\%$ effectively reducing sector-by-sector variations.

5.3 ϕ Event Identification

The purpose of the all the cuts mentioned above is to identify candidate ϕ events with the $epK^+(K^-)$ topology. After applying the data filtering techniques and cuts mentioned above, $23,282$ such events were identified. The sample contains all physical processes that contribute to this final state as well as real ϕ's and accidental background from pions. Contamination from high mass hyperons such as the Λ^* will be removed with a cut on the PK^- invariant mass.

Figure 5.14 shows the K^+K^- invariant mass with a highly-pronounced ϕ meson peak. This distribution is simultaneously fit to a Gaussian (whose integral is shown in

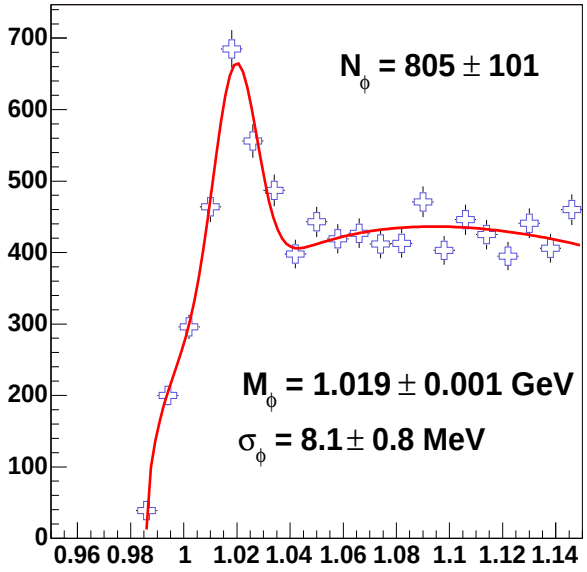

Figure 5.14: K^+K^- invariant mass including all data cuts and fit to ϕ peak with Eq. 5.10.

the green shaded region) plus an empirical phase space function for the background,

$$\begin{aligned} \mathsf{FIT} &= \mathsf{gaussian} + \mathsf{background} \\ \mathsf{gaussian} &= A\exp\left[\frac{-(\mathsf{IM_{kk}}-\mu)^2}{2\sigma}\right] \\ \mathsf{background} &= B_1\sqrt{\mathsf{IM_{kk}}^2 - M_{th}^2} + B_2\left(\mathsf{IM_{kk}}^2 - M_{th}^2\right) \end{aligned} \tag{5.10}$$

where M_{th} is the threshold for ϕ production (M_{th}=1.96 GeV), and A, B_1, and B_2 are extracted parameters of the fit. The mean μ and the width σ of the gaussian have been fixed at their average values for most of the fits to extract the ϕ yields. The total ϕ yield is extracted via:

$$N_\phi = \frac{\sqrt{2\pi}}{\Delta_{bin}} A\sigma \tag{5.11}$$

where A is the height of the Gaussian, σ is its width, and Δ_{bin} is the bin size of the histogram. This fit yields $N_\phi = 805$ and a mean $M_\phi = 1.019$ GeV and a width of 8.1

MeV. The statistical error σ_{N_ϕ} is given as

$$\sigma_{N_\phi} = N_\phi \sqrt{\frac{{\sigma_A}^2}{A^2} + \frac{{\sigma_\sigma}^2}{\sigma^2}} \tag{5.12}$$

5.3.1 Physics Background

There are competing channels which lead to a epK^+K^- final state. In order to successfully extract the ϕ signal, the contribution from these channels must be well-understood. The majority of this background comes from the production and subsequent decay of high-mass hyperons decaying via $ep \rightarrow e^{'}\Lambda^*(\Sigma^*)$ such as the $\Lambda^*(1520)$ as seen in Figure 5.15. In fact, the main contributor to the background is the $\Lambda^*(1520)$ whose cross section is similar to the ϕ. There are additional contributions from the $\Lambda^*(1600)$, $\Lambda^*(1800)$, $\Lambda^*(1820)$, $\Sigma^*(1660)$, and $\Sigma^*(1750)$. A cut on the pK^-

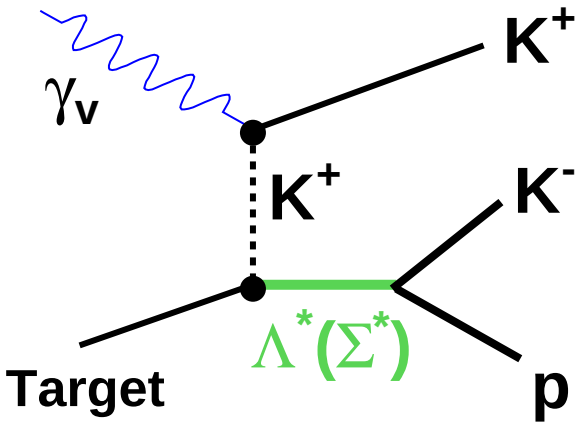

Figure 5.15: Feynman diagram for excited $\Lambda(1520)$ hyperon production. This is the primary background for $\phi(1020)$ production.

invariant mass is employed to cut out the $\Lambda^*(1520)$ contribution to the ϕ peak. This cut is illustrated in Figure 5.16. Instead of a single high-end cut on IM_{pK}, a "range" cut that removes the Λ peak and retains data below $IM_{pK} = 1.5$ GeV is employed. This procedure serves the two-fold purpose of retaining essentially all the ϕ statistics while increasing the signal-to-background ratio. The low end of the range cut is

$IM_{pK} = 1.49$ GeV and the high end is at $IM_{pK} = 1.55$ GeV, which equates to a 2σ cut. This is illustrated in Figure **??**. The criteria to select the best cut to eliminate the $\Lambda^*(1520)$ background was two-fold. The best cut would maximize the signal-to-background ratio as well as the ϕ yield. A summary of the various cut values investigated as well as their respective signal to background ratios and ϕ yields is shown in Table 5.3.

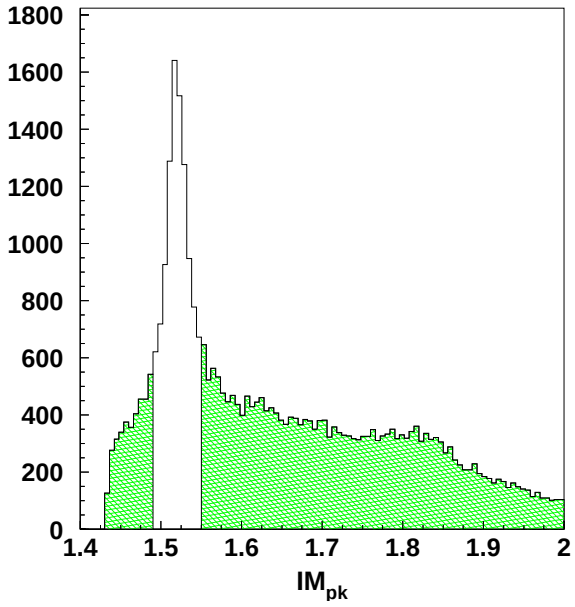

Figure 5.16: Plot of pK^- invariant mass. The $\Lambda^*(1520)$ removed by the cut (white) is clearly visible as well as the data kept (green shaded region).

The single-valued cuts, ranging between $IM_{pK} = 1.53$ GeV and $IM_{pK} = 1.57$ GeV result in a 23-27% loss in statistics and a $\sim 20\%$ decrease in the signal to background ratio. In sharp contrast, the range cut preserves essentially all the ϕ statistics as well as increasing the signal to background ratio by $\sim 13\%$. The reason for this becomes obvious if one investigates a plot of the IM_{KK} versus IM_{pK}, Figure 5.17. A sizable sample of ϕ's are located in the IM_{pK} phase space below 1.5 GeV which would be eliminated with a single-valued cut at $IM_{pK} = 1.53$ or above.

IM_{pK} **Cut**	**Signal to Background Ratio**	N_ϕ
No Cut	0.5664	972
$IM_{pK} = 1.53$	0.4535	754
$IM_{pK} = 1.54$	0.4698	762
$IM_{pK} = 1.55$	0.4662	760
$IM_{pK} = 1.56$	0.4759	748
$IM_{pK} = 1.57$	0.4913	716
Range Cut	0.6413	963

Table 5.3: Summary of investigated IM_{pK} cuts along with their respective signal to background ratios and ϕ yield.

5.4 Acceptance Correction

Before cross sections can be extracted, the ϕ yields must first be corrected for the detector acceptance. The acceptance is actually a combination of the geometrical acceptance of CLAS, the detector efficiencies of the SC and DC, the track reconstruction efficiency, and the event selection efficiency. It is calculated using a full GEANT-based simulation for CLAS called GSIM. Since the electromagnetic calorimeter and Cerenkov detectors aren't well modeled in GSIM, their efficiencies will be determined using the data. The acceptance correction proceeds in four main steps as follows:
EVENT GENERATOR ⇒ **GSIM** ⇒ **GPP** ⇒ **RECONSTRUCTION**

5.4.1 Event Generator

During the event generator step, events with the topology $ep \rightarrow ep\phi$ are generated according to a specific physics model whose parameters are adjusted to closely replicate the data. In the case of this analysis, the event generator **phi_gen** was written by the author specifically for the purpose of generating ϕ events according to the Vector Meson Dominance (VMD) model. The C++ based code takes as input various kinematical and model-based parameters summarized in Table 5.4 and generates ϕ events according to the following cross section:

$$\sigma_\phi{}^{VMD}(Q^2, W) = \sigma_\phi(0, W)\frac{p^*_\gamma(Q^2 = 0)}{p^*_\gamma(Q^2)}\frac{1+\epsilon}{(1+Q^2/\Lambda)^3}\exp(-b \mid t - t_{min}(Q^2) \mid) \quad (5.13)$$

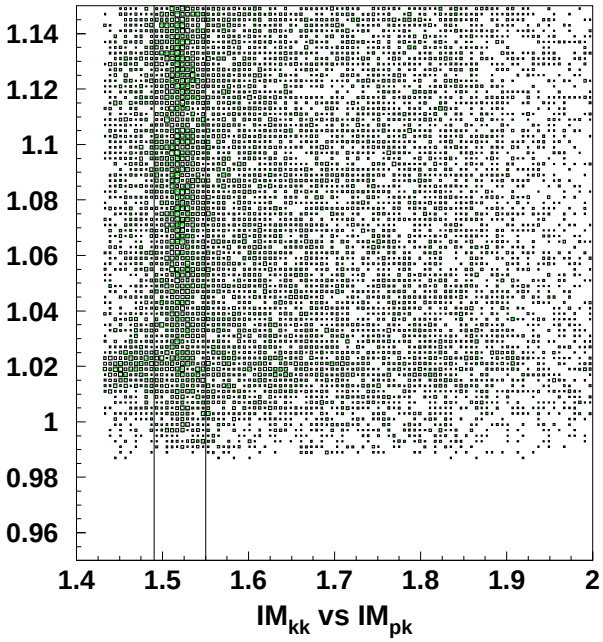

Figure 5.17: Scatter plot of IM_{KK} versus IM_{pK}. The well-defined vertical strip at $IM_{pK} = 1.52$ GeV is the $\Lambda(1520)$ band. The horizontal strip at $IM_{KK} = 1.02$ GeV is the ϕ band. The lines show the range cut applied to remove the Λ background. Also discernible are the ϕ events located below the low-end cut that would be thrown away with a single-valued cut above $IM_{pK} = 1.53$.

where $\sigma_\phi(0, W)$ is the photoproduction cross section, $\frac{p^*_\gamma(Q^2=0)}{p^*_\gamma(Q^2)}$ is a phase-space correction factor defined as $\frac{W^2-{M_p}^2}{\sqrt{(W^2-{M_p}^2-Q^2)^2+4W^2Q^2)}}$, ϵ is the polarization parameter (see chapter 1 section 1.1.1), $R = \frac{\sigma_L}{\sigma_T}$, and Λ is a scaling parameter. The cross section includes a factor $\exp(-b \mid t - t_{min}(Q^2) \mid)$ which describes the t behavior. The propagator is actually a modified from its normal $\frac{1}{Q^4}$ dependence to a $\frac{1}{Q^6}$ dependence to more closely resemble the data. A weighted 2-Dimensional histogram in Q^2 and ν is generated according to equation 5.13. This histogram is randomly sampled to produce all the kinematic distributions and quantities. In the VMD model, the decay process $\phi \rightarrow K^+K^-$ proceeds according to the angular decay distribution $W(\cos\theta_H, \psi)$, (see equation 7.4) and is included in the simulation. This is accomplished by creating a 2-Dimensional histogram in $\cos\theta_H$ and ψ weighted by $W(\cos\theta_H, \psi)$. The decay frame

Parameter	Value	Description
Beam Energy	5.754 GeV	e1-6 Beam Energy
Q^2 Range	1.0 to 5.0 GeV^2	Low and high range of Q^2
ν Range	2.5 to 4.3 GeV	Low and high range of ν
t Range	0.0 to -6.0 GeV^2	Low and high range of t
$\mathcal{L}_{int}$	$1.0 \times 10^{40} cm^{-2}$	integrated Luminosity
b	1.05	Impact parameter
ξ^2	0.33	VMD scaling parameter
$cos\delta$	0.70	L/T phase factor
Λ	1.039	Propagator scaling factor

Table 5.4: List of kinematic and VMD input parameters for the event generator phi_gen.

angles are then randomly sampled from this histogram.

For the present acceptance study, approximately 10 million events were generated.

5.4.2 GSIM

The generated events from phi_gen are then processed with a tagged version, release 4-5 of GSIM. GSIM is a GEANT based simulation of the CLAS detector which models the propagation of particle tracks through the CLAS detector components. As was previously mentioned, the GSIM modeling of the CC and to a lesser extent the EC, are unreliable so the efficiency of those subsystems will be calculated separately from the e1-6 data. The 4-5 release of GSIM was modified to include the GEANT implementation of the e1-6 target (Figure 2.4). The simulation of each $ep \rightarrow ep\phi$ event took approximately 0.875 seconds to complete on the JLAB batch farms. All 10 million generated events were propagated through GSIM which was completed in about 2 days.

5.4.3 GPP

In order to obtain realistic spacial and timing resolution as well as for the purpose of removing dead or inefficient DC and SC channels, the GSIM data is processed with the GSIM Post Processing (GPP) program. In order to deal with dead SC

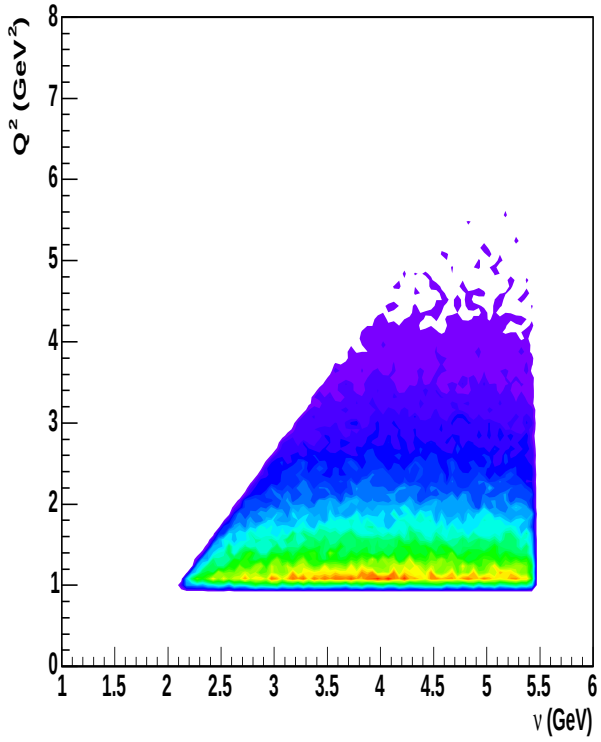

Figure 5.18: Generated, weighted Q^2 versus ν histogram used to obtain correlated Q^2 and ν values.

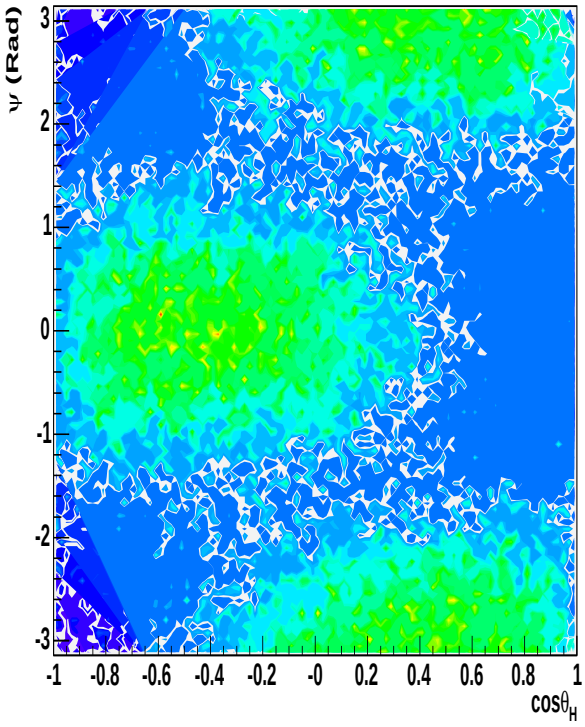

Figure 5.19: Generated ψ versus $\cos\Theta_H$ histogram weighted with $W(\cos\Theta_H, \psi)$ used to obtain correlated ψ and $\cos\Theta_H$ values.

counters, GPP simply references the SC status entries in the calibration database and removes them. GPP also accepts an SC smearing factor **f** at the command line which was optimized to match the timing resolution of the data. GPP also accepts 3 DOCA smearing factors **a, b,** and **c** which are responsible for smearing the drift chamber resolution for regions 1, 2, and 3 respectively. This smearing was matched to the data through the timing-independent epK^+ missing mass. The DOCA smearing factors were chosen to reproduce the resolution of K^- missing mass. The values of these parameters used in this study are summarized in Table 5.5. In addition to the smearing of the drift chambers, GPP also takes into account the individual wire efficiency through an efficiency lookup table constructed from the actual e1-6 data [40].

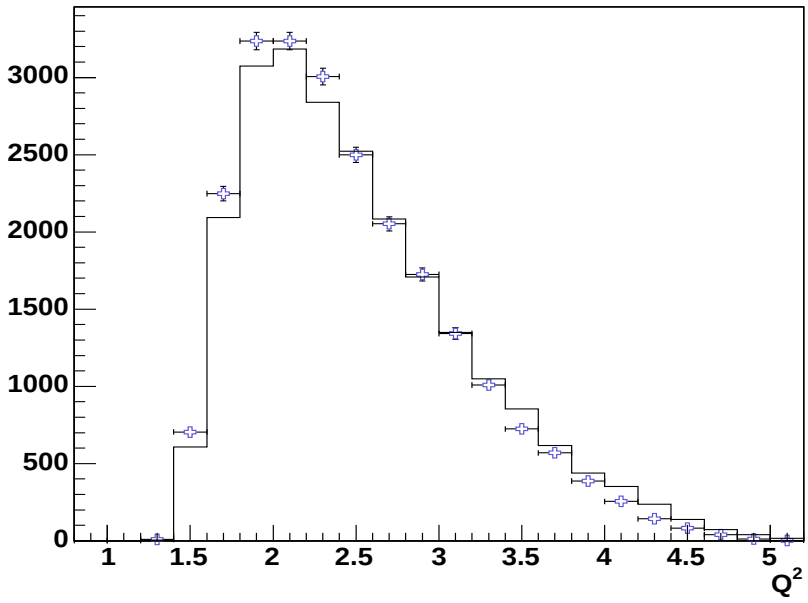

Figure 5.20: 23,000 reconstructed Monte Carlo events (histogram) overlayed with same amount of reconstructed data (blue error points).

5.4.4 Generated Track Reconstruction

After the previous steps are completed, the generated data, which is identical to the raw beam data, must be processed with RECSIS (see Section 4.1) the track reconstruction software. The generated data was processed with the same version, release 3-5 of RECSIS as was used to process the e1-6 data. This reconstructed data was then processed with the same cuts as the data except for the EC cuts. The energy loss correction was applied but not the momentum corrections since there are no ambiguities in the GSIM magnetic field or drift chamber positions.

5.4.5 Extraction of the Acceptance

The efficiency or acceptance is defined as the ratio of accepted events N_{acc} to generated events N_{gen} in a discrete phase space element Γ.

$$Acc(\Gamma) = \frac{N_{acc}(\Gamma)}{N_{gen}(\Gamma)} \tag{5.14}$$

Parameter	Value
f	1.30
a	2.25
b	2.25
c	2.25

Table 5.5: Summary of GPP input parameters

For this analysis, the acceptance will be calculated in 2-dimensional phase space elements of $d\Gamma = dQ^2dt$. Ideally these phase space elements should be as small as possible to eliminate any dependence of the acceptance calculation on the model used to generate the events. This is not especially important in this case since the event generator used is expected to reproduce the real data [10]. The event generator used very accurately represents the real data as is demonstrated in Figure 5.20 where the Q^2 histogram of reconstructed Monte Carlo events is overlayed with the Q^2 data with errors. The binning as well as the values for the acceptance calculation in Q^2 and t is shown in Table A.1. The binning for the Q^2,t' acceptance table is the same as the Q^2,t table. The extraction of the cross section in these variables is completed in coarser bins than the acceptance correction. For each 2-dimensional bin $(Q^2, -t)$, the acceptance or efficiency is defined as:

$$Acc(Q^2, -t) = \frac{N_{acc}(Q^2, -t)}{N_{gen}(Q^2, -t)} \tag{5.15}$$

where $N_{gen}(Q^2, -t)$ is the number of generated events in this bin and $N_{acc}(Q^2, -t)$ is the number of accepted events in this bin. It is desirable to extract the differential cross section in t' as well, so another acceptance table in Q^2 and t' is generated for this purpose. The binning is the same as for the table in Q^2 and t and is shown in Figure 5.22.

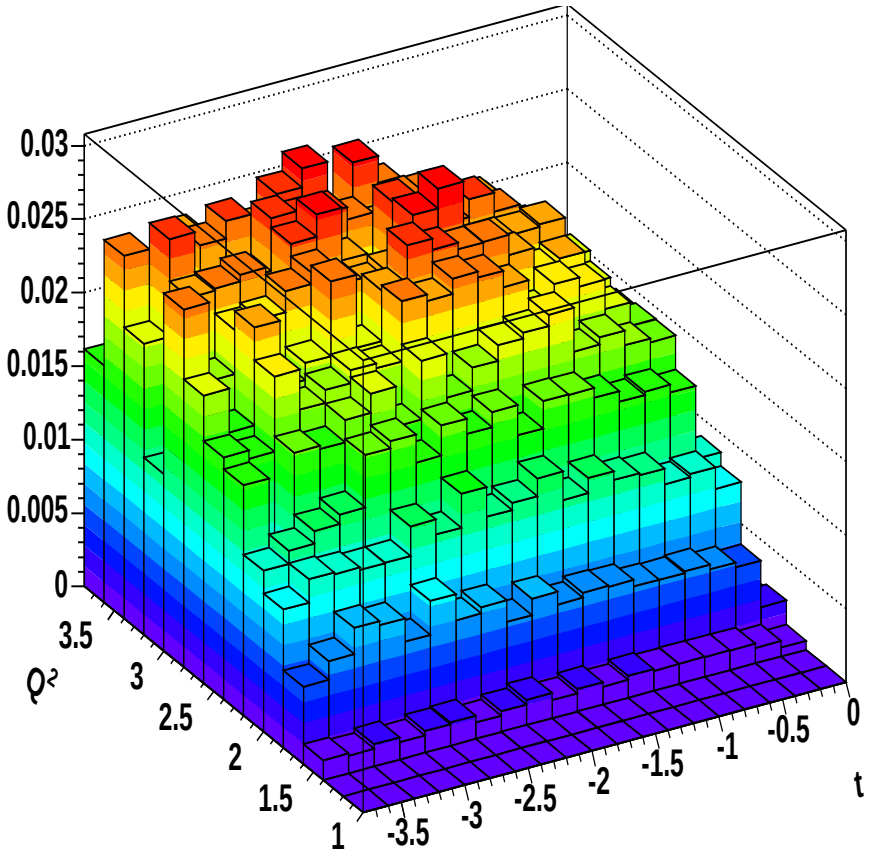

Figure 5.21: 2-dimensional representation of CLAS acceptance in Q^2 and t. Each "lego" represents a 0.2 GeV $\times$ 0.2 GeV 2-d bin. The z-axis is the efficiency for each bin.

5.5 Cherenkov Efficiency

The Cherenkov counters are not properly modeled in GSIM therefore a separate efficiency study had to be conducted. One can describe the electron signal from the CC by a generalized Poisson distribution

$$y\left(\frac{x}{C_3}\right) = \frac{C_1 C_2 \frac{x}{C_3} e^{-C_2}}{\Gamma(\frac{x}{C_3}+1)} \tag{5.16}$$

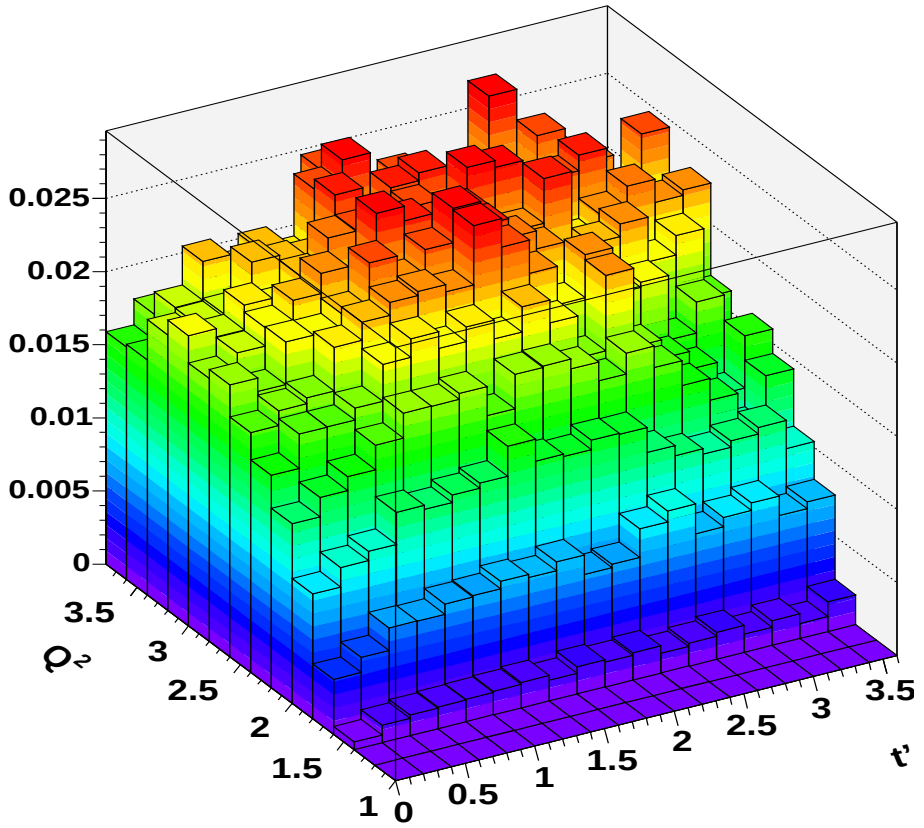

Figure 5.22: 2-dimensional representation of CLAS acceptance in Q^2 and t'. Each "lego" represents a 0.2 GeV $\times$ 0.2 GeV 2-d bin. The z-axis is the efficiency for each bin.

where C_1, C_2, and C_3 are adjustable fit parameters. C_1 is an overall amplitude, C_2 is the mean of the Poisson distribution and C_3 is a scaling parameter. The function was used to fit the Nphe x 10 distribution between 40 and 200 after all other electron selection cuts were made. These fit parameters were used to extrapolate the function to 0. The detection efficiency is then defined as

$$CC_{eff}(Q^2, x_B) = \frac{\int_{25}^{\infty} \mathrm{y(Nphe \quad x \quad 10)}}{\int_{0}^{\infty} \mathrm{y(Nphe \quad x \quad 10)}} \tag{5.17}$$

[10] The Cherenkov efficiency depends on Q^2 and x_B therefore this correction was calculated in Q^2 and x_B bins. One such example is shown in Figure 5.23 for $0.3 \leq x_B \leq 0.4$ and $1.8 \leq Q^2 \leq 2.0$.

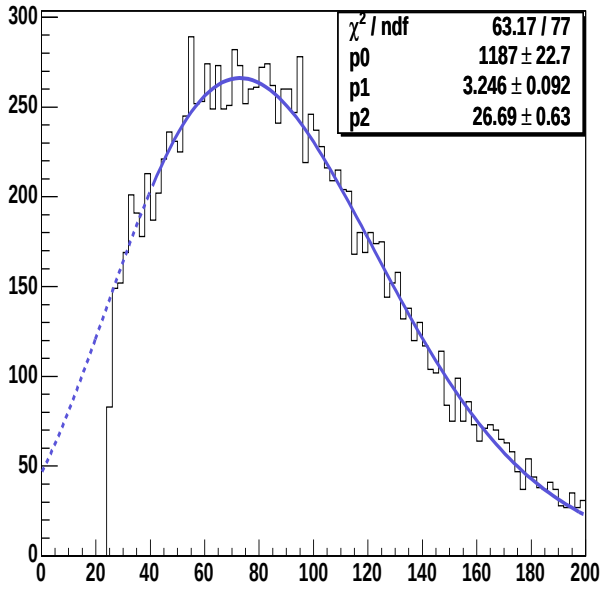

Figure 5.23: Plot shows Nphe x 10 distribution for scattered electrons after all electron selection cuts are made. The solid line shows a fit to the generalized Poisson distribution from 40 to 200 while the dashed line shows the extrapolation of the function to 0.

5.6 Radiative Corrections

Radiative effects must be taken into account when determining cross section values. In this analysis, the radiative effects are calculated in two distinct steps. The external radiative process, which is the finite probability that the incoming or scattered electron will radiate a hard photon in the presence of a nucleon in the target other than the one associated with the event are taken into account during the acceptance calculation at the GSIM step. There is also the possibility of the incoming electron (beam) to radiate external to the event. This effect is not modeled and will

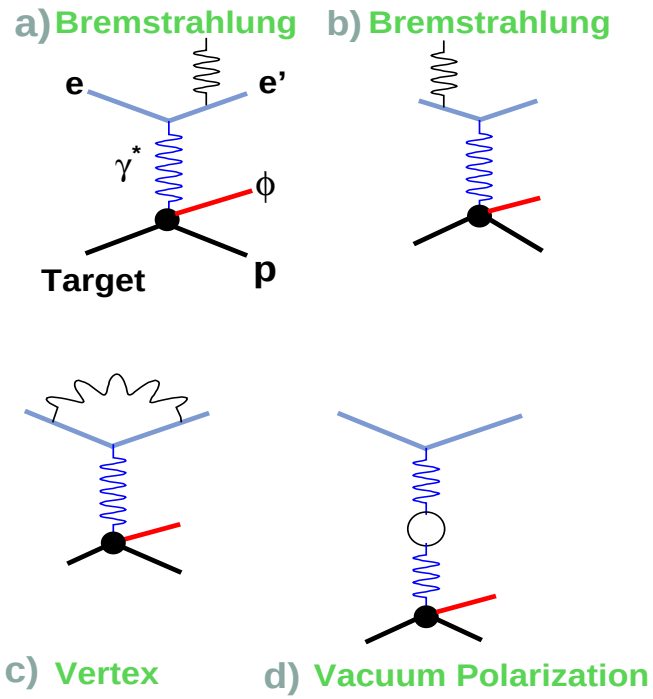

Figure 5.24: Contributing graphs of the radiative correction calculation Bremsstrahlung radiation (a), (b) self-absorption of radiated photon (c) and the internal loop of e^+/e^- pair production/annihilation (d). The born process (no radiated photon) is not shown.

be included in the systematic error of the correction, however such effects are partially taken into account in the intrinsic energy spread of the beam. The internal radiative corrections include the Bremsstrahlung process for the incoming or scattered electron in the presence of the nucleon associated with the event as well as diagrams such as vacuum polarization, which are not accounted for during the acceptance calculation, are shown in Figure 5.24. These internal corrections are calculated in a radiative correction factor F_{rad} using the radiative correction code *exclurad*, with $v_{cut} = 0.02$

GeV^2 [41]. F_{rad} [1] is calculated in each W and Φ bin as

$$F_{rad} = \frac{\sigma_{rad}}{\sigma_{norad}} \tag{5.18}$$

where σ_{norad} is the cross section calculated without any radiative effects (a.k.a. the Born cross section) and σ_{rad} is the cross section calculated with radiative effects included (diagrams 5.24 a-d). The correction factor for various W bins is shown as a function of Φ in Figure 5.25. The correction was made in W and Φ bins at average values of Q^2 and $\cos\theta_{CM}$ because the correction was found not to vary significantly in Q^2 and $\cos\theta_{CM}$.

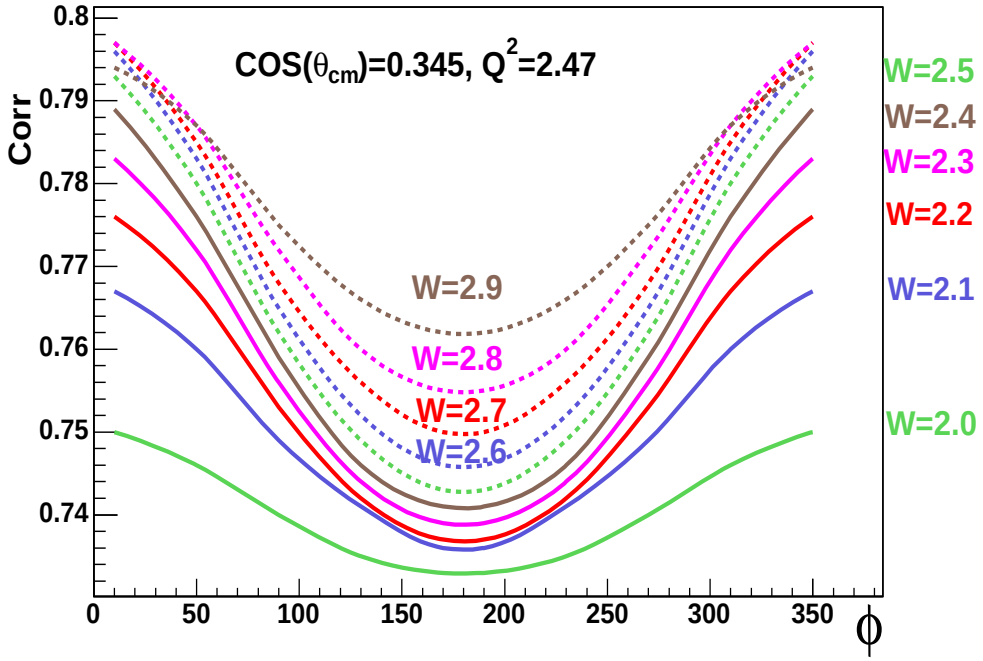

Figure 5.25: Plot of radiative correction F_{rad} as a function of $\Phi_{CM} = \Phi$ for assorted values of W from 2.0 to 3.0 GeV. The correction for each W value was computed at a $< Q^2 >= 2.47$ GeV^2 and $\cos\theta_{CM} = 0.345$.

[1] F_{rad} is δ as defined in Equation 75 of Reference [41].

5.7 Accumulated Charge Normalization

In order to properly normalize the cross section measurements, the total accumulated charge for the data analyzed must be known. This is accomplished by reading the information recorded in scalar events which retain a record of accumulated charge Q as measured by the Faraday cup. For the data set analyzed, the quantity FCG, which is the live time-gated reading from the Faraday cup, is read from these scalar events. There exists a slight ambiguity in measuring the accumulated charge using this method due to the scalar readout not being synchronized with the start of each run. In other words, there is a fraction of charge at the beginning and end of each run that is not accounted for. This uncertainty is estimated to be less than a 1% effect. For the data contained in this analysis, $Q = 22420 \times 10^{-6}$ Coulombs. Once the total charge Q is known, the integrated luminosity can be calculated as

$$\mathcal{L}_{int} = \frac{l_t \cdot D_t \cdot \mathcal{N}}{M_H} \cdot \frac{Q}{q_e} \tag{5.19}$$

where

- l_t is the length of the target (5.0 cm)
- D_t is the density of the target (0.0708 g/cm^3)
- $\mathcal{N}$ is Avagadro's number (6.022×10^{23})
- M_H is the molar density of Hydrogen (1.0 g/mol)
- q_e is the electron charge (1.6×10^{-19} C)

The integrated luminosity is then

$$\mathcal{L}_{int} = 2.98 \times 10^{40} \quad \mathsf{cm}^{-2} \tag{5.20}$$

Chapter 6

Cross Sections

6.1 Extraction of ϕ meson σ and $\frac{d\sigma}{dt}$ as a function of Q^2

6.1.1 $\sigma(Q^2, W)$

The total ϕ electroproduction cross section is given by

$$\sigma(Q^2, W, E_{beam}) = \frac{1}{\Gamma(Q^2, W, E_e)} \frac{d\sigma_\phi}{dQ^2 dW} \tag{6.1}$$

where $\Gamma(Q^2, W, E_e)$ is given by equation 1.16 and E_e enters through the polarization parameter ϵ given by equation 1.13. We can extract the ϕ cross section from the data via

$$\frac{d\sigma}{dQ^2 dW} = \frac{1}{BR_{\phi \to K^+K^-}} \frac{n_W}{\mathcal{L}_{int} \Delta Q^2 \Delta W} \tag{6.2}$$

where

- $BR_{\phi \to K^+K^-} = 0.491 \pm 0.009$ is the branching ratio of the decay $\phi \to K^+K^-$

- n_W is the acceptance-weighted, CC efficiency-weighted and radiative-correction weighted yield in each kinematic bin

$$n_W = \frac{N_\phi}{ACC(\Gamma) \cdot F_{rad} \cdot CC_{eff}} \tag{6.3}$$

where N_ϕ is defined in Equation 5.11.

- $\mathcal{L}_{int}$ is the integrated luminosity
- ΔQ^2 is the size of the Q^2 bin in GeV^2
- ΔW is the size of the W bin in GeV.

The binning in Q^2 and $-t$ for the extraction of the cross section in those variables are shown in Table 6.1. The binning in t' is the same as that used for t. In this analysis,

Variable	**Bin** (GeV^2)	**Bin Size** (GeV^2)	**Number of Acceptance Bins**
Q^2	1.6 - 1.8	0.2	1
	1.8 - 2.0	0.2	1
	2.0 - 2.2	0.2	1
	2.2 - 2.6	0.4	2
	2.6 - 3.0	0.4	2
	3.0 - 3.8	0.8	4
$-t$	0.0 - 0.4	0.4	2
	0.4 - 0.8	0.4	2
	0.8 - 1.2	0.4	2
	1.2 - 1.6	0.4	2
	1.6 - 2.0	0.4	2
	2.0 - 2.4	0.4	2
	2.4 - 2.8	0.4	2
	2.8 - 3.6	0.8	4

Table 6.1: Binning for the extraction of the cross sections in Q^2, t, and t' and the number of acceptance bins in each respective cross section bin. t' has the same binning and number of cross section bins as t so it is omitted in this table for brevity.

σ was integrated over the entire W range of $2.0 \leq W \leq 3.0$. This is allowable because the cross section varies only slightly with W. This permits one to express $\sigma(Q^2, W)$ as $\sigma(Q^2)$. To obtain the $\sigma(Q^2)$, each event is weighted for acceptance, radiative effects, the CC efficiency as well as the virtual photon flux factor. The invariant mass distribution (IM_{KK}) of weighted events in each Q^2 bin is then fit to equation 5.10. This is shown in Figure 6.1. The cross section for each of the bins is calculated

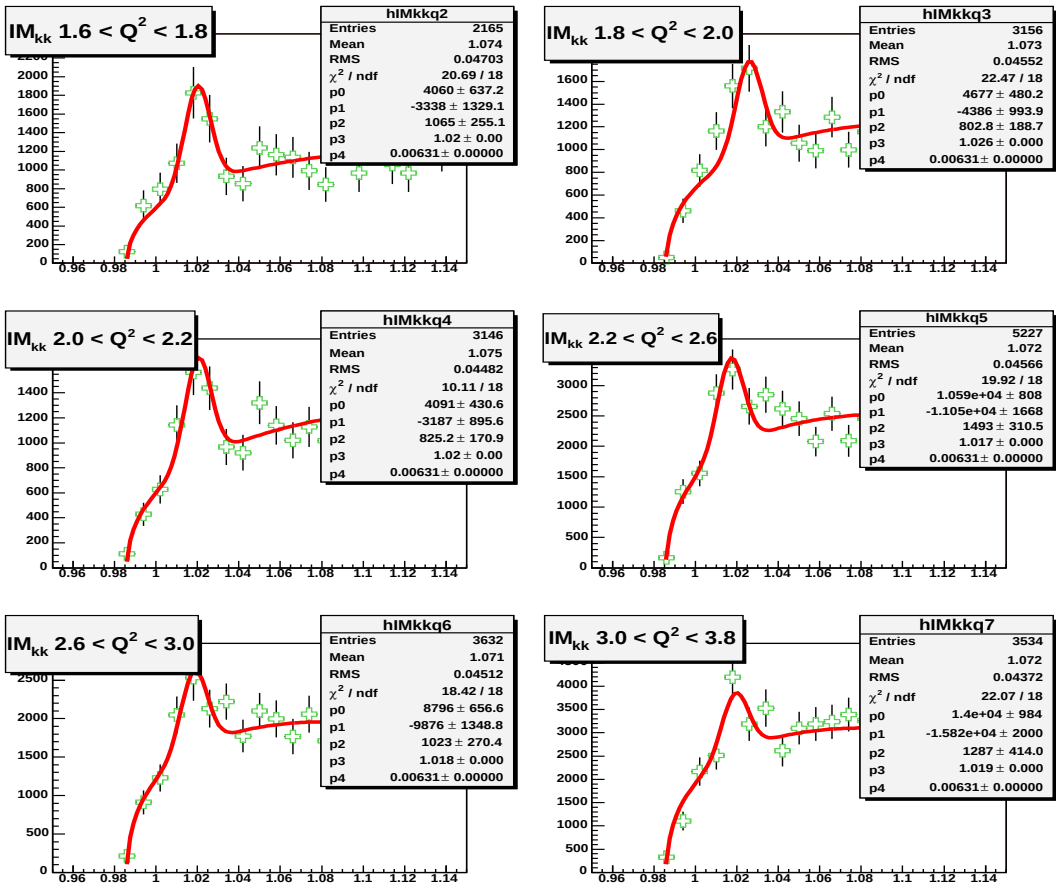

Figure 6.1: Fitted ϕ yields in given Q^2 bins given by a fit to Equation 5.10.

according to equations 6.1 and 6.2 and is shown along with previous JLab results, in Figure 6.2. The values for the cross section in each Q^2 bin as well as the relevant kinematics is shown in Table 6.2.

The total cross section was fit to determine the scaling behavior. For this data we determined the scaling to be $1/Q^{4.6\pm1.7}$ for $1.6 \leq Q^2 \leq 3.8$.

6.1.2 Differential Cross Section in t', $\frac{d\sigma}{dt'}$

The differential cross section in t' was extracted in 8 bins in t'. The fitted data is shown in Figure 6.3. The differential cross section plotted for each t' is shown in

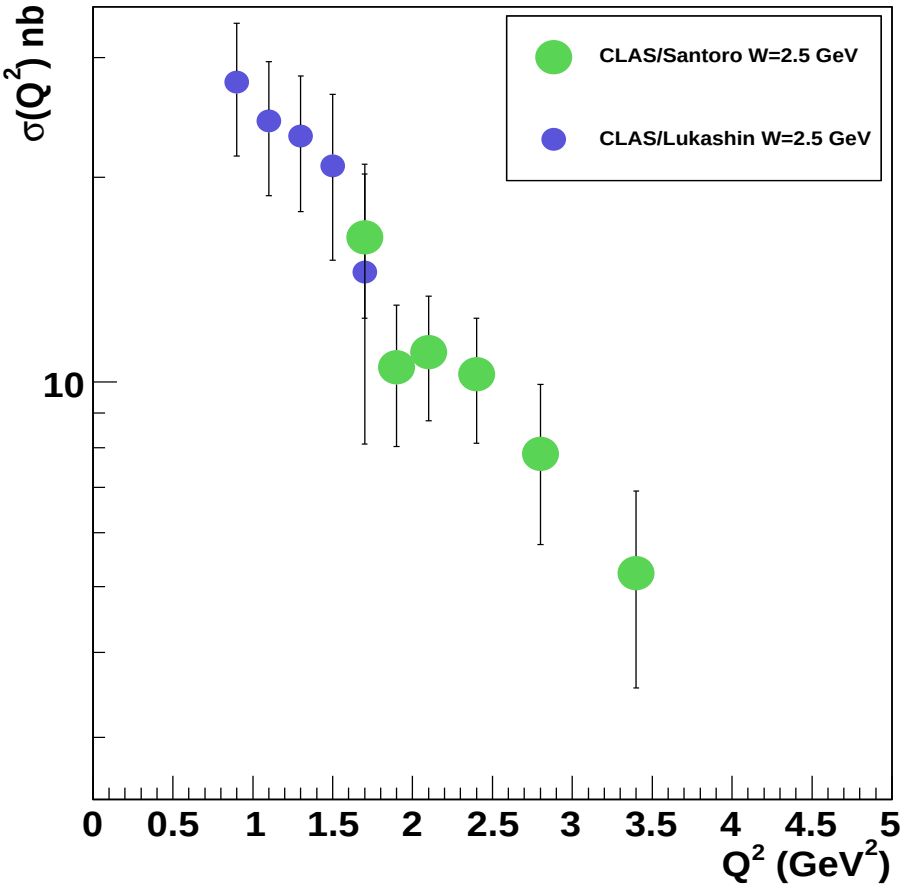

Figure 6.2: Plot shows $\sigma(Q^2)$ for all t and W values for a previous JLab data set [2] (blue points) and the from present analysis (green points).

Figure 6.4. The values for the cross section in each t' bin as well as the relevant kinematics is shown in Table 6.3.

6.1.3 Differential Cross Section in t, $\frac{d\sigma}{dt}$

The differential cross section is easiest to compare with theory if it is computed in terms of the Mandelstam variable t. Experientially, $\frac{d\sigma}{dt'}$ is often plotted, as in the previous section, in order to avoid corrections due to kinematic effects of the minimum 4-momentum transfer t_{min}. The differential cross section as a function of

Bin	$< Q^2 >$ (GeV^2)	$< \epsilon >$	σ (nb)
1	1.7	0.430	16.3 $\pm$ 3.9
2	1.9	0.475	10.5 $\pm$ 2.5
3	2.1	0.479	11.1 $\pm$ 2.3
4	2.4	0.459	10.3 $\pm$ 2.1
5	2.8	0.433	7.8 $\pm$ 2.0
6	3.4	0.387	5.2 $\pm$ 1.7

Table 6.2: Total cross section $\sigma(Q^2)$ and kinematics of each data point. $< Q^2 >$ is the bin center, and $< \epsilon >$ is the average ϵ in each bin.

Bin	$< t' >$ (GeV^2)	$< \epsilon >$	$\mathsf{d}\sigma/\mathsf{d}t'$ (nb/GeV^2)
1	0.19	0.453	7.2 $\pm$ 1.2
2	0.59	0.441	2.4 $\pm$ 0.8
3	0.99	0.435	2.3 $\pm$ 0.6
4	1.39	0.429	0.4 $\pm$ 0.4
5	1.79	0.430	1.2 $\pm$ 0.4
6	2.19	0.435	1.2 $\pm$ 0.3
7	2.59	0.426	0.5 $\pm$ 0.2
8	3.17	0.392	0.3 $\pm$ 0.1

Table 6.3: Differential cross section $\frac{d\sigma}{dt'}$ and kinematics of each data point. $< t' >$ is the bin center, and $< \epsilon >$ is the average ϵ in each bin.

t was extracted first for all values of Q^2, then for a Q^2 bin $1.6 \leq Q^2 \leq 2.6$ The differential cross section in t is given as

$$\frac{d\sigma}{dt} = \frac{\sigma}{\Delta t} \tag{6.4}$$

where Δt is the bin size in GeV^2 in which the cross section is extracted. A correction for $t_{min}(Q^2, W)$ is applied to relevant bins and is described in section 6.3. Such a correction is usually avoided by extracting and plotting the data as a function of t' but in order to compare to predictions of the JML model, the extraction versus t was necessary. $\frac{d\sigma}{dt}$ for all Q^2 is shown in Figure 6.5. The values for the cross section in each t bin as well as the relevant kinematics is shown in Table 6.4.

The data show very similar trends as previous data [2] namely they are consistent

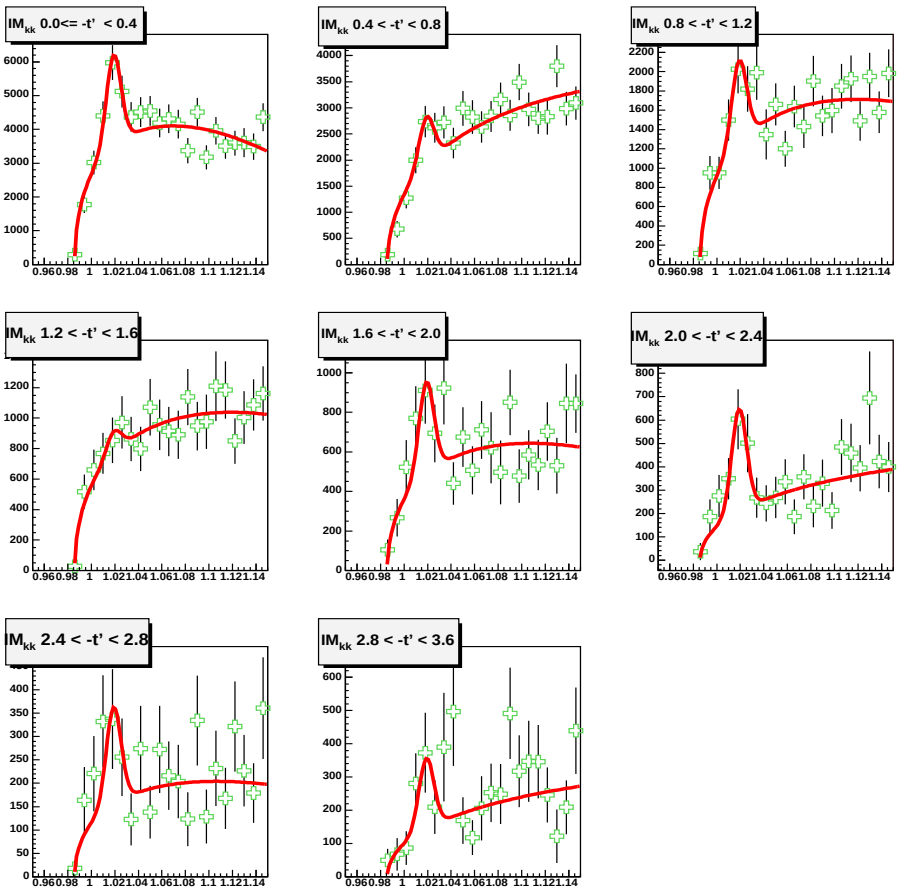

Figure 6.3: Fitted $\frac{d\sigma}{dt'}$ yields in t' bins given by a fit to Equation 5.10.

with diffractive production ($e^{-b|t|}$) below a $|t|$ of ≈ 1.5 GeV^2. $\frac{d\sigma}{dt}$ was extracted in two bins in Q^2 for comparison to the JML model. For our total Q^2 range, $1.6 \leq Q^2 \leq 4.0$ the data is shown in Figure 6.6 along with the JML predictions calculated in 2 Q^2 bins. The data in our truncated Q^2 bin, $1.6 \leq Q^2 \leq 2.6$ is shown in Figure 6.7 as well as the JML predictions calculated in one Q^2 bin.

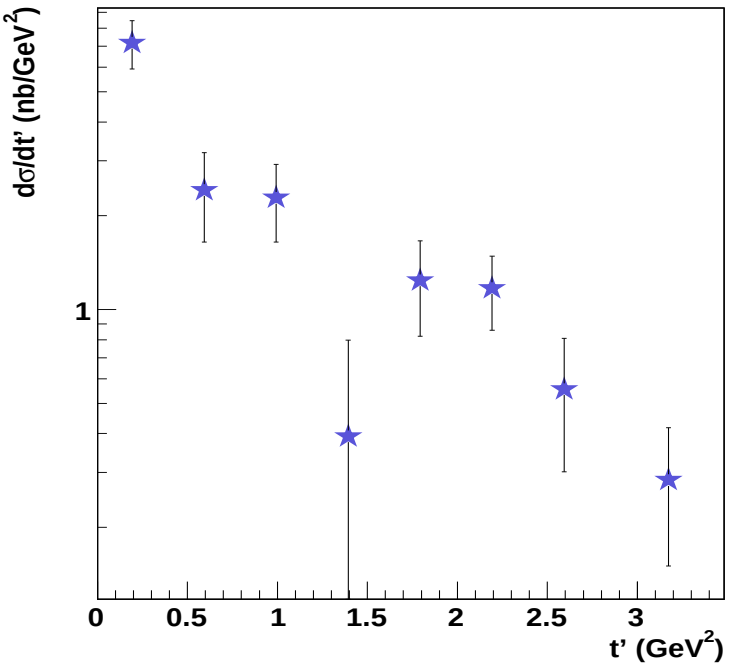

Figure 6.4: $\frac{d\sigma}{dt'}$ vs t' for all Q^2.

6.2 Bin Centering Correction

The distribution of data in each kinematical bin is not flat. As a result, the average value of the data in a bin doesn't coincide with the center but is offset depending upon the data distribution so any measurement made from data within that bin cannot be naively quoted at the center but rather where the real average of the data occurs. For this, a bin centering correction has to be made. An analytic form for the correction can be obtained if one makes an assumption of the functional form of the data. In this analysis, the bin centering correction was made for the t and t' distributions, which are assumed to have an exponential shape. This greatly simplifies the form of the correction:

$$x = x_0 - \frac{1}{b} \ln \frac{\sinh(p)}{p} \tag{6.5}$$

where x_0 is the center of the bin, b is the impact parameter measured from the fitted distribution, and $p = \frac{b\Delta}{2}$ where Δ is the bin width. It should be noted that one may

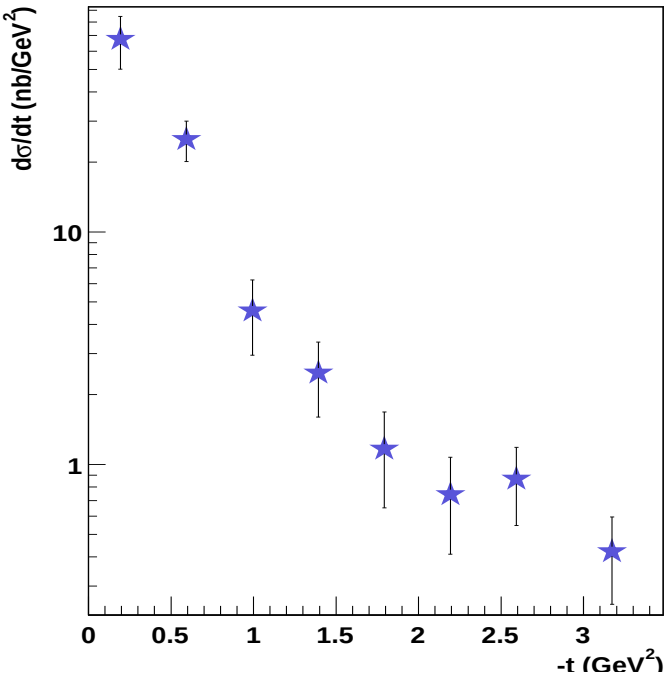

Figure 6.5: $\frac{d\sigma}{dt}$ vs -t integrated over the entire Q^2 range.

alternatively quote a modified value of the differential cross section $d\sigma/dt, d\sigma/dt'$ at the center of each bin.

6.3 $t_{min}(Q^2, W)$ Correction

In this section we correct for this kinematic effect assuming a simple form for the differential cross section. The differential cross section $\frac{d\sigma}{dt}$ contains contributions from all kinematically accessible Q^2 values

$$\frac{d\sigma}{dt} = \int_{Q^2{}_{min}}^{Q^2{}_{max}} \frac{d\sigma}{dt}(Q^2) dQ^2 \tag{6.6}$$

Bin	$< -t >$ (GeV^2)	$< \epsilon >$	$d\sigma/dt$ (nb/GeV^2)
1	0.19	0.361	67.5 ± 17.3
2	0.59	0.419	25.0 ± 4.9
3	0.99	0.445	4.6 ± 1.4
4	1.39	0.449	2.5 ± 0.9
5	1.79	0.447	1.2 ± 0.5
6	2.19	0.452	0.7 ± 0.3
7	2.59	0.450	0.9 ± 0.3
8	3.17	0.430	0.4 ± 0.2

Table 6.4: Differential cross section $\frac{d\sigma}{dt}$ and kinematics of each data point. $< -t >$ is the bin center, and $< \epsilon >$ is the average ϵ in each bin.

however experimentally, the Q^2 range accessible in each t bin is limited by t_{min} where

$$t_{min}(Q^2, W) = \left[\frac{Q^2 + M_\phi^2}{2W}\right]^2 - \left[\left[\left(\frac{W^2 - Q^2 + {M_\phi}^2}{2W}\right)^2 + Q^2\right]^{\frac{1}{2}} - \left[\left(\frac{W^2 + {M_\phi}^2 - {M_p}^2}{2W}\right)^2 - {M_\phi}^2\right]^{\frac{1}{2}}\right]^2 \tag{6.7}$$

$t_{min}(Q^2, W)$ is the momentum transfer t when the center-of-mass scattering angle θ_{CM}, the angle between the γ^* and ϕ is 0. $t_{min}(Q^2, W)$ is plotted in Figure 6.8. This translates into a truncation of the allowable Q^2 values contributing to $\frac{d\sigma}{dt}$. The range of Q^2 can be obtained by an inversion of $t_{min}(Q^2, W)$ and evaluated at a given t value corresponding to the center of a given t bin. Consequently, what is observed experimentally is

$$\left(\frac{d\sigma}{dt}\right)_{\mathsf{exp}} = \int_{{Q^2}_{min}}^{{t_{min}}^{-1}(Q^2,W)} \frac{d\sigma}{dt}(Q^2) dQ^2 \tag{6.8}$$

$\frac{d\sigma}{dt}$ is whatever function is used to model the t-dependence of the cross section. In the simplest case, there is no Q^2 dependence

$$\sigma(t) = A_\phi \mathsf{exp}(-b_\phi t) \tag{6.9}$$

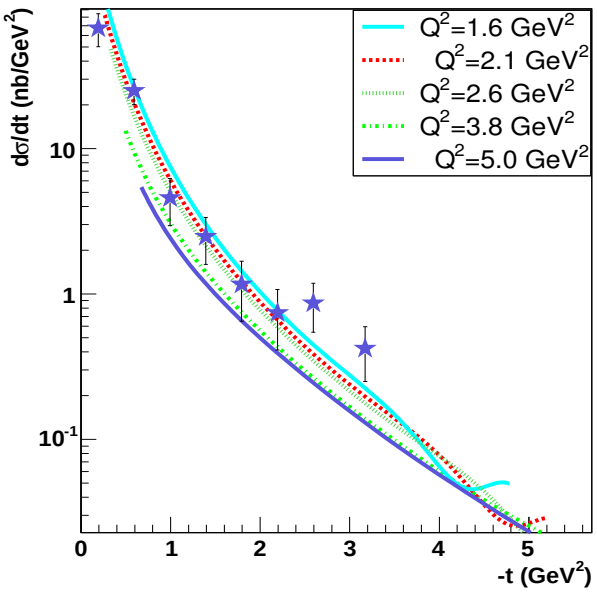

Figure 6.6: $\frac{d\sigma}{dt}$ vs -t for the entire Q^2 range and the JML predictions at 5 Q^2 points.

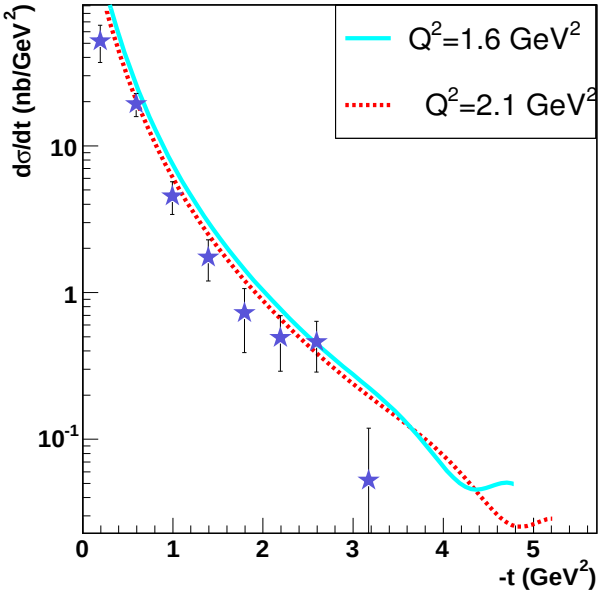

Figure 6.7: $\frac{d\sigma}{dt}$ vs -t for the Q^2 bin $1.6 \leq Q^2 \leq 2.6$ and the JML predictions.

In this case, the cross section just factors out. Given this, the correction factor for a given t bin is given by

$$\mathsf{F} = \frac{{t_{min}}^{-1}(Q^2, W; @t) - {Q^2}_{min}}{{Q^2}_{max} - {Q^2}_{min}} \tag{6.10}$$

The process of inverting $t_{min}(Q^2, W)$ equates to finding the roots of the polynomial $t_{min}(Q^2, W)$. The inversion of $t_{min}(Q^2, W)$ are then the physically meaningful roots of

$$t_{min}(Q^2, W) - t = 0 \tag{6.11}$$

In this analysis, the correction factor was extracted for all values of t at which $\frac{d\sigma}{dt}$ were extracted. At each t, the zeros of $t_{min}(Q^2, W)$ (${t^{-1}}_{min}(Q^2, W)$ were calculated for several W points in the range $2.0 \leq W \leq 3.0\ GeV^2$. The value used to calculate the correction factor at each t was actually an average over these points.

$${t^{-1}}_{min}(Q^2, W) = \frac{\sum_i {t^{-1}}_{min}(Q^2, W)_i}{N} \tag{6.12}$$

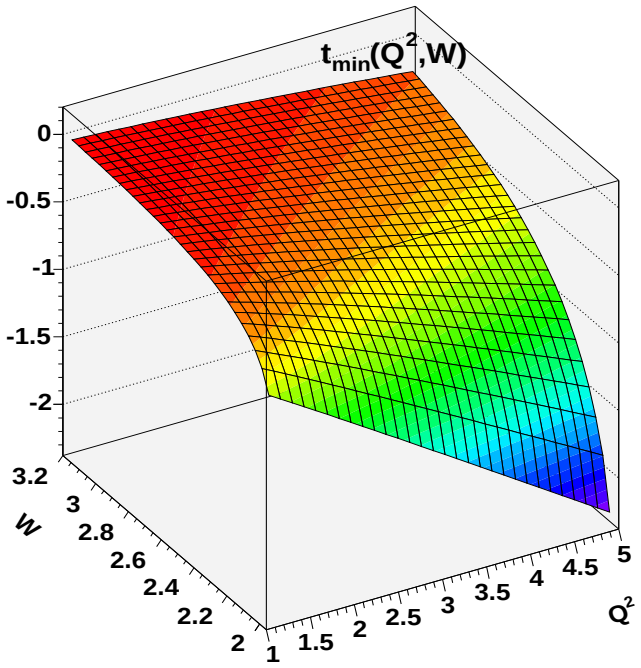

Figure 6.8: Plot of $t_{min}(Q^2, W)$ surface for e1-6 kinematics.

This correction is pictorially represented in Figure 6.9. A table of this correction factor for each t is given in Table 6.5, with the observed $\frac{d\sigma}{dt}$ is divided by this factor to obtain the corrected or true $\frac{d\sigma}{dt}$.

6.4 Systematic Error Estimates

The relatively low number of measured ϕ events leads to statistical domination of the errors. There were sources of systematic errors in this experiment and they can be summarized as follows:

- Fitting Procedure
- Acceptance Correction
- t_{min} Correction (applicable only to the extraction of $d\sigma/dt$).

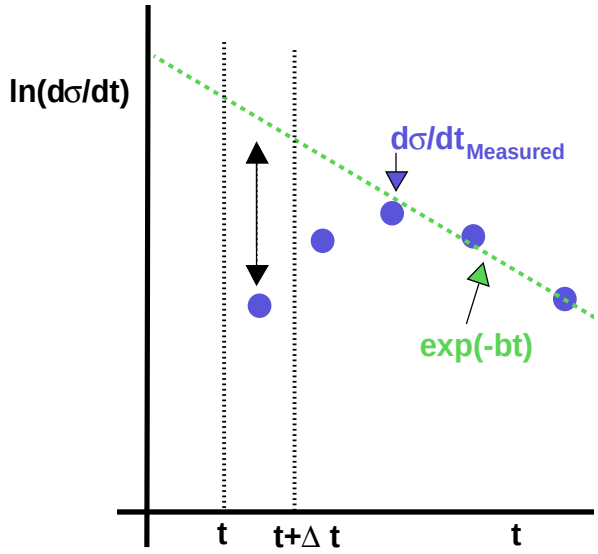

Figure 6.9: Plot illustrates the essence of the $t_{min}(Q^2, W)$ correction. The blue points represent the observed differential cross section as a function of t while the green dotted curve represents where these points should fall in the absence of t_{min} effects i.e. if one plotted the differential cross section as a function of $t^{'} = t - t_{min}(Q^2, W)$. It is important to note that the green curve represents the t-dependence of the cross section assuming some model and can assume various forms.

$< -t >$(GeV^2)	$t^{-1}{}_{min}(Q^2, W)$(GeV^2)	Low Q^2 F	all Q^2 F
0.2	1.48	0.12	0.03
0.6	1.85	0.65	0.19
1.0	2.35	1.0	0.40
1.4	2.87	1.0	0.62
1.8	3.37	1.0	0.84
2.2	3.88	1.0	1.0
2.6	4.37	1.0	1.0
3.2	5.09	1.0	1.0

Table 6.5: $t_{min}(Q^2, W)$ Correction values for each t bin in which the cross section is extracted.

Chapter 7

Angular Distributions

7.1 Background

The angular decay distribution of the $K^+(K^-)$ in the ϕ rest frame describes the polarization properties of the ϕ meson. The scattering amplitude $\mathcal{M}$ for vector meson electroproduction $\gamma^* + N \rightarrow P + V$ can be expressed in terms of helicity amplitudes $T_{\lambda_V \lambda_P \lambda_{\gamma^*} \lambda_N}$ where λ is the helicity of each particle. The vector meson spin density matrix is derived from these helicity amplitudes by exploiting the Von Neumann formula

$$\rho(V) = \frac{1}{2} T \rho(\gamma^*) T^\dagger \tag{7.1}$$

where $\rho(\gamma^*)$ is the spin-density matrix of the virtual photon. The details of this derivation can be found in reference [1, 42]. The decomposition of $\rho(V)$ can be accomplished on a basis of nine 3 x 3 hermetian matrices ρ^α_{ij}. The index α ranges from 0 to 8 and corresponds to the particular decomposition. This index can also be related to the virtual photon polarization $\alpha = 0 - 2$ for purely transverse photons, $\alpha = 4$ for purely longitudinal photons while other values correspond to Longitudinal-Transverse interference terms. The indices ij correspond to the helicity state of the vector meson; for instance ρ^0_{00} is proportional to the probability that a transversely polarized virtual photon will produce a longitudinally polarized ($\lambda = 0$) vector meson while ρ^0_{01} is an interference term between a meson of helicity 0 and a meson of helicity 1 produced by a transversely polarized virtual photon [10]. In the case that there is

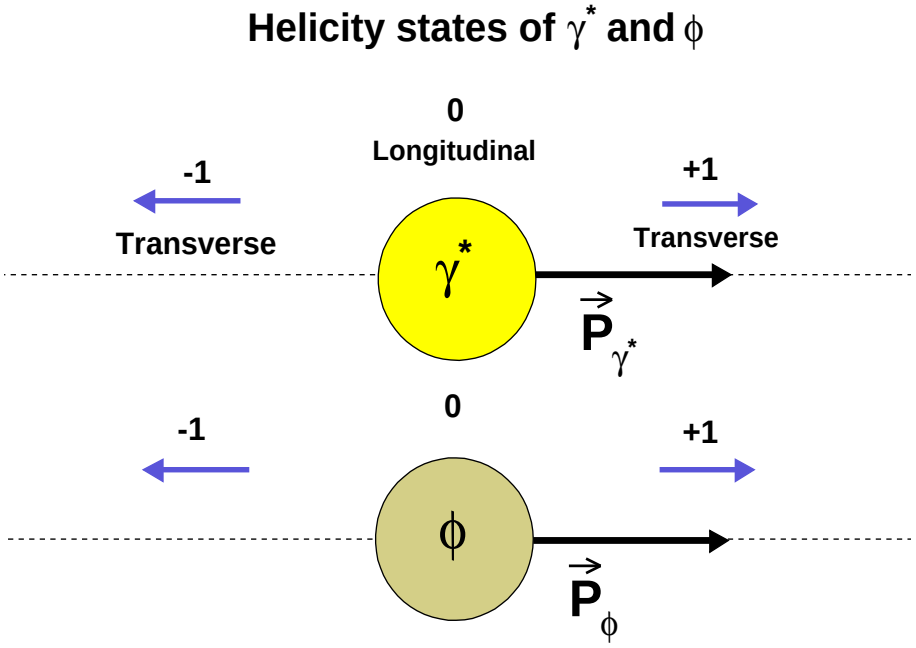

Figure 7.1: Helicity states of the virtual photon and ϕ. The blue arrows indicate the spin directions corresponding to each helicity state.

no σ_L/σ_T separation, ρ^{α}_{ij} can be parameterized as follows

$$\begin{aligned} r^{04}_{ij} &= \frac{\rho^{0}_{ij} + \epsilon R \rho^{4}_{ij}}{1+\epsilon R} \quad ; \quad \alpha = 4 \\ r^{\alpha}_{ij} &= \frac{\rho^{\alpha}_{ij}}{1+\epsilon R} \quad ; \quad \alpha = 0-3 \\ r^{\alpha}_{ij} &= \sqrt{R}\frac{\rho^{\alpha}_{ij}}{1+\epsilon R} \quad ; \quad \alpha = 5-8 \end{aligned} \tag{7.2}$$

where R and ϵ retain their earlier definitions.

In terms of these parameters, the full angular decay distribution assumes the normalized form

$$W\Big(\cos\theta_H, \phi_H, \Phi\Big) = \frac{3}{4\pi}\Big[\frac{1}{2}(1-r^{04}_{00}) + \frac{1}{2}(3r^{04}_{00}-1)\cos^2\theta_H$$

$$
\begin{aligned}
&-\sqrt{2}\mathsf{Re}\, r_{10}^{04} \sin 2\theta_H \cos\phi_H - r_{1-1}^{04} \sin^2\theta_H \cos 2\phi_H \\
&-\epsilon\, \cos 2\Phi\{r_{11}^1 \sin^2\theta_H + r_{00}^1 \cos^2\theta_H - \sqrt{2}\mathsf{Re}\, r_{10}^1 \sin 2\theta_H \cos\phi_H \\
&-r_{1-1}^1 \sin^2\theta_H \cos 2\phi_H\} \\
&-\epsilon\, \sin 2\Phi\{\sqrt{2}\mathsf{Im}\, r_{10}^2 \sin 2\theta_H \sin\phi_H + \mathsf{Im}\, r_{1-1}^2 \sin^2\theta_H \sin 2\phi_H\} \\
&+\sqrt{2\epsilon(1+\epsilon)} \cos\Phi\{r_{11}^5 \sin^2\theta_H + r_{00}^5 \cos^2\theta_H - \sqrt{2}\mathsf{Re}\, r_{10}^5 \sin 2\theta_H \cos\phi_H \\
&-r_{1-1}^5 \sin^2\theta_H \cos 2\phi_H\} \\
&+\sqrt{2\epsilon(1+\epsilon)} \sin\Phi\{\sqrt{2}\mathsf{Im}\, r_{10}^6 \sin 2\theta_H \sin\phi_H + r_{1-1}^6 \sin^2\theta_H \sin 2\phi_H\}\Big]
\end{aligned}
\tag{7.3}
$$

One of the primary goals of this analysis is to test SCHC. If SCHC holds then by definition $r_{00}^0 = 0$ and $r_{00}^{04} = \frac{\epsilon R}{1+\epsilon R}$, where equation 7.3 reduces to the simpler form with the introduction of $\psi = \phi_H - \Phi$:

$$
\begin{aligned}
W\Big(\cos\theta_H, \psi) = \frac{3}{8\pi}\frac{1}{1+\epsilon R}\Bigg[& \sin^2\theta_H + 2\epsilon R \cos^2\theta_H \\
& + 2(1+\epsilon R)\epsilon\Big(r_{1-1}^1 - \mathsf{Im} r_{1-1}^2\Big) \sin^2\theta_H \cos 2\psi \\
& + 2(1+\epsilon R)\, 2\sqrt{2\epsilon(1+\epsilon)} \sin 2\theta_H \cos\psi\Big(\mathsf{Im} r_{10}^6 - \mathsf{Re} r_{10}^5\Big)\Bigg]
\end{aligned}
\tag{7.4}
$$

7.2 Acceptance Correction for the Angular Distribution

Analogous to the acceptance tables $\mathrm{ACC}(Q^2, t)$, $\mathrm{ACC}(Q^2, t')$, an acceptance table in $\mathrm{ACC}(\psi, \cos\theta_H)$ is defined for the extraction of the projections of the angular dis-

tributions $\frac{dN}{d\psi}$ and $\frac{dN}{d\cos\theta_H}$. Ten million Monte Carlo events were generated with the phi++ generator assuming the SCHC form of the angular distribution (see Figure 5.19). The bin size for each variable is shown in Table 7.1. The correction is shown graphically in Figure 7.2. The events that were used to generate this acceptance table

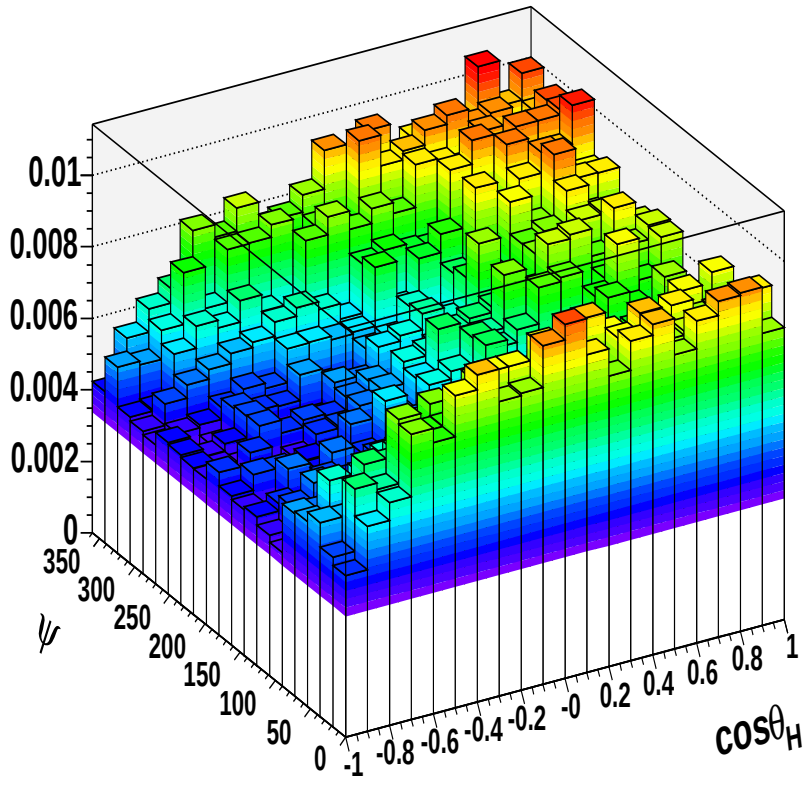

Figure 7.2: 2-dimensional representation of CLAS acceptance in ψ and $\cos\theta_H$. Each bin represents a 18.0 Degree $\times$ 0.1 units of $\cos\theta_H$ 2-d bin. The z-axis is the efficiency for each bin.

were the same as those used for the previous acceptance tables. In a similar fashion to the previous acceptance table, the weight of events was limited to be less than 400.

Variable	Range	Number of Bins	Bin Size
ψ (Degrees)	0 to 360	20	18°
$\cos\theta_H$	-1 to 1	20	0.1

Table 7.1: Acceptance table values for the extraction of the angular distribution.

7.3 Extraction of r_{ij}^{α} parameters

7.3.1 Differential Cross Section $\frac{d\sigma}{d\Phi}$ and test of SCHC

The differential cross section in Φ were extracted in the same manner as the other differential cross sections. Due to the limited statistics of this experiment, $\frac{d\sigma}{d\Phi}$ was extracted for integrated Q^2 and t' so a one dimensional acceptance correction in 20 Φ bins was used. $\frac{d\sigma}{d\Phi}$ was extracted in 9 bins whose respective fits are shown in Figure 7.3. The expected Φ dependence arises from integrating equation 7.3 in $\cos\theta_H$,and

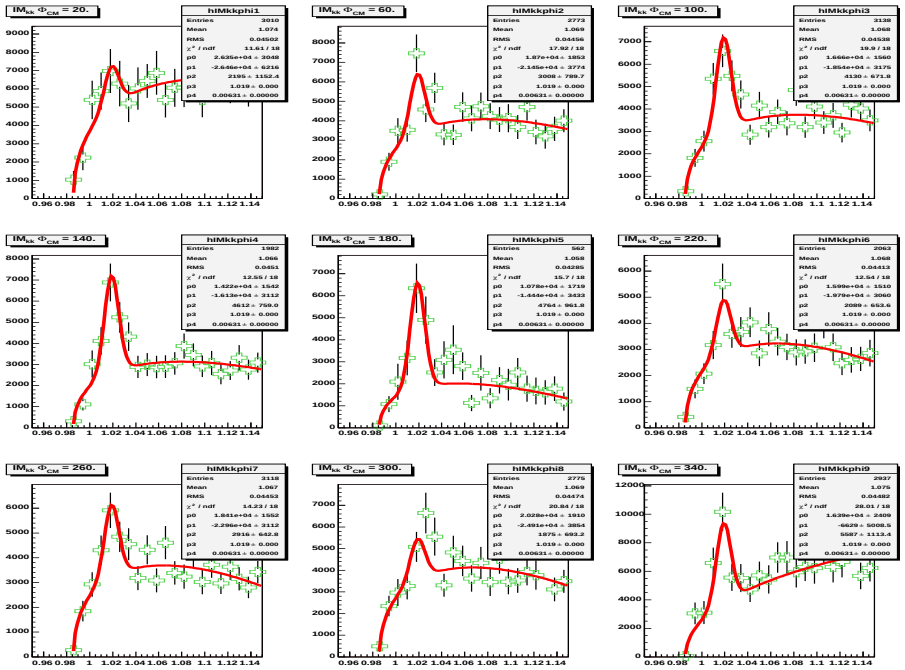

Figure 7.3: Fits to K^+K^- invariant mass in 9 bins in Φ_{CM}

ϕ_H to obtain:

$$\frac{d\sigma}{d\Phi} = \frac{1}{2\pi}\left(\sigma + \epsilon\cos 2\Phi\sigma_{TT} + \sqrt{2\epsilon(1+\epsilon)}\cos\Phi\sigma_{LT}\right) \tag{7.5}$$

where σ_{LT} and σ_{TT} are the interference terms of the longitudinal and transverse parts of the cross section. The cross section along with a fit to equation 7.5 is shown in

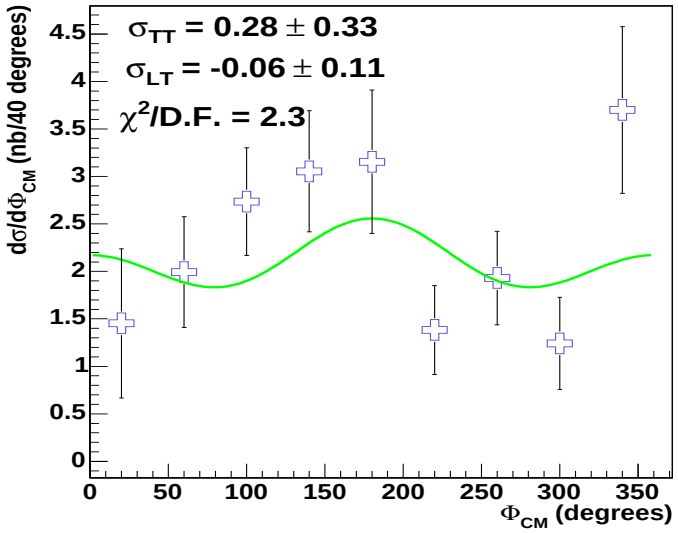

Figure 7.4: $\frac{d\sigma}{d\Phi}$ vs Φ. Green line shows a fit to equation 7.5 along with extracted fit parameters σ_{TT} and σ_{LT}.

Figure 7.4. If SCHC is a valid assumption then these interference terms must vanish [10]. It can be concluded from Figure 7.4 that these terms are compatible with zero. The errors quoted are purely statistical so the inclusion of systematic errors associated with the acceptance calculation, etc would only strengthen our conclusion. A fit of the $d\sigma/d\Phi$ distribution to a constant yields $\chi^2/D.F. = 1.9$ ($\chi^2 = 15.2$) as opposed to a $\chi^2/D.F. = 2.3$ ($\chi^2 = 13.8$) from a fit to Equation 7.5 indicates compatibility with zero. In order to extract the r_{ij}^{α} parameters from the measured angular distribution, one has the option of taking two 1-dimensional projections of equation 7.3.

7.3.2 Polar Angular distribution projection

To obtain the polar angular distribution, an integration in Φ and ϕ_H (or ψ) yields

$$W(\cos\theta_H) = \frac{3}{2}\left[\frac{1}{2}\left(1 - r_{00}^{04}\right) + \frac{1}{2}\left(3r_{00}^{04} - 1\right)\cos^2\theta_H\right] \tag{7.6}$$

In order to obtain this projection from the data, the acceptance-efficiency-radiative correction-weighted distribution K^+K^- invariant mass is extracted in 10 bins in $\cos\theta_H$ (0.20 units of $\cos\theta_H$ each). The same fit to a Gaussian plus a polynomial background was made to extract the weighted yields in each of these bins as shown in Figure 7.5.

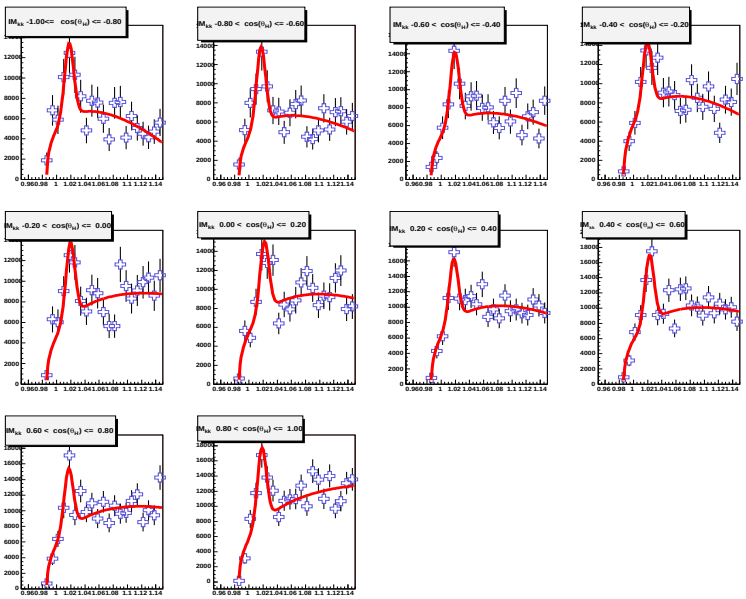

Figure 7.5: K^+K^- invariant mass in $\cos\theta_H$ bins plus a fit to equation 5.10 (red line).

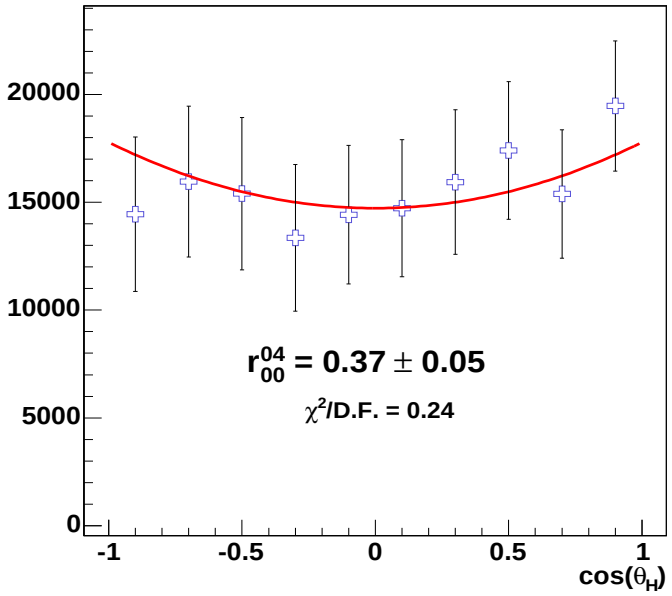

Figure 7.6: $\frac{dN}{d\cos\theta_H}$ extracted for all Q^2 values plus a fit to equation 7.6. Also shown is the extracted r_{00}^{04} parameter.

7.3.3 Angular distribution projection in ψ

After an integration in $\cos\theta_H$, a substitution of $\phi_H = \psi + \Phi$, an integration in Φ, and some algebra, the projected angular distribution in ψ is given as

$$W(\psi) = \frac{1}{2\pi}\left[1 + \epsilon\left(r_{1-1}^1 - \mathsf{Im}r_{1-1}^2\right)\cos 2\psi\right] \tag{7.7}$$

The factor of $\frac{1}{2\pi}$ is a normalization factor. A fit of $\frac{dN}{d\psi}$ to Eq. 7.7 shown in Figure 7.7 determines the difference $r_{1-1}^1 - \mathsf{Im}r_{1-1}^2$. If the SCHC assumption is valid then $r_{1-1}^1 = -\mathsf{Im}r_{1-1}^2$, where the fit yields $r_{1-1}^1 - \mathsf{Im}r_{1-1}^2 = 0.09 \pm 0.08$. An alternative method of determining r_{1-1}^1 or $\mathsf{Im}r_{1-1}^2$ can be made using the method of moments.

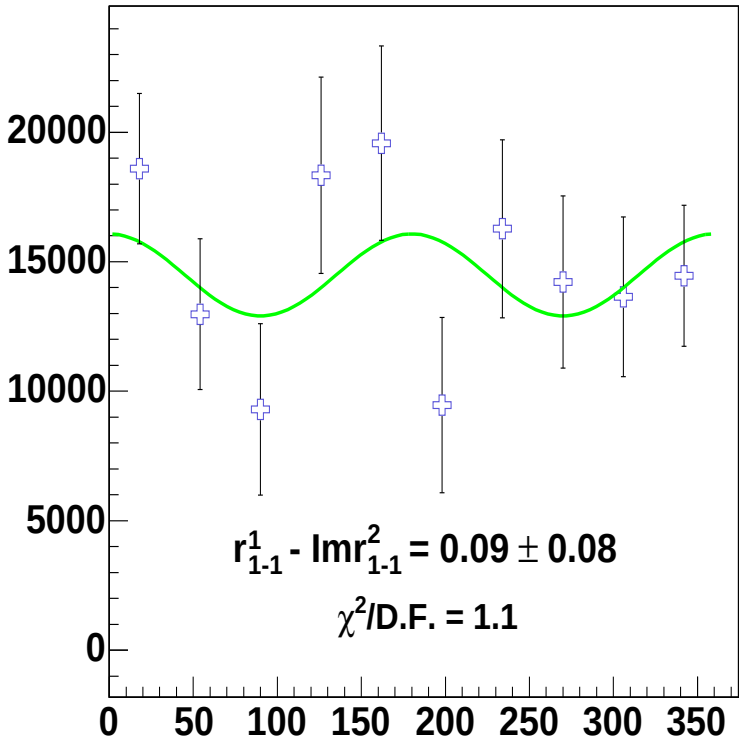

Figure 7.7: $\frac{dN}{d\psi}$ extracted for all Q^2 values plus a fit to equation 7.7.

Chapter 8

Conclusions

8.1 Comparison to Previous Data

The measurements of $\sigma(Q^2)$ from the present analysis along with the previous CLAS measurement [2] was shown in Figure 6.2. The one overlap point at $Q^2 = 1.7$ is in good agreement with the previous CLAS data. The data at low W [2, 25, 3, 43] is the most relevant for comparison to our data. The total cross sections are plotted in Figure 8.1 along with assorted data sets tabulated in Table 1.1. The data shows a similar trend to [2] and is good agreement with the overlapping data point as well as with the overlap point of the data from [25]. There is no overlap between our data and the DESY or H1 data because of the different [3, 25] ranges in W, but these data do demonstrate a common behavior. There are errors on the DESY points however they are relatively small compared to the other data sets.

8.2 Comparison to VMD Model

The VMD model predicts an exponential form for the t' behavior of the cross section

$$\frac{d\sigma}{dt'} = A_\phi \mathsf{e}^{-b_\phi t'} \tag{8.1}$$

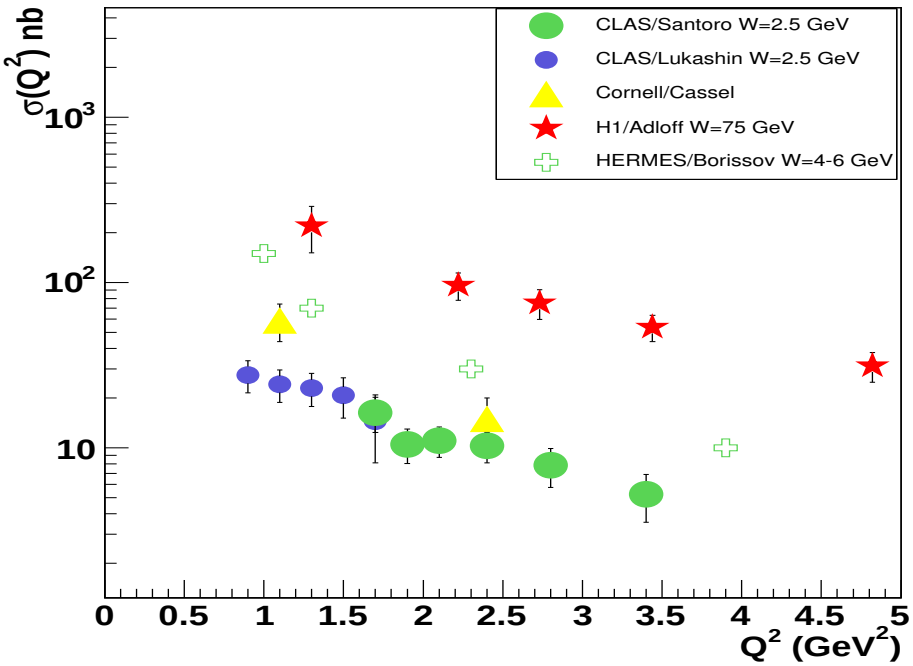

Figure 8.1: Total cross sections as a function of Q^2 for our data (green points), previous JLab data (blue points)[2], Cornell data (triangles) [3], HERMES data for W between 4 and 6 GeV^2, and HERA data at high W (W=75 GeV^2).

If the interaction is assumed to proceed diffractively, b_ϕ can be related to the radius of interaction R_{int} between the virtual ϕ and the target proton. [1]

$$b_\phi = \frac{R_{int}^2}{4} \tag{8.2}$$

and is thusly referred to as the impact parameter. The measurement of $\frac{d\sigma}{dt'}$ permits the extraction of b_ϕ through a fit of equation 8.1. Figure 8.2 shows a fit of the measured differential cross section to equation 8.1 yielding a $b_\phi = 0.99$ GeV^{-2} ($R_{int} = 0.39$ fm) for the full range of the data. This corresponds to about one quarter the diameter of the nucleon (proton). The presence of a diffractive minima at $t' = 1.4$ GeV^2 is quite apparent in Figures 8.2 and 8.3 so the fit above was repeated for the region

[1] R_{int} in diffractive ϕ production is analogous to the classical light-scattering aperture of radius R[20].

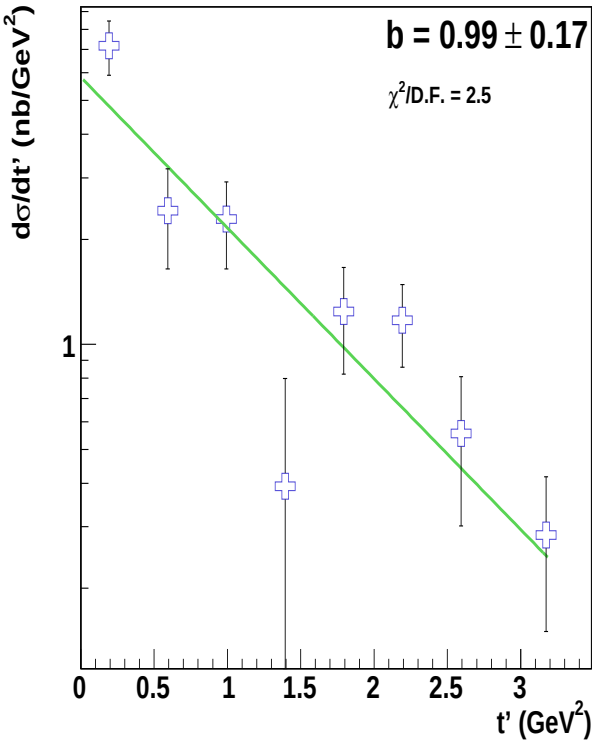

Figure 8.2: Plot shows $\frac{d\sigma}{dt'}$ along with a fit to equation 8.1 over the full range of the data.

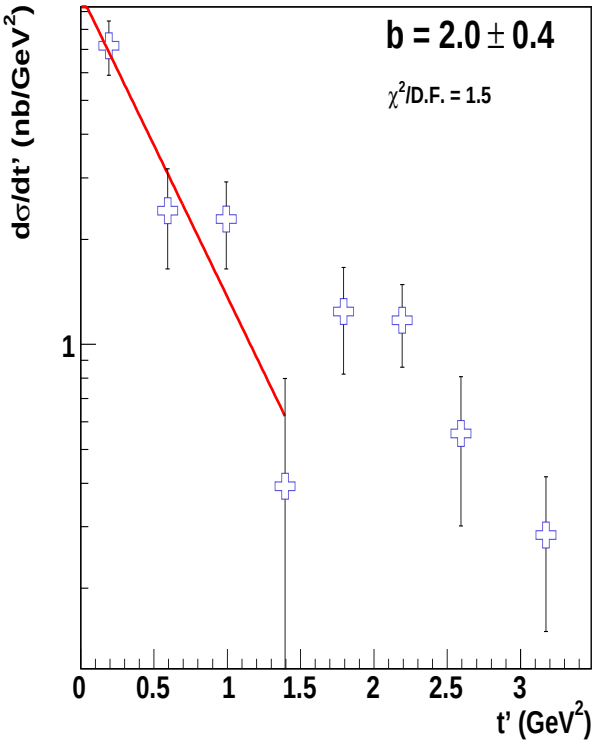

Figure 8.3: Plot shows $\frac{d\sigma}{dt'}$ along with a fit to equation 8.1 from 0.0 to 1.4 GeV^2 which corresponds to the range of the first diffractive minima.

in t' between 0.0 and 1.4, corresponding to the first "diffractive fringe", yielding $b_\phi = 2.00$ GeV^{-2}. The variable $c\Delta\tau$ characterizes the spatial or temporal extent of the fluctuation of the virtual meson. It is obtained through uncertainty principle arguments to be

$$\Delta\tau = \frac{2\nu}{(Q^2 + M_\phi^2)} \tag{8.3}$$

The nature of the interaction becomes more point-like as Q^2 increases and the fluctuation time and the spatial extent of the fluctuation decreases. This transition should be observed as a decrease in the measured b parameter. This is illustrated in Figure 8.4. Since the differential cross section in t' was extracted for all Q^2, the value for b will be quoted at an average $c\Delta\tau$ calculated at an average $Q^2 = 2.21$ GeV^2 and the average value of $\nu = 4.23$ GeV for the data. These values along with those of the

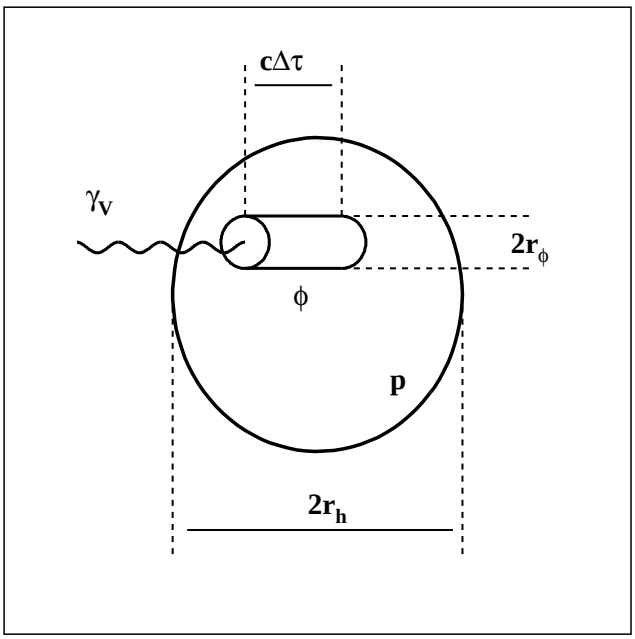

Figure 8.4: Spacetime picture of the interaction between the virtual ϕ meson (radius r_ϕ) and the proton (radius r_h). The diagram shows the characteristic fluctuation distance $c\Delta\tau$ compared to the overall size of the proton. This is not drawn to scale.

previous CLAS analysis are quoted in table 8.1. The results are consistent with the expected decrease in b.

Data	b	$c\Delta\tau$ (fm)	Q^2 (GeV^2)
CLAS/Santoro	0.99 ± 0.17	0.46	2.21
CLAS/Lukashin	1.61 ± 0.31	0.60	1.02

Table 8.1: The value of the impact parameter b for a fit to the full t' range for this analysis and the previous CLAS analysis.

8.3 Comparison to JML Predictions

The differential cross section in t was extracted for comparison to the JML model. The data for $1.6 \leq Q^2 \leq 4.0$ GeV^2 plus the JML model prediction [44] is shown in

6.6. The hybrid model, assuming a Pomeron plus 2 gluon exchange [45], represented the data in this bin quite well. Deviations at high -t suggest that we have not yet reached the region where 2 gluon exchange is completely dominant. The data for all Q^2 plus the JML prediction is shown in 6.6.

8.3.1 Q^2 dependence of the total cross section

The total cross sections as a function of Q^2 and the JLM predictions for the total cross section at three different center of mass energies is shown in figure 8.5. The

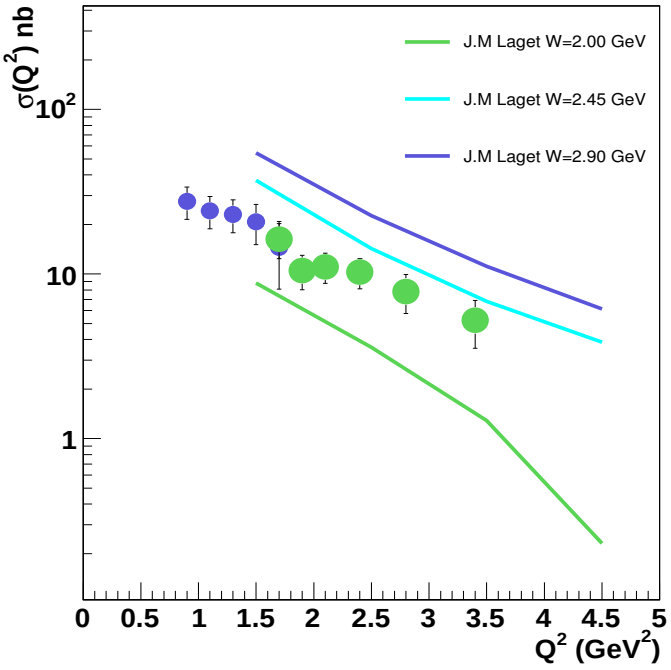

Figure 8.5: Figure shows our data (green points) well as the previous CLAS analysis (blue points) plotted with the JML prediction for the total cross section at three different W values: W=2.0,2.45, and 2.90 GeV.

JML cross section predictions were calculated at the average $\epsilon = 0.44$ of our data. The model brackets the data at the W values used for calculation and also shows the same common trend as the data.

8.4 SCHC and the Extraction of σ_L

There are multiple handles on testing the validity of SCHC. The method employed in this analysis is to fit the $\frac{d\sigma}{d\Phi}$ distribution to equation 7.5. If SCHC holds, both σ_{TT} and σ_{LT} should vanish. In Figure 7.4, the fit parameters σ_{TT} and σ_{LT} are shown to be compatible with 0. For this analysis, we can conclude that SCHC is valid. This allows a simple expression for the ratio $R = \frac{\sigma_L}{\sigma_T}$

$$R = \frac{1}{\epsilon}\frac{r_{00}^{04}}{1 - r_{00}^{04}} \tag{8.4}$$

The value of $r_{00}^{04} = 0.37$ was obtained through a fit to the polar angle decay distribution $W(\cos\theta_H)$ for the entire Q^2 range. The ratio R can now be computed for an average Q^2 utilizing equation 8.4. The values are tabulated in 8.2. Ideally, one would like

r_{00}^{04}	0.37 ± 0.05
$< \epsilon >$	0.44
R	1.33 ± 0.18

Table 8.2: Summary of parameters extracted as a consequence of SCHC

to extract a value of r_{00}^{04} and R for each Q^2 bin and a corresponding σ_L. As was previously mentioned, the statistics of this channel are limited, so instead an r_{00}^{04} for a weighted-average Q^2 was extracted and a corresponding R. The value of the longitudinal cross section for the weighted-averaged Q^2 and average $< \epsilon >$ can be computed as:

$$\sigma_L = \frac{\sigma_{avg}}{R(1+ < \epsilon >)} \tag{8.5}$$

For this data, the value used and the results are in Table 8.3. The measurement from

σ_{avg}	σ_L
10.2 ± 2.4	5.3 ± 1.3

Table 8.3: Extraction of σ_L

this analysis is plotted along with the previous CLAS result, HERMES measurements

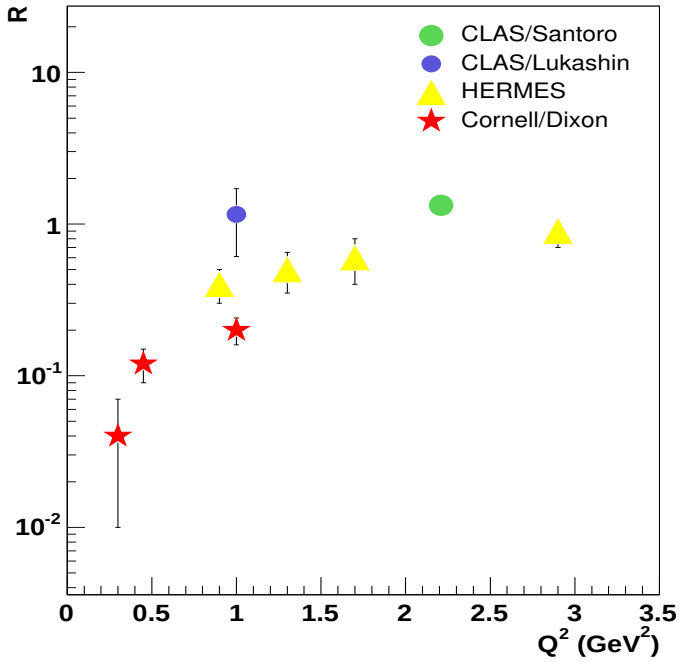

Figure 8.6: Plot shows $R = \sigma_L/\sigma_T$ vs. Q^2 for our data (green dot), previous CLAS results (blue dot), HERMES results (yellow triangles) and Cornell data (red stars).

and electroproduction from Cornell in Figure 8.6. The data shows a slow rise in R as expected relative to the Cornell and HERMES data. Our data point is consistent with the previous CLAS data point at $Q^2 = 1.0$ GeV^2.

8.5 Discussion and Conclusions

ϕ meson electroproduction was examined in the kinematical regime: $1.6 \leq Q^2 \leq 3.8$, $0.0 \leq t' \leq 3.6$, and $2.0 \leq W \leq 3.0$. This analysis accrued approximately four times the statistics as the previous ϕ electroproduction analysis [2]. From the measurement of the impact parameter $b_\phi = 0.99$ GeV^{-2} ($R_{int} = 0.39$ fm compared to the proton radius of 1.0 fm), it can be concluded that we have entered a regime where the partonic structure of the proton is being probed (See Figure 8.4). The behavior of the impact parameter is consistent with the predictions of VMD as well as withprevious measurements. Comparisons of the differential cross section $d\sigma/dt$

to the JML model predictions show very good agreement with the data up to high values of $-t \sim 3.0$ GeV^2. The JML model predictions at various values of W bracket the total cross section $\sigma(Q^2)$ measurements but are systematically high. The scaling behavior of the total cross section $1/Q^{4.6\pm1.7}$ is compatable within errors to the $1/Q^4$ VMD prediction as well as the $1/Q^6$ GPD scaling prediction. The data suggest that we are straddling an intermediate region between the applicability of the two models. It was shown from the differential cross section $d\sigma/d\Phi$ that SCHC is valid at the 13% level. The decay distribution parameter r_{00}^{04} was then measured from a fit of the 1-dimensional projection $W(\cos\theta_H)$ to the $dN/d\cos\theta_H$ distribution.

In their range of validity, GPDs make certain predictions about the cross section, namely that the longitudinal part of the cross section σ_L becomes dominant as Q^2 increases. In other words, we expect R to increase as a function of Q^2. SCHC permitted us to determine an average value of R from the determination of r_{00}^{04} and subsequently an average value of σ_L. The R value measured for this analysis was larger compared to previous measurements at lower Q^2 and is consistent with the prediction that σ_L increases with Q^2. However, it does not yet dominate the cross sections, suggesting that we have not yet reached a kinematic domain where reliable calculations can be made within the framework of GPDs.

Bibliography

[1] K. Schilling and G. Wolfe. *Nucl. Phys.*, B61:381, 1973.

[2] K. Lukashin *et al.* Exlcusive electroproduction of $\phi(1020)$ mesons at 4.2 GeV. *Phys. Rev. C*, 64:059901(E), 2001.

[3] D.G. Cassel *et al.* Exclusive ρ^0, ω and ϕ electroproduction. *Phys. Rev. D*, 24(11):2787, 1981.

[4] E.S. Smith, H. Funsten, and P. Rubin. Measurement of the polarization of the $\phi(1020)$ in electroproduction. Proposal to PAC6, Jefferson Lab Hall B, 5 April 1993.

[5] E. Leader and E. Predazzi. *An Introduction to Gauge Theories and the New Physics*. Cambridge University Press, 1982.

[6] J. Bartels, D. Haidt, and A. Zichichi. Review of particle physics. *Eur. Phys. J. C*, 15(1-4), 2000.

[7] L.N. Hand. Experimental investigation of pion electroproduction. *Phys. Rev.*, 129(4):1834, 1962.

[8] T.H. Bauer and R.D. Spital. The hadronic properties of the photon in high-energy interactions. *Rev. of Modern Physics*, 50(2):261, 1978.

[9] T.D. Lee. *Particle Physics and Introduction to Field Theory*. Harwood Academic Publishers, 1981.

[10] L. Morand. *Deeply Virtual Production of the Omega Meson*. PhD thesis, CEA-Saclay, 2004.

[11] T. Regge. Introduction to complex orbital momenta. *Nuovo Cimento*, XIV(5), 1959.

[12] S. Donnachie, Guenter Dosch, Peter Landshoff, and Otto Nachtman. *Pomeron Physics and QCD*. Cambridge University Press, 2002.

[13] T. Regge. Bound state, shadow states and mandelstam representation. *Nuovo Cimento*, XVIII(5), 1960.

[14] J.-M. Laget and R. Mendez-Galain. Exclusive photo- and electroproduction of vector mesons at large momentum transfer. *Nuclear Physics*, A581:397–428, 1995.

[15] F. Cano and J.-M. Laget. Real and virtual compton scattering in a regge approach. *Phys. Letters B.*, 551:317–323, 2003.

[16] C. Hadjidakis *et al.* Deeply virtual production of ρ^0 mesons. CLAS-ANALYSIS 2004-108, Jefferson Lab Hall B, IPN Orsay, DAPNIA/SPhN, CEA-Saclay, 2004.

[17] A. Airapetian. Exclusive leptoproduction of ρ^0 mesons from hydrogen at intermediate virtual photon energies. *Eur. Phys. Journal C.*, 17:389–398.

[18] M. Guidal *et al.* Deeply virtual electroproduction of vector mesons. JLab proposal e-99-105, Hall B, 1999.

[19] M. Diehl. Generalized parton distributions. *Physics Reports*, 388:41–277, 2003.

[20] K. Lukashin. *Electroproduction of the* $\phi(1020)$ *Vector Meson at 4.2 GeV*. PhD thesis, Virginia Polytechnic Institute and State University, 2000.

[21] J. Collins *et al.* Factorization for hard exclusive electroproduction of meson in QCD. *Phys. Rev. D.*, 56(5), 1997.

[22] M. Vanderhaeghen, P.A.M. Guichon, and M. Guidal. Deeply virtual electroproduction of photons and mesons on the nucleon: Leading order amplitudes and power corrections. *Phys. Rev. D*, 60:094017, 1999.

[23] M. Vanderhaeghen, P.A.M. Guichon, and M. Guidal. Hard electroproduction of photons and mesons on the nucleon. *Phys. Rev. Letters*, 80(23):5064, 1998.

[24] X. Ji. Gauge-invariant decomposition of nucleon spin. *Phys. Rev. Letters*, 78(4):610, 1997.

[25] R. Dixon *et al.* Electroproduction of ϕ mesons. *Phys. Rev. Letters*, 39(9):516, 1977.

[26] B.A. Mecking *et al.* The CEBAF large acceptance spectrometer. *Nuclear Instruments and Methods in Physics Research A*, 503:513–553, 2003.

[27] S. Morrow *et al.* Target cell and vacuum chamber in GSIM for e1-6a. Technical report, SPhN-Saclay, 19 Dec. 2002.

[28] G. Adams *et al.* The CLAS cherenkov detector. *Nuclear Instruments and Methods in Physics Research A*, 465:414–427, 2001.

[29] E.S. Smith *et al.* Calibration of the CLAS TOF system. CLAS-NOTE 2001-011, Jefferson Lab Hall B, 2001.

[30] E.S. Smith and R. Nasseripour. Systematic study of time-walk corrections for the tof counters. CLAS-NOTE 2002-007, Jefferson Lab Hall B, 2002.

[31] M.D. Mestayer *et al.* The CLAS drift chamber system. *Nuclear Instruments and Methods in Physics Research A*, 449:81–111, 2000.

[32] M. Amarian *et al.* The CLAS forward electromagnetic calorimeter. *Nuclear Instruments and Methods in Physics Research A*, 460:239, 2001.

[33] L.C. Smith. Private Communications.

[34] L. Elouadrhiri *et al.* Charged particle identification in CLAS. CLAS-NOTE 1998-004, Jefferson Lab Hall B, 1998.

[35] Kijun Park. Electron fiducial cuts. webpage: http://www.jlab.org/Hall-B/secure/e1-6/parkkj/public_html/e1-6/e1-6-meeting/first_talk.html.

[36] Kijun Park *et al.* Kinematical corrections for CLAS. CLAS-NOTE 2003-012, Jefferson Lab Hall B, 2003.

[37] K.S. Egyian. Determination of electron energy cut due to the CLAS EC threshold. CLAS-NOTE 1999-007, Jefferson Lab Hall B, 1999.

[38] S. Morrow *et al.* Proton energy loss correction for e1-6a. Technical report, SPhN-Saclay, 20 Nov. 2003.

[39] F. Sabatié *et al.* Momentum corrections for e1-6 using kinematical fits. CLAS-NOTE 2003-010, Jefferon Lab Hall B, 2003.

[40] M. Ungaro and J. Li. Procedure for drift chamber inefficiencies. CLAS-NOTE 2003-006, Jefferson Lab Hall B, 2003.

[41] A. Afanasev and I. Akushevich. QED radiative corrections in processes of exclusive pion production. *Phys. Rev. D*, 66:074004, 2002.

[42] K. Schilling, P. Seyboth, and G. Wolf. On the analysis of vector-meson production by polarized photons. *Nucl. Phys.*, B15:397–412, 1970.

[43] A. Borissov. Meson 2000 workshop. In *Cross Sections of Vector Meson Production at intermediate virtual photon energies*, Cracow, Poland, 2000.

[44] J.-M. Laget. Private Communications.

[45] J.-M. Laget. Photoproduction of vector mesons at large momentum transfer. *Phys. Letters B.*, 489:313–318, 2000.

Appendix A

Acceptance and Efficiency Tables

$< Q^2 >$ (GeV^2)		1.7	1.9	2.1	2.3	2.5	2.7	2.9	3.1	3.3	3.5	3.7
$< -t >$ (GeV^2)	0.1	0.2	-	-	-	-	-	-	-	-	-	-
	0.3	0.5	0.9	1.0	0.9	1.1	0.9	0.7	0.5	0.2	-	-
	0.5	0.6	1.1	1.6	1.8	1.8	1.8	1.5	1.6	0.8	0.4	0.2
	0.7	0.6	1.1	1.6	1.8	1.9	2.0	2.1	1.9	1.8	1.7	1.0
	0.9	0.6	1.2	1.6	1.9	2.2	2.2	2.4	2.2	2.2	2.2	1.7
	1.1	0.6	1.2	1.6	1.9	2.2	2.2	2.2	2.3	2.4	2.1	2.1
	1.3	0.6	1.2	1.7	2.2	2.1	2.4	2.3	2.5	2.4	2.2	2.0
	1.5	0.7	1.1	1.7	2.1	2.3	2.5	2.3	2.4	2.5	2.2	2.0
	1.7	0.6	1.4	1.5	2.0	2.4	2.5	2.7	2.5	2.5	2.5	2.2
	1.9	0.7	1.2	1.8	1.9	2.4	2.5	2.6	2.6	2.3	2.6	1.9
	2.1	0.6	1.1	1.7	1.7	2.3	2.6	2.3	2.1	2.4	2.3	2.2
	2.3	0.7	1.4	1.7	2.0	2.3	2.3	2.2	2.3	2.5	2.7	2.1
	2.5	0.7	1.1	1.5	1.6	1.9	2.0	2.3	2.6	2.5	2.6	2.2
	2.7	0.8	1.3	1.7	1.9	2.0	2.5	2.5	2.5	2.6	2.0	1.7
	2.9	0.6	1.0	1.6	1.8	1.9	2.0	2.3	2.2	2.2	2.5	2.2
	3.1	0.8	1.1	1.3	1.6	1.8	1.8	2.2	2.4	1.5	2.4	2.3
	3.3	0.8	1.1	1.2	1.6	2.1	2.3	2.2	2.3	1.6	2.0	1.9
	3.5	0.6	1.1	1.1	0.9	1.5	1.6	1.9	2.3	2.6	2.2	2.0
	3.7	0.5	0.9	1.0	1.5	1.6	1.9	2.4	1.2	1.9	2.4	1.6

Table A.1: Acceptance table for all Q^2 and t bins. The values are quoted in percent. Bins with a value "-" are those with an acceptance value below 0.2%.

Q^2 (GeV^2)		1.7	1.9	2.1	2.3	2.5	2.7	2.9	3.1	3.3	3.5	3.7
x_B	0.05	90.5	96.4	96.4	96.4	96.4	96.4	96.4	96.4	96.4	96.4	96.4
	0.15	91.7	93.6	95.1	96.1	96.3	96.4	96.4	96.4	96.4	96.4	96.4
	0.25	91.9	93.3	94.5	95.3	96.3	97.2	97.0	96.2	96.0	96.0	96.0
	0.35	96.0	88.9	93.1	94.2	96.0	97.0	97.2	97.0	96.8	96.7	96.5
	0.45	96.8	91.3	92.3	93.1	94.3	96.2	97.7	97.7	97.3	97.1	97.0
	0.55	96.8	96.8	96.8	96.8	96.8	96.8	97.5	97.5	98.0	98.5	97.2
	0.65	97.6	97.6	97.6	97.6	97.6	97.6	97.6	97.6	97.6	97.6	97.6

Table A.2: Cherenkov Efficiency table.

	Φ									
W	18	54	90	126	162	198	244	280	316	352
2.0	0.750	0.746	0.740	0.735	0.733	0.733	0.735	0.740	0.746	0.750
2.1	0.767	0.760	0.749	0.741	0.736	0.736	0.741	0.749	0.760	0.767
2.2	0.776	0.767	0.753	0.742	0.737	0.737	0.742	0.753	0.767	0.776
2.3	0.783	0.772	0.756	0.744	0.739	0.739	0.744	0.756	0.772	0.783
2.4	0.789	0.776	0.759	0.746	0.741	0.741	0.746	0.759	0.776	0.789
2.5	0.793	0.780	0.762	0.749	0.743	0.743	0.749	0.762	0.780	0.793
2.6	0.796	0.783	0.765	0.752	0.746	0.746	0.752	0.752	0.752	0.752
2.7	0.797	0.785	0.768	0.756	0.750	0.750	0.756	0.768	0.785	0.797
2.8	0.797	0.787	0.772	0.760	0.755	0.755	0.760	0.772	0.787	0.797
2.9	0.794	0.787	0.775	0.766	0.762	0.762	0.766	0.775	0.787	0.794

Table A.3: Radiative corrections table. Φ is in degrees and W is in GeV.